7

Vibrational dynamics of hydrogen bonds

Erik T. J. Nibbering[1], Jens Dreyer[1], Oliver Kühn[2], Jens Bredenbeck[3], Peter Hamm[3], Thomas Elsaesser[1]

[1] Max-Born-Institut für Nichtlineare Optik und Kurzzeitspektroskopie, Berlin, Germany
[2] Institut für Chemie und Biochemie, Freie Universität Berlin, Germany
[3] Physikalisch Chemisches Institut, Universität Zürich, Switzerland

Coordinated by: Erik T. J. Nibbering

7.1 Significance of hydrogen bonding

Hydrogen bonds are ubiquitous and of fundamental relevance in nature. Representing a local attractive interaction between a hydrogen donor and an adjacent acceptor group, they result in the formation of single or multiple local bonds with binding energies in the range from 4 to 50 $\mathrm{kJ\,mol^{-1}}$, much weaker than a covalent bond, but stronger than most other intermolecular forces and thus decisive for structural and dynamical properties of a variety of molecular systems [1–4]. Disordered extended networks of intermolecular hydrogen bonds exist in liquids such as water and alcohols, determining to a large extent their unique physical and chemical properties. At elevated temperatures, such liquids undergo pronounced structural fluctuations on a multitude of time scales, due to the limited interaction strength. In contrast, well-defined molecular structures based on both intra- and intermolecular hydrogen bonds exist in polyatomic molecules, molecular dimers and pairs and – in particular – in macromolecules such as DNA and other biomolecular systems.

Vibrational spectra of hydrogen-bonded systems reflect the local interaction strength and geometries as well as the dynamics and couplings of nuclear motions. Steady-state infrared and Raman spectra have been measured and modeled theoretically for numerous systems, making vibrational spectroscopy one of the major tools of hydrogen bond research [5]. In many cases, however, conclusive information on structure and – in particular – dynamics is difficult to derive from stationary spectra which average over a multitude of molecular geometries and time scales. In recent years, vibrational spectroscopy in the ultrafast time domain [6] is playing an increasingly important role for observing hydrogen bond dynamics in real-time, for separating different types of molecular couplings, and for determining them in a quantitative way [7]. Using such sophisticated probes, it has been established that the basic dynamic properties of hydrogen bonds are determined by processes in the femto- to picosecond time domain. The acquired knowledge about both potential energy surfaces of hydrogen-bonded systems and their dynamical properties may prove to be useful to design optical control schemes to steer reactive processes – that is hydrogen or proton transfer – by interaction with tailored coherent infrared pulses or pulse sequences.

In this Chapter, an overview of this exciting new field is presented with emphasis on both experimental and theoretical studies of the coherent response and of incoherent relaxation dynamics of hydrogen bonds in the electronic ground state [8–32]. In Sect. 7.2, the characteristic features of the vibrational spectra of hydrogen-bonded systems, the underlying coupling mechanisms, and the resulting molecular processes are introduced. Section 7.3 describes the experimental and theoretical methods applied in ultrafast vibrational spectroscopy of hydrogen bonds. Vibrational dephasing and incoherent processes of population relaxation and energy dissipation in disordered hydrogen-bonded systems such as water are discussed in Sect. 7.4. Section 7.5 is devoted to coherent nuclear motions and relaxation processes in intra- as well as intermolecular hydrogen-bonded structures with well-defined geometries in a liquid environment. An outlook is presented in Sect. 7.6.

7.2 Molecular vibrations as probe of structure and dynamics of hydrogen bonds

Vibrational spectroscopy provides direct insight into the couplings between normal modes as governed by the potential energy surfaces of hydrogen bonds. Here the characteristics of vibrational motions in hydrogen-bonded molecular systems are introduced and aspects of the theoretical modeling are discussed.

7.2.1 Vibrational modes of hydrogen-bonded systems

The formation of hydrogen bonds results in pronounced changes of the vibrational spectra of the molecules involved [5]. In a $X{-}H\cdots Y$ hydrogen bond, with X and Y usually being electronegative atoms such as O or N, the absorption band of the stretching mode of the X−H donor group (ν_{XH}) displays the most prominent modifications, a red-shift and – in most cases – a substantial spectral broadening and reshaping as well as a considerable increase in intensity (Fig. 7.1).

The red-shift reflects the reduced force constant of the oscillator and/or the enhanced anharmonicity of the vibrational potential along the X−H stretching coordinate, i.e. an enhanced diagonal anharmonicity. The red-shift has been used to characterize the strength of hydrogen bonds [33–35]. Spectral broadening can originate from different types of interactions, among them anharmonic coupling of the high-frequency X−H stretching mode to low-frequency

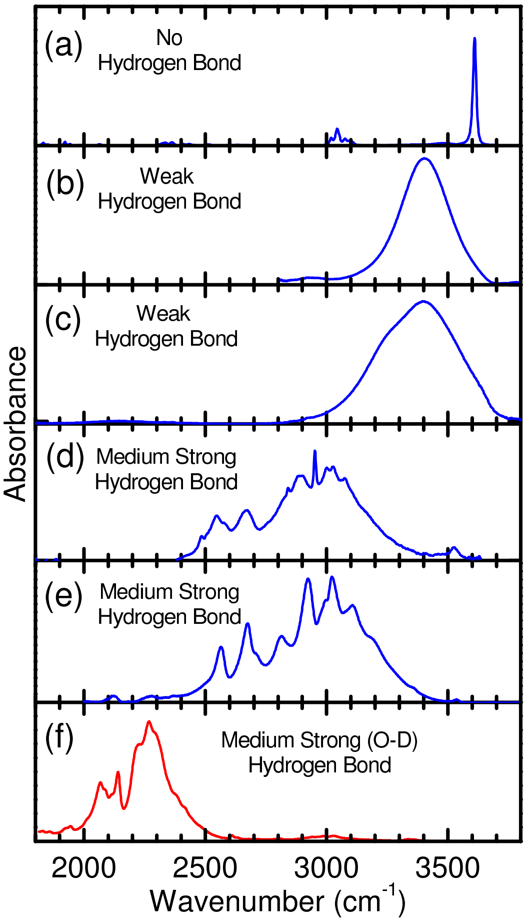

Fig. 7.1. Infrared absorption spectra showing O−H stretching absorption bands of (a) uncomplexed phenol in C_2Cl_4, (b) the weak hydrogen bond of HOD in D_2O, (c) neat H_2O, (d) the medium strong hydrogen bond of PMME-H, (e) acetic acid dimer $(CD_3{-}COOH)_2$, and (f) the O−D stretching band of acetic acid dimer $(CD_3{-}COOD)_2$.

modes, Fermi resonances with overtone and combination tone levels of fingerprint modes, vibrational dephasing, and inhomogeneous broadening due to different hydrogen bonding geometries in the molecular ensemble [36–39]. The substantial enhancement of the spectrally integrated absorption intensity accompanying spectral broadening is related to changes of the electronic structure. In contrast to the stretching mode, X−H in-plane bending modes (δ_{XH}), with transitions located in the fingerprint region of the vibrational spectrum, undergo small blue-shifts upon hydrogen bonding, but usually without appreciable effects on the line shape [5].

In the weak attractive potential between hydrogen donor and acceptor groups, modes which are connected with motions of the heavy atoms thereby affecting the hydrogen bond distance, can be identified. Formation of intermolecular hydrogen-bonded dimers gives rise to six new vibrational low-frequency modes out of translational and rotational degrees of freedom, among them the dimer hydrogen bond stretching (ν_{dimer}) and bending (δ_{dimer}) modes. In hydrogen bond networks, e.g., in water, intermolecular modes often extend over several molecules and dominate the low-frequency vibrational spectrum. The small force constants and the large reduced mass of such hydrogen bond modes result in low-frequency modes typically located below $200\,\mathrm{cm}^{-1}$. Corresponding intramolecular hydrogen bond modes, on the other hand, are often found up to $400\,\mathrm{cm}^{-1}$. Thus, these hydrogen bond motions with vibrational periods of about 660 to 80 fs are clearly separated in time from high-frequency X$-$H stretching motions with vibrational periods on the order of 10 to 15 fs.

7.2.2 Vibrational coupling mechanisms

Hydrogen bonding enhances the anharmonicity of the potential energy surface resulting in strengthened mechanical coupling of different vibrational modes. Anharmonic mode coupling is crucial for the line shape of vibrational absorption bands, hydrogen bond dynamics, and for vibrational energy transfer. In the vibrational spectra, anharmonic mode couplings are manifested by the appearance of over- and combination tones, band splittings and/or frequency shifts of harmonic transitions. In the following different mechanisms of anharmonic coupling are discussed.

7.2.2.1 Anharmonic coupling with low-frequency hydrogen bond modes

Anharmonic coupling between the high-frequency X$-$H stretching mode and low-frequency hydrogen bond modes has been considered a potential broadening mechanism of the X$-$H stretching band [36, 37, 39]. The separation of time scales between low- and high-frequency modes allows for a theoretical description in which the different states of the X$-$H stretching oscillator define adiabatic potential energy surfaces for the low-frequency modes (Fig. 7.2a), similar to the separation of electronic and nuclear degrees of freedom in the Born-Oppenheimer picture of vibronic transitions. Vibrational transitions from different levels of the low-frequency oscillator in the $v(\nu_{XH}) = 0$ state to different low-frequency levels in the $v(\nu_{XH}) = 1$ state with a shifted origin of the potential result in a progression of lines which, for moderate displacements, is centered at the pure X$-$H stretching transition and displays a mutual line separation by one quantum of the low-frequency mode (as depicted in Fig. 7.2b). The absorption strength is determined by the dipole moment of the $v(\nu_{XH}) = 0 \rightarrow 1$ transition of the X$-$H stretching mode and

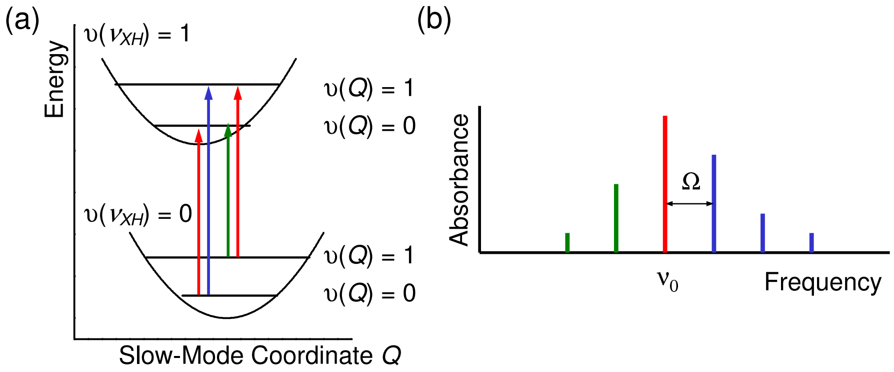

Fig. 7.2. (a) Potential energy surfaces for the hydrogen bond low-frequency mode in a single hydrogen bond, showing a displacement along the low-frequency (slow-mode) coordinate Q as function of the quantum state of the X−H/X−D high-frequency (fast-mode) stretching coordinate q (ν_{HX}). The X−H/X−D stretching transition is accompanied by changes in the low-frequency mode quantum state governed by Franck-Condon factors; (b) The corresponding stick spectrum of the X−H/X−D stretching transition shows the Franck-Condon progression centered at ν_0 ($v(\nu_{XH}) = 0 \rightarrow 1$) with frequency separations Ω of the low-frequency mode.

the Franck-Condon factors between the optically coupled levels of the low-frequency mode. With increasing difference in quantum number of the low-frequency mode in the $v(\nu_{XH}) = 0$ and 1 states, the Franck-Condon factors decrease and the progression lines become weaker for larger frequency separation from the progression center. For each low-frequency mode coupling to an X−H stretching oscillator, an independent progression of lines occurs.

Excitation of anharmonically coupled oscillators with a broadband ultrashort laser pulse resonant to the X−H stretching band can create a phase-coherent superposition of several levels of the low-frequency mode making up a vibrational wave packet. The wave packet can be generated in the $v(\nu_{XH}) = 1$ excited state by direct excitation, in the $v(\nu_{XH}) = 0$ ground state through a Raman-like process, or by coherence transfer from the $v(\nu_{XH}) = 1$ to the $v(\nu_{XH}) = 0$ state. These vibrational wave packets can be observed by ultrafast nonlinear vibrational spectroscopy as coherent dynamics [8, 9].

7.2.2.2 Fermi resonances of the X−H stretching $v(\nu_{XH}) = 1$ state with overtone or combination levels of fingerprint vibrations

Coupling of the $v(\nu_{XH}) = 1$ state with higher lying states of fingerprint vibrations, such as the X−H bending mode, through Fermi resonances can lead to level splittings [38]. In this way the over- and combination tones, which are harmonically forbidden, gain in cross section. For Fermi resonances in the weak coupling regime, a vibrational energy redistribution channel is facilitated (Fig. 7.3a). For the strong coupling limit a level splitting is observed

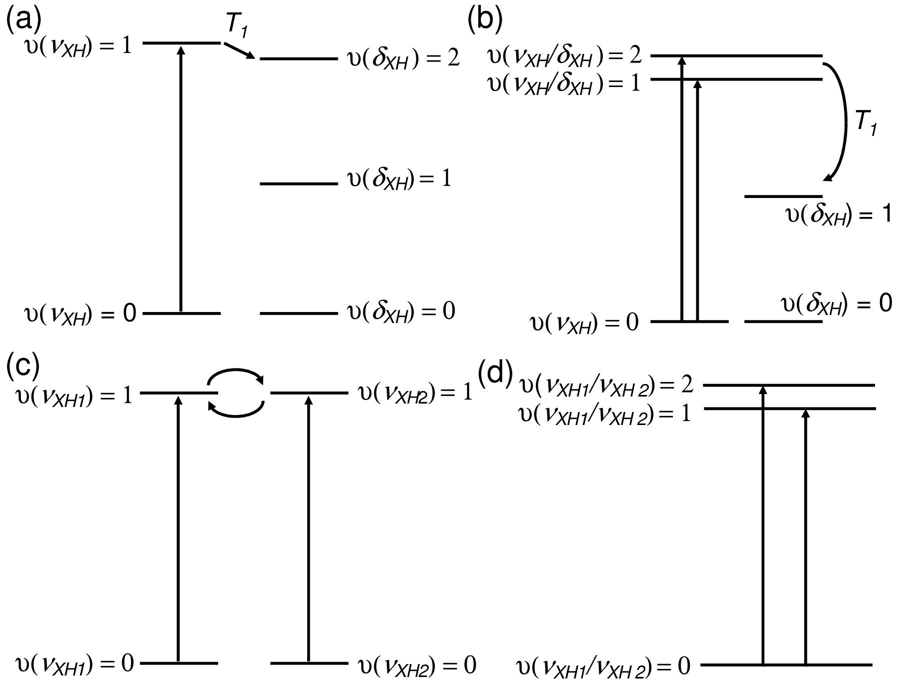

Fig. 7.3. Fermi resonance scheme in the weak (a) and strong (b) coupling limits between the X–H/X–D stretching $v(\nu_{XH}) = 1$ and the $v(\delta_{XH}) = 2$ bending levels. In (a) the weak Fermi resonance facilitates an efficient relaxation channel for energy redistribution, whereas case (b) explains the observation of additional transitions within the X–H/X–D stretching bands. The Davydov coupling scheme in the weak (c) and strong (d) limits between $v(\nu_{XH}) = 1$ levels of different X–H/X–D oscillators explain the phenomenon of vibrational excitation energy transfer (c) and excitation delocalization (d).

in the X–H stretching spectral region, indicative of states with mixed quantum character and concomitant similar absorption cross sections (Fig. 7.3b). In Sect. 7.5 experimental and numerical evidence of this mechanism will be provided for a few selected cases.

7.2.2.3 Davydov coupling between local X–H stretching oscillators

If several local oscillators can be found in one molecular assembly, for instance X–H stretching modes in acetic acid dimers or nucleic acid base pairs, or amide I vibrations in peptides, an excitonic type of interaction denoted as Davydov coupling may occur between the respective $v(\nu_{XH}) = 1$ states of the local oscillators. Small couplings enable vibrational excitation energy transfer between nearby X-H oscillators (Fig. 7.3c), whereas strong coupling leads to new combinations of quantum states (Fig. 7.3d), in a similar fashion as for amide I vibrations in proteins [40]. Line splittings with altered absorption cross sections of the individual transitions are dictated by the relative orientations of the transition dipole moments of the single X−H oscillators. In the case of the cyclic acetic acid dimer (see Sect. 7.5), selection rules based on the C_{2h} symmetry govern the IR- or Raman-activity of the transitions [37].

7.2.2.4 Coupling with fluctuating solvent modes

In the condensed phase the hydrogen bond is subject to fluctuating forces exerted by the solvent bath. These solvent bath modes, typically being overdamped, lead to spectral diffusion and broadening of the vibrational transition lines. Depending on the modulation strength and the fluctuation time scales, the spectra may vary between a distribution of transition frequencies corresponding to different hydrogen bond configurations (inhomogeneous broadening) or an averaged motionally narrowed transition (homogeneous broadening). Different theoretical approaches to describe the frequency modulation have been used: either the dipole moment of the X−H stretching oscillator is directly coupled to the local electric field induced by the solvent [41,42], or the low-frequency modes coupled to the X−H oscillator are stochastically modulated [43–45]. For an extensive discussion on the different underlying line broadening mechanisms, both using classical and quantum approaches, the reader is referred to a review by Henri-Rousseau, Blaise, and Chamma [39].

Using the density operator approach, the vibrational absorption line shape $\alpha(\omega)$ for a $v = 0 \rightarrow 1$ transition is given by:

$$\alpha(\omega) \propto \int_{-\infty}^{\infty} dt\, e^{-i(\omega-\omega_0)t} \langle \boldsymbol{\mu}_{10}(t)\boldsymbol{\mu}_{10}(0)\rangle \ , \tag{7.1}$$

with the transition dipole moment correlation function:

$$\begin{aligned} \langle \boldsymbol{\mu}_{10}(t)\boldsymbol{\mu}_{10}(0)\rangle &= |\mu_{10}|^2 \left\langle \exp\left[-i\int_0^t d\tau\, \delta\omega_{XH}(\tau)\right]\right\rangle \\ &\cong |\mu_{10}|^2 \exp\left[-i\int_0^t d\tau_2 \int_0^t d\tau_1\ \langle \delta\omega_{XH}(\tau_1)\delta\omega_{XH}(\tau_2)\rangle\right] \ , \end{aligned} \tag{7.2}$$

where $\boldsymbol{\mu}_{10}$ is the transition dipole moment of the vibrational transition centered at ω_0. In the interpretation of linear spectra, but even more so for results obtained with nonlinear experiments, the quantity governing the line broadening is the X−H transition frequency fluctuation correlation function $C(t)$:

$$C(t) = \langle \delta\omega_{XH}(t)\delta\omega_{XH}(0)\rangle \ , \tag{7.3}$$

where $\omega_{XH}(t)$ is the time-dependent X−H transition frequency. Solvent-induced line broadening for hydrogen-bonded systems has been modeled using

$C(t)$ subject to the assumption of Gauss-Markov modulation of the transition frequency:

$$C(t) = \varDelta^2 \exp\left(-\frac{t}{t_c}\right) , \tag{7.4}$$

with $\varDelta$ being the modulation strength (a measure for the distribution of possible transition frequencies for hydrogen-bonded systems) and t_c the frequency fluctuation correlation time (indicating the average time a particular hydrogen-bonded system resides at a particular frequency), with which one can interpolate between the inhomogeneous static and homogeneous fast modulation limits [46]. In the case of an infinitely short correlation time t_c, $C(t)$ can be approximated as a δ-function, i.e. $C(t) = \varDelta^2 t_c \delta(t) = \delta(t)/T_2$, and a Lorentzian line shape dictated by the transverse dephasing time T_2 results. A homogeneous broadening described by a single T_2 time has been used for hydrogen-bonded systems with well-defined geometries in weakly interacting nonpolar solvents (see Sect. 7.5). However, for disordered highly fluctuating hydrogen-bonded systems often a sum of exponentially decaying functions is being used to mimic the more complex temporal behavior suggesting a multitude of characteristic fluctuation time scales underlying the microscopic dynamics (see the discussion in Sects. 7.4.1 and 7.4.2). More extensive expressions for $C(t)$ using Brownian oscillators have also been used [47]. A special case is the stochastic exchange between a limited number of hydrogen bond configurations, a case that has also been treated in the review by Kubo [46]. Here, the frequency separation between vibrational transitions indicative of the different hydrogen bond configurations and the exchange rate between these configurations dictates the absorption line shapes. In Sect. 7.4.4 an example will be provided of how chemical exchange influences the outcome of nonlinear infrared experiments.

Summarizing, the discussed mechanisms result in spectral substructures and/or a strong broadening of the overall O−H stretching band, even for a small number of absorption lines with large Franck-Condon factors. The different anharmonic couplings transform the hydrogen stretching oscillator into a vibrational multilevel system with a manifold of transition lines, each broadened by the solvent modulations.

7.2.3 Calculation of vibrational couplings in hydrogen bonds

Hydrogen bond potential energy surfaces are often dominated by electrostatic interactions and exchange repulsions, but depending on the type of hydrogen bond, polarization, charge-transfer, covalent or van der Waals forces contribute as well [48]. Thus, only a well-balanced theoretical description accurately accounts for the subtle interplay between these physical interactions. Numerical treatments to account for the anharmonicity of potential energy surfaces are introduced next, followed by a discussion of the suitability of different quantum chemical methods to describe hydrogen bonding.

7.2.3.1 Anharmonic coupling of vibrational modes

Most commonly anharmonically coupled vibrational force fields are calculated perturbatively by expanding the potential energy surface in a Taylor series with respect to a suitable set of coordinates $\{q_i\}$ around a reference geometry usually taken as the equilibrium geometry [49]:

$$\begin{aligned} V = V_0 &+ \sum_{i}^{3N-6} \Phi_i \, q_i + \sum_{i,j}^{3N-6} \Phi_{ij} \, q_i q_j \\ &+ \sum_{i,j,k}^{3N-6} \Phi_{ijk} \, q_i q_j q_k + \sum_{i,j,k,l}^{3N-6} \Phi_{ijkl} \, q_i q_j q_k q_l \ldots \,, \end{aligned} \tag{7.5}$$

with the n^{th} order force constants given by

$$\Phi_{ijk\ldots} = \frac{1}{n!} \left(\frac{\partial^n V}{\partial q_i \partial q_j \partial q_k \ldots} \right)_0 \,. \tag{7.6}$$

Cubic anharmonic force constants Φ_{ijk} describe the coupling between fundamental modes and overtone and combination bands (Fermi resonance), whereas the coupling between overtone or combination states themselves (Darling-Dennison coupling) is characterized by quartic force constants Φ_{ijkl}. The nuclear displacement coordinates q_i are usually chosen to be Cartesian, internal, or normal coordinates. Cartesian coordinates are well-defined and easy to use but molecular motion may be better visualized using internal coordinates. Internal coordinates such as bond lengths, bond angles, and dihedral angles are inherently localized as they are confined to 2, 3 and 4 atoms, respectively. The resulting force constants are usually diagonally dominant and facilitate transfer and comparison between related molecules. Isotope effects can be readily studied as effective masses for internal coordinates enter the vibrational Hamiltonian directly. However, curvilinear internal coordinates introduce strong couplings in the kinetic energy operator that are difficult to calculate for larger systems. When the force constants are related to spectroscopic observables, (dimensionless) normal modes are the most common choice. As normal modes are often delocalized, it is, however, difficult to relate them to microscopic (local) properties of the molecule. Delocalized force constants are not easily transferred from one molecule to another and – in contrast to Cartesian and internal coordinates – the mass-weighted normal modes only provide isotope dependent force fields.

While first and second order analytical derivatives of the potential energy surface are available for most popular quantum chemical methods [50], higher order force constants mostly have to be determined numerically, either by least-square fitting of pointwise calculated multidimensional potential energy surfaces [51] or by finite difference procedures [52–54]. Nonperturbative approaches to calculate anharmonic coupling such as the vibrational self-consistent field approach (VSCF) [55, 56], diffusive Monte Carlo methods [57, 58] or grid methods [59–61] have also been put forward.

The computational treatment of anharmonic coupling in hydrogen-bonded systems depends on the type of hydrogen bond. Weak hydrogen bonds with X−H stretching frequencies above $3200\,\mathrm{cm}^{-1}$ can often be sufficiently described in the harmonic approximation applying an empirical scaling factor, or, if not, by an one-dimensional anharmonic correction in the proton coordinate. Hydrogen bonds of intermediate strengths exhibit X−H stretching frequencies in the range of $2800\text{-}3100\,\mathrm{cm}^{-1}$. Here, the potential energy surface along the X−H···Y coordinate develops a shoulder or even a shallow well for a tautomeric X···H−Y configuration. The potential energy surface along the proton coordinate becomes broader, the barrier for proton transfer decreases, and the vibrational energy levels are spaced more closely leading to a larger frequency shift. Strong hydrogen bonds with X−H frequencies below $2700\,\mathrm{cm}^{-1}$ may even develop a single minimum potential energy surface with the zero vibrational energy level being above the barrier. In both medium-strong and strong cases, an explicit anharmonic treatment of at least the X−H and the X···Y coordinates is advisable. The latter coordinate reflects hydrogen bond stretching and/or bending modes.

Potential energy surfaces for nonreactive hydrogen bonds have been discussed until now. The description of reactive dynamics involving large-amplitude motion is conveniently done within the Reaction Surface Hamiltonian approach (for a recent review, see [32]). It combines the exact treatment of a few large-amplitude coordinates with the harmonic approximation for the majority of the degrees of freedom. In terms of the anharmonic expansion of the potential in the vicinity of a minimum this represents an approximation, that is, only certain terms in (7.5) are preserved [19]. The advantage, however, is that a full-dimensional simulation becomes possible as long as respective ab initio computations of the second derivative matrix can be carried out.

Derivatives of the dipole moment $\boldsymbol{\mu}$ in the coordinates q_i determine infrared intensities [62]:

$$\boldsymbol{\mu} = \boldsymbol{\mu}_0 + \sum_{i}^{N} \left(\frac{\partial \boldsymbol{\mu}}{\partial q_i} \right)_0 q_i + \sum_{i,j}^{N} \left(\frac{\partial \boldsymbol{\mu}}{\partial q_i q_j} \right)_0 q_i q_j + \ldots \quad . \tag{7.7}$$

Linear spectroscopy in the dipole approximation truncates the expansion after the linear term, an approximation that is also frequently adopted in nonlinear vibrational spectroscopy [6], although the influence of higher order terms on infrared intensities has been considered [63–65].

7.2.3.2 Quantum chemistry of hydrogen bonds

A large variety of theoretical methods including mechanical force fields, semi-empirical and ab initio methods have been applied to describe hydrogen bonding. The conceptually simplest approach is provided within the framework of classical mechanical force fields [66–68]. Some empirical mechanical force fields simply rely upon electrostatic and van der Waals interactions without explicit hydrogen bonding terms. Others modify the parameters and functional form of the van der Waals interaction, commonly a Lennard-Jones potential. In some cases directional terms such as $(\cos\theta^{XHY})^4$ are included as factors on the distance dependent parts in the Lennard-Jones potential to account for the hydrogen bond angle θ^{XHY}.

Among semiempirical electronic structure methods, older methods such as CNDO, INDO, MNDO and AM1 are considered inappropriate due to an overestimation of the exchange repulsion, whereas more recently developed semiempirical methods such as SAM1 and PM3 are regarded as reasonable methods for the description of hydrogen bond interactions [48, 69].

For ab initio methods the inclusion of electron correlation has been shown to be essential for an accurate treatment of hydrogen bonds [3, 70]. Hartree-Fock methods underestimate hydrogen bond energies and are thus inappropriate for a reliable description. In contrast, methods covering correlation effects explicitly such as second-order Møller-Plesset perturbation theory (MP2), configuration interaction (CI) or coupled-cluster (CC) methods are well suited to describe hydrogen bonding. In addition, sufficiently large basis sets, preferably of polarized triple-zeta quality with diffuse functions, have to be applied. The finite size of the basis set leads to a source of error in supermolecular calculations of intermolecular hydrogen bonding, the basis set superposition error, an artificial overestimation of the complexation energy. For very accurate treatments, this error may be approximately accounted for by the counterpoise correction [71, 72].

MP2, CI, and in particular CC methods such as CCSD(T) or CCSDT are capable of achieving very high accuracy, they are, however, computationally quite demanding and thus only affordably for smaller systems [73]. Therefore, approaches are being pursued to study hydrogen bonding with similar accuracy to MP2 or higher levels of theory, but with less computational effort. In particular, density functional theory (DFT) methods became very popular. Unfortunately, the accuracy of DFT to describe hydrogen bonding depends on the functional used to approximate the electronic exchange and correlation. DFT methods applying the generalized gradient approximations (GGA) or hybrid functionals have been shown to perform rather well in describing thermochemical, structural, and vibrational properties of hydrogen-bonded systems provided that sufficiently flexible basis sets are used [74]. DFT methods suffer from the inability to describe energy contributions stemming from dispersion forces [74]. This applies mainly to weak hydrogen bonds, hydrogen bond geometries deviating from linearity and extended hydrogen-bonded complexes [73, 75, 76]. However, attempts to explicitly include dispersion interaction into DFT methods are underway [77]. Some recently developed DFT functionals have also been shown to provide reasonably accurate energetic and geometric predictions for hydrogen bonds to π acceptors [78].

Approximate resolution of the identity (RI) MP2 methods, which are about one order of magnitude faster than exact MP2 methods, are capable of an accurate description of hydrogen bonds as well as systems, for which the proper treatment of dispersion interaction is essential, e.g. stacked base pairs [79].

An important and likewise challenging field is the simulation of extended hydrogen-bonded networks, e.g. liquids such as water or alcohols [80]. Many studies have used classical molecular dynamics with empirical potentials, often optimized to reproduce experimentally observable bulk properties [66, 81, 82]. In recent years, ab initio molecular dynamics have developed into a very powerful tool, which combines molecular dynamics with forces calculated on-the-fly from electronic structure calculations, in particular with DFT methods [83–86]. By this means ab initio molecular dynamics of liquid water [87–89], methanol [90] or hydrated protons in water [91–93] have been investigated. Because of considerable computational costs, ab initio molecular dynamics methods are restricted to small system sizes and short trajectories. Therefore, hybrid high-level/low-level approaches have been designed [94–96]. Hybrid methods include quantum effects for the electronically active region, whereas the environment is treated at a lower level of theory, either by lower level quantum mechanical methods (QM/QM) or by classical molecular mechanics (QM/MM).

7.3 Ultrafast nonlinear infrared spectroscopy

Ultrafast nonlinear infrared spectroscopy requires femtosecond pulses for resonant excitation and probing of vibrational transitions. Pulses of microjoule energy are necessary to induce a nonlinear vibrational response because of the comparably small cross sections of vibrational absorption on the order of $\sigma = 10^{-18} - 10^{-19}\,\mathrm{cm}^2$. So far, ultrafast dynamics of hydrogen bonds have been studied in the frequency range from 500 to 4000 cm^{-1} (wavelength range 20 to 2.5 µm) with the main emphasis on O−H and N−H stretching vibrations. Microjoule pulses with a duration of 40 - 250 fs have been generated throughout this range by nonlinear optical frequency conversion. A brief review of the relevant techniques has been given in [7].

Ultrafast vibrational spectroscopy does not only enable the determination of real time dynamics of vibrational states. With the bandwidth of the laser pulses the potential of exciting a collection of vibrational states into a coherent superposition can be explored as well [8, 9, 11, 13, 20–22, 24, 27]. The multilevel character and the coherent nature of X−H stretching excitations in hydrogen bonds have to be taken into account to describe the observed nonlinear signals.

Theoretical descriptions of nonlinear experiments often rely on perturbation theory [40, 47]. In addition to the material response, the applied light fields $E_i(t)$ interacting at three different times govern the third-order nonlinear polarization $P^{(3)}(t)$:

$$\begin{aligned} P^{(3)}(t) = & \int_0^\infty dt_3 \int_0^\infty dt_2 \int_0^\infty dt_1 \; S^{(3)}(t_3, t_2, t_1) \\ & \times E_3(t - t_3) E_2(t - t_3 - t_2) E_1(t - t_3 - t_2 - t_1) \,. \end{aligned} \tag{7.8}$$

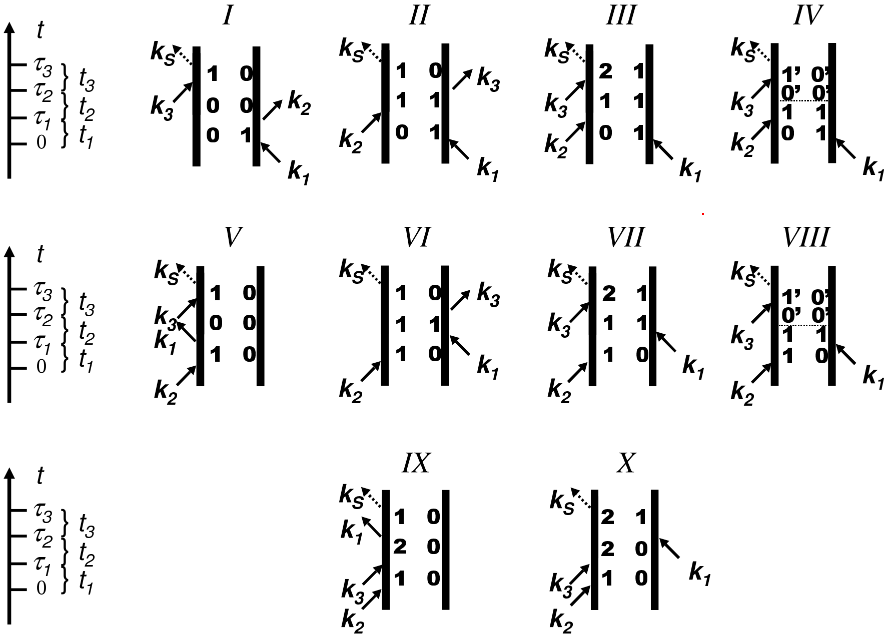

Fig. 7.4. Double sided Feynman diagrams used to describe nonlinear infrared experiments. Diagrams *I-IV* describe echo-generating (rephasing) Liouville space pathways, while diagrams *V-X* symbolize nonrephasing pathways. For two-level systems only diagrams *I, II, V*, and *VI* contribute, whereas diagrams *III, VII, IX* and *X* have to be added for three-level (vibrational ladder) systems. Diagrams *IV* and *VIII* take into account the population relaxation to a hot ground state, as indicated by the horizontal dashed line.

Here, $S^{(3)}(t_3, t_2, t_1)$ is the third-order response function:

$$S^{(3)}(t_3, t_2, t_1) = \sum_{\alpha=I}^{X} R_\alpha(t_3, t_2, t_1) \; , \tag{7.9}$$

which is a system property containing all information that potentially can be obtained from a system by means of third-order spectroscopy (for an application in electronic spectroscopy see Chapter 8) . To determine the different light-matter interactions that are possible in nonlinear vibrational experiments, double-sided Feynman diagrams are a standard means of depicting the possible Liouville space pathways. Due to the multilevel nature of hydrogen-bonded X−H oscillators 10 different diagrams often have to be considered (Fig. 7.4) [12,40,97].

Diagrams *I-IV* are denoted as rephasing pathways due to the time reversal of the system evolution in period t_3 after a coherence period t_1 and a population period t_2. Diagrams *V-X*, on the other hand, do not cause a rephasing.

Diagrams *III, VI, IX*, and *X* have to be implemented for vibrational ladder systems. Diagrams *II, III, VI*, and *VII* diminish in importance upon T_1 (population) relaxation. Diagrams *IV* and *VIII* have been implemented to describe an effective five level system of hydrogen-bonded X−H stretching vibrations (see Sect. 7.3.1). For each Liouville space pathway $\alpha = I, .., X$ a specific material response function $R_\alpha(t_3, t_2, t_1)$ can be defined, depending on the particular diagonal and off-diagonal elements of the density operator through which the system evolves in the three different time periods. Explicit equations can be found in Sect. 3.2 in the overview [7]. In the following different forms of nonlinear vibrational spectroscopy that have been pursued in the investigation of hydrogen bond dynamics are described.

7.3.1 Pump-probe spectroscopy

Pump-probe spectroscopy is conventionally used to follow the population kinetics upon an excitation of the $v(\nu_{XH}) = 0 \rightarrow 1$ transition. This implies that measurements are made in the well-separated pulse regime, i.e. when pump and probe pulses do not overlap in time and additional signal contributions caused by alternate order in the field interactions can be discarded [47]. In this well-separated pulse regime the time-dependent populations can be followed using a probe pulse in spectrally integrated fashion (with a single detector) or, by taking advantage of the large pulse bandwidth, after spectral dispersion with a monochromator (Fig. 7.5a-c). In the case of Fig. 7.5a the spectrally integrated absorption change $\Delta\alpha(\omega_{pr})$ measured by a probe pulse with carrier frequency ω_{pr} is proportional to [47, 98]:

$$\Delta\alpha(\omega_{pr}) \propto \frac{\operatorname{Im} \int_{-\infty}^{\infty} dt\, E_{pr}^*(t) \times P^{(3)}(t)}{\int_{-\infty}^{\infty} dt\, |E_{pr}(t)|^2} \,. \tag{7.10}$$

Here $E_{pr}(t)$ is the time-dependent electrical field of the probe pulse and $P^{(3)}(t)$ is given by (7.8). For spectrally resolved detection of the probe pulse (Fig. 7.5b,c), the measured signal is given by:

$$\Delta\alpha(\omega_{pr}) \propto \frac{|E_{pr}(\omega)|^2 \operatorname{Im}\left(P^{(3)}(\omega)/E_{pr}^*(\omega)\right)}{\int_0^{\infty} d\omega\, |E_{pr}(\omega)|^2} \,. \tag{7.11}$$

As a consequence of a significantly large diagonal anharmonicity of X−H stretching vibrations, the $v(\nu_{XH}) = 0 \rightarrow 1$ and $v(\nu_{XH}) = 1 \rightarrow 2$ transitions are centered at different spectral positions [40], separated by an anharmonic shift of up to several hundreds of wavenumbers (see Fig. 7.6). Thus, after excitation of the X−H stretching vibration, one observes the ground state $v(\nu_{XH}) = 0 \rightarrow 1$ bleaching and excited state $v(\nu_{XH}) = 1 \rightarrow 0$ stimulated emission, both leading to a decrease of absorbance at the frequency position of the X−H stretching band observed in the linear IR spectrum. In addition,

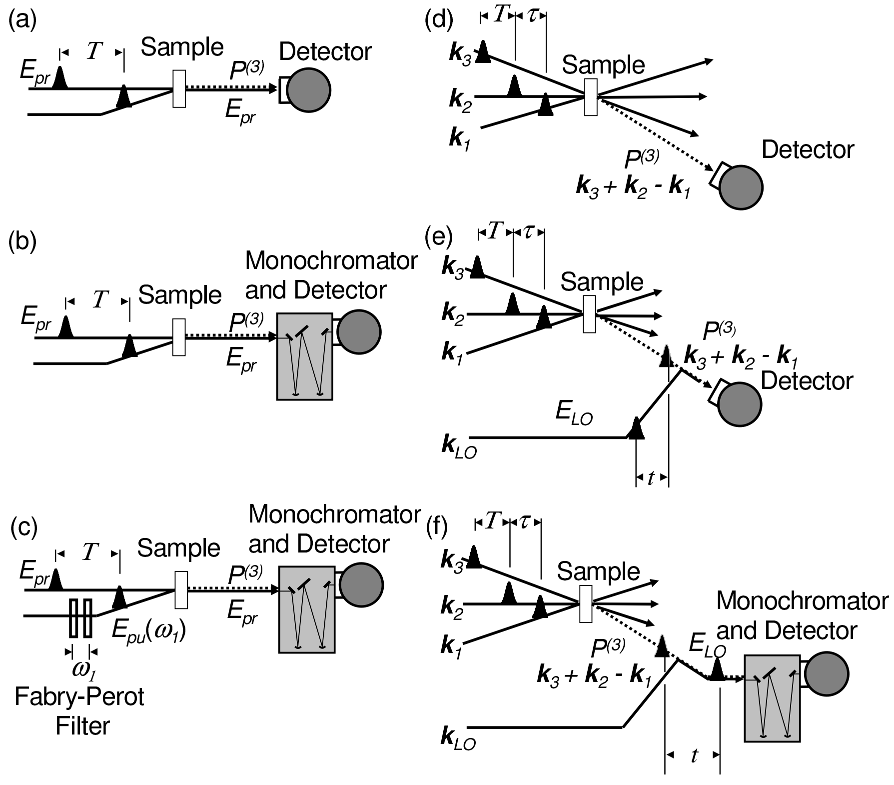

Fig. 7.5. Schematics of nonlinear spectroscopy techniques: (a) spectrally integrated pump-probe; (b) spectrally resolved pump-probe; (c) 2D-IR pump-probe; (d) homodyne (intensity) detected photon echo; (e) heterodyne (amplitude) detected photon echo with local oscillator LO; (f) heterodyne (amplitude) detected photon echo using spectral interferometry with local oscillator (2D-FT-IR).

a transient red-shifted absorption occurs on the $v(\nu_{XH}) = 1 \rightarrow 2$ transition, decaying upon $v(\nu_{XH}) = 1$ population relaxation.

From a large collection of experimental work the conclusion has been drawn that the $v(\nu_{XH}) = 1$ state does not relax directly back to the $v(\nu_{XH}) = 0$ state, leading to a disappearance of the bleach signals [8,9,12,13,20,24,99–101]. Instead, the short-lived $v(\nu_{XH}) = 1$ state, often with sub-picosecond lifetimes, redistributes vibrational excess energy into other modes actively involved in the hydrogen bond motions, such as the X−H bending and the hydrogen bond low-frequency modes (Fig. 7.6). Subsequently, energy dissipation to the solvent (vibrational cooling) occurs on longer time scales on the order of picoseconds to hundreds of picoseconds. In this hot ground state configuration the X−H stretching mode is not excited, but its transition $v(\nu_{XH}) = 0' \rightarrow 1'$ is frequency up-shifted due to anharmonic coupling to the transiently highly

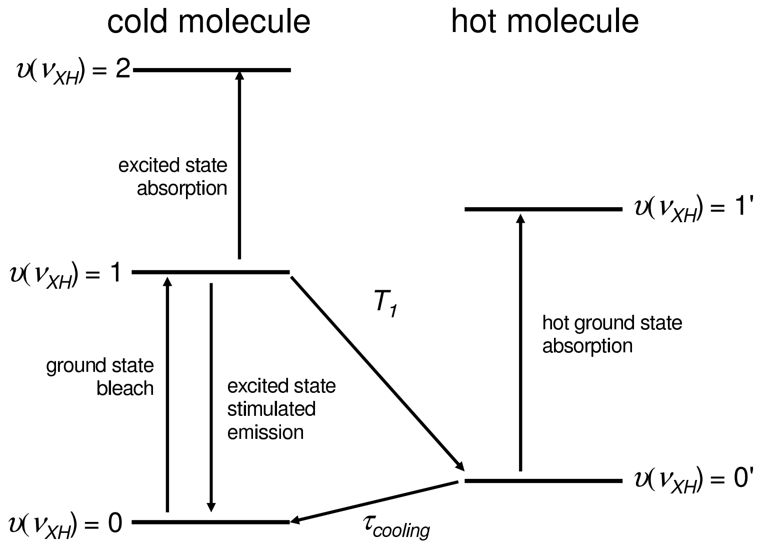

Fig. 7.6. Level structure implementing the $v(\nu_{XH}) = 0$, $v(\nu_{XH}) = 1$, and $v(\nu_{XH}) = 2$ states of the X–H/X–D stretching mode, as well as the two levels of the hot molecule generated upon population relaxation of the $v(\nu_{XH}) = 1$ state.

populated hydrogen bond modes. In contrast, when X–H bending vibrations relax into the hot ground state upon intramolecular vibrational energy redistribution (IVR), red-shifting is observed [25,28,31], in accordance with more typically found negatively valued anharmonic couplings between intramolecular vibrational modes [62,102,103].

Besides the investigation of population dynamics, pump-probe spectroscopy can be used to examine coherent vibrational dynamics. The anharmonic coupling between the X–H stretching and low-frequency hydrogen bond modes allows for the preparation of a coherent superposition of vibrational eigenstates of these low-frequency modes by exciting the stretching vibration with a broadband pump pulse (see Fig. 7.2a). This effect has been explored in medium strong hydrogen-bonded molecular systems (see Sect. 7.5).

Finally, the probe pulse can also be tuned to the fingerprint region [23,25]. In this two-color pump-probe experiment one can follow the dynamics of fingerprint vibrations upon excitation of the X–H stretching mode. Here the idea is to explore the population kinetics after the decay of the $v(\nu_{XH}) = 1$ state, where the IVR pathways and vibrational energy dissipation into the solvent are of main interest. Population relaxation of X–H stretching vibrations in hydrogen-bonded systems is of ultrafast nature, because the $v(\nu_{XH}) = 1$ state is close in energy to the bending $v(\delta_{XH}) = 2$ overtone state (Fig. 7.3a,b), but also other overtone and combination levels may play a role. These overtone and combination states may facilitate vibrational energy relaxation pathways. It should be noted that changes of vibrational population induced by an IR pump pulse have also been probed by spontaneous anti-Stokes Raman scattering of a visible or near-infrared pulse [104–106]. The detection of the weak Raman signals remains a challenge, even when resonance enhancement is used by tuning the Raman probe pulse to an electronic transition [106].

7.3.2 Photon-echo spectroscopy

Femtosecond four-wave mixing spectroscopy allows for directly monitoring the macroscopic nonlinear polarization dynamics [107, 108], with which the coherence dynamics of X−H stretching vibrations can be followed in real-time [10,12,21,22,26,27,109–121]. In general, vibrational photon echo spectroscopy involves the resonant interaction of two or three laser pulses with carrier frequencies ω_i and propagation directions k_i (see Fig. 7.5d-f). Here the first pulse generates a coherent superposition of the $v(\nu_{XH}) = 0$ and $v(\nu_{XH}) = 1$ states, which then evolves during the first pulse delay period (coherence time τ). A second pulse converts the phase information into a frequency population grating in the $v(\nu_{XH}) = 0$ and $v(\nu_{XH}) = 1$ states. After a second pulse delay period (population time T) a third pulse converts the phase information again into a coherence. When the phase information has not been lost due to dephasing and spectral diffusion a macroscopic photon echo signal appears in the phase-matched directions $k_3 + k_2 - k_1$ and $k_3 - k_2 + k_1$. The photon echo signal can either be homodyne-detected in a time integrated way (Fig. 7.5d):

$$I_{hom}(\tau, T) \propto \int_{-\infty}^{\infty} dt \left| P^{(3)}(\tau, T, t) \right|^2 , \tag{7.12}$$

or heterodyne-detected by convoluting it with a fourth phase-locked light pulse serving as local oscillator (LO). The heterodyne-detected signal can either be recorded by scanning the pulse delay between echo and local oscillator (Fig. 7.5e) [122]:

$$I_{het}(\tau, T, t) \propto \mathrm{Im} \int_{-\infty}^{\infty} dt' \left\{ E^*_{LO}(t' - t) P^{(3)}(\tau, T, t') \right\} , \tag{7.13}$$

or by Fourier transforming the signal with a monochromator and recording it as a spectral interferogram (Fig. 7.5f) [123]:

$$S_{het}(\tau, T, \omega_3) \propto \mathrm{Re} \left\{ E^*_{LO}(\omega_3) P^{(3)}(\tau, T, \omega_3) \right\} , \tag{7.14}$$

that can be converted into a two-dimensional spectrum:

$$S_{het}(\omega_1, T, \omega_3) \propto i \, \mathrm{sign}(\omega_3) \int_{-\infty}^{\infty} d\tau P^{(3)}(\tau, T, \omega_3) \exp(i\omega_1 \tau) , \tag{7.15}$$

provided the relative phase between the LO and signal fields has been determined.

Different aspects of the vibrational dynamics can be probed by a specific choice of pulse delays τ and T. These different situations are:

1) *Transient grating (TG) scattering,* where the first pulse delay $\tau = 0$. A population grating is generated by pulses 1 and 2, and the signal diffracted from this grating as function of pulse delay T, is a direct measure of processes affecting this grating, such as population relaxation or rotational diffusion [124–126].

2) *Two pulse photon echo (2PE),* where the second pulse delay $T = 0$. A macroscopic polarization due to a coherent superposition generated by the first pulse is allowed to dephase during the coherence time τ, after which the interactions with pulses 2 and 3 invert the coherent superposition, and a rephasing of the macroscopic polarization can occur [10, 127–129]. Only when inhomogeneity exists during the pulse sequence, a macroscopic photon echo is generated.

3) *Three pulse photon echo (3PE),* where both pulse delays τ and T are scanned. With a 3PE photon echo signal one can fully explore the dephasing and spectral diffusion dynamics affecting the spectral line shapes [130].

4) *Three pulse echo peak shift (3PEPS),* where the maximum of the echo signal along the coherence time τ is monitored as function of the population time T [12, 131, 132]. The decrease of this signal directly reflects the diminishing of the spectral inhomogeneity in time. For two-level systems it has been shown that the 3PEPS-signal mimics the frequency fluctuation correlation function $C(t)$ for pulse delays T at which temporal overlap between the three pulses is negligible.

5) *Two-color three pulse photon echo (2ω3PE),* where phase information is written into the inhomogeneously broadened transition of one particular transition, and afterwards detected by generating an echo from a second molecular transition by the third pulse [133]. This experimental configuration may provide insight into correlated frequency fluctuations for two molecular vibrations [120, 134, 135], e.g., the same microscopic solvent motions may be responsible for phase memory loss for the X−H stretching and X−H bending vibrations in a particular hydrogen bond.

7.3.3 Multidimensional spectroscopy

Until now well-established nonlinear spectroscopic techniques have been described providing insight into the vibrational dynamics of hydrogen-bonded systems, such as IVR, population relaxation, coherent wave packet motions, dephasing and spectral diffusion. Typically the information obtained is depicted in the time domain. However, the multilevel nature of the molecular vibrations that characterize hydrogen bonds has still many features that necessitate novel methodology, e.g., to elucidate questions such as the connectivity of energy levels, the cross relaxation between levels and the discrimination between different mechanisms of dephasing. Recent developments in multidimensional infrared spectroscopy have led to significant advances in deciphering the dynamics of complex multilevel systems. In these multidimensional nonlinear techniques the information on the molecular systems is typically mapped out in the frequency domain. Most papers in the field of multidimensional infrared spectroscopy treat the response of amide I vibrations in peptides and proteins [40, 122, 136], as well as other systems [65, 137], and recent extensions use the structure resolving method on transient states [138, 139]. The purpose of this section is to indicate different methodological approaches for multidimensional spectroscopy and to provide the underlying similarities in terms of information obtained, and differences with respect to experimental limitations.

In NMR spectroscopy multidimensional nonlinear techniques have been extremely successful in the study of such properties [140]. The transferability of the concepts of multidimensional NMR spectroscopy to IR spectroscopy has been postulated already in the earliest publications on two-dimensional NMR [141], however, the first two-dimensional IR spectrum was measured only recently [142]. The essential idea of 2D-IR spectroscopy is the following: A relatively narrow band pump-pulse, or a sequence of two subsequent broad band pulses, excite a vibrational state, and a delayed probe pulse measures the response of the directly pumped transition, as well as that of any other transition. The first response gives rise to a so-called diagonal contribution, whereas the second response gives rise to a cross-peak (off-diagonal peak), which reports on the connectivity of pumped and probed transitions. It has been shown that the connectivity between two states can be related to the geometry of a molecule, as well as to exchange processes between various conformations of a molecular system. In particular, the connectivity can be related to local contacts, which is the basic principle of structure determination both in 2D-NMR and 2D-IR spectroscopy. All basic NMR experiments (EXSY, NOESY) have been demonstrated also in the IR range, with the important difference that the IR experiment is intrinsically the – by many orders of magnitudes – faster method. This allows one to follow or to freeze in even the fastest motions of molecular systems on a picosecond or even faster timescale.

While this first 2D-IR experiment was a quasi-frequency domain double resonance experiment, a technique that has been developed further [135, 136, 138, 139, 143–147], time domain pulsed Fourier transform IR techniques have been devised meanwhile, mostly applied to amide I and carbonyl stretching vibrations [65, 122, 137, 148–153], but also on X−H/X−D stretching vibrations [26, 27, 97, 109–121, 154–158]. In the following the frequency and time domain approaches of 2D-IR spectroscopy, concerning the potential information content as well as regarding technical issues, are compared.

The principles of the two experimental implementations of 2D-IR spectroscopy are shown in Fig. 7.5:

1) *Double-resonance spectroscopy (also called dynamic hole burning):* The double-resonance experiment is essentially a conventional pump-probe experiment (Fig. 7.5c). An intense ultrashort (typically 100 fs) IR laser pulse

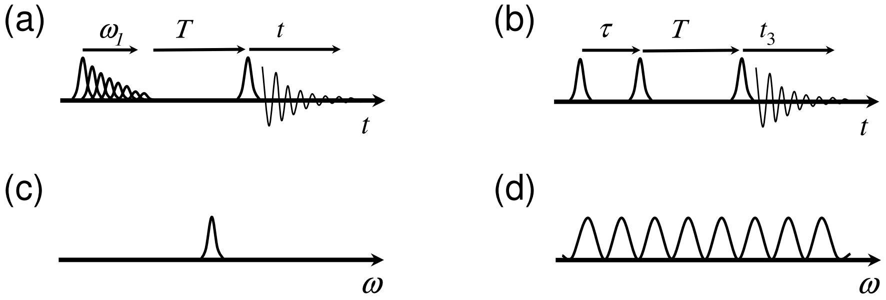

Fig. 7.7. Frequency vs. time domain 2D-IR method. Pulse sequence of the double resonance experiment of Fig. 7.5c in the time domain (a) and in the frequency domain (c). The corresponding representation of the pulsed Fourier transform experiment of Fig. 7.5e is shown in (b) in the time domain and in (d) in the frequency domain.

[159, 160], the bandwidth of which ($\approx 200\,\mathrm{cm}^{-1}$) covers the whole spectral range of interest, is split into a pump and a probe beam. The difference between the double-resonance experiment and the conventional pump-probe experiment of Fig. 7.5b is the adjustable Fabry-Perot filter which the pump beam passes before reaching the sample. It consists of two partial reflectors separated by a distance which is regulated by a feedback-controlled piezo-electric mount. It slices out a narrow-band pump pulse (typical bandwidth 5-15 cm^{-1}), the center frequency of which is controlled by the computer. In this way two frequencies are defined, the center frequency of the pump pulse and the probe frequency. These are the frequency axes used in the 2D-IR spectrum. Hence, in a 2D-IR spectrum, each (horizontal) cut in the probe frequency direction represents a transient absorption spectrum obtained by pumping at the frequency on the pump (vertical) axis.

2) *Pulsed Fourier transform 2D spectroscopy (also called heterodyne-detected photon echo spectroscopy):* The pulsed Fourier transform experiment is based on a three-pulse photon echo experiment, as described in the previous section (Fig. 7.5e,f). The generated third-order field is 2D-Fourier transformed with respect to times τ (the time between the first and the second pulse) and t (the time after the third pulse), generating a 2D-IR spectrum as a function of two frequencies ω_1 and ω_3. In order to perform the Fourier transform, one needs to know the electric field irradiated by the third-order polarization (see (7.8)), rather than the time-integrated intensity, which is what 'normal' square law detectors measure. This is the reason for using the heterodyne-detected version of photon echo spectroscopy (Fig. 7.5e,f). The interferometric superposition of echo signal and local oscillator can either be performed in the time domain (by scanning the time and phase of the local oscillator) or in the frequency domain (by spectrally dispersing both beams in a spectrograph). The outcome of the interferometric superposition depends on the optical phase

between first and second pulse as well as of the third and local oscillator pulse, $(\phi_1 - \phi_2) + (\phi_3 - \phi_{LO})$, which is why the requirements on the mechanical stability of the setup and an accurate measurement of the phase are high. Schemes utilizing intrinsic [123] and active [161] phase stabilization have been proposed recently.

Principally speaking, the two types of experiments can be looked at both in the time (Fig. 7.7a,b) and in the frequency (Fig. 7.7c,d) domains and both are connected through a simple Fourier transformation. Yet, the more intuitive picture is the frequency domain picture for double-resonance spectroscopy and the time domain picture for pulsed Fourier transform spectroscopy. In the double-resonance experiment, a (relatively) narrow band pump pulse frequency selectively excites a transition (i.e. burns a hole), and a broad band probe beam probes the response of other (but the excited) transitions. If such a response exists, a cross peak shows up in the 2D-IR spectrum, which reports on the connectivity of pumped and probed transition.

For pulsed Fourier transform spectroscopy, where the natural language works in the time domain, a frequency domain picture can also be adapted: The pulse sequence of first two pulses produces a frequency grating with a spacing that depends on the coherence time τ. That is, the pulse sequence produces a 'hole-burning' pulse with sinusoidal shape (Fig. 7.7d), and one needs a Fourier transform to regain the spectral information. In the same way, one could also look at the double resonance experiment in the time domain, where the Fabry-Perot filter produces a sequence of exponentially decaying phase-locked pulses (Fig. 7.7a).

Almost all optical 2D experiments published so far are third-order experiments in the weak field regime, in which a power expansion of the nonlinear response in terms of the electric field of the incident pulses is well justified [47] (exception to the rule is the reported optical 2D spectral study of atomic Rb vapor that is clearly not in the weak field regime [162]). It is important to note that the emitted polarization $P^{(3)}(t)$ of (7.8) is *linear* with respect to the field of each interaction E_i. Therefore, at least principally speaking, the information content of frequency and time domain approaches are absolutely identical and are connected through a simple Fourier transformation. It is mostly practical issues by which both methods differ.

In the case of NMR, pulsed Fourier transform methods became much more widespread than frequency domain methods soon after their introduction, partly due to greater sensitivity because of their multiplex advantage, but also due to their greater experimental versatility. However, it is important to keep in mind that modern NMR spectroscopy works in the limit of strong fields ($\pi/2$ and π pulses in most cases). Hence, in contrast to 2D-IR spectroscopy, a simple Fourier relation between time-domain and frequency domain experiments does in general *not* exist.

7.4 Disordered hydrogen-bonded liquids

Most ultrafast infrared spectroscopic studies on ultrafast structural dynamics of hydrogen-bonded liquids have until now dealt with isotopically diluted samples, e.g. either X−H stretching vibrations in a solvent bath consisting of X−D oscillators, or vice versa. Isotopically diluted samples avoid the experimental limitation of handling extremely thin samples due to the large IR cross sections in neat liquids. However, isotopic dilution implies different vibrational systems, accompanied by different energy levels and couplings that may have different vibrational dynamics. In this Section the discussion on disordered hydrogen-bonded liquids first focuses on results obtained on the coherent response of isotopically diluted water and neat liquid water, before discussing vibrational energy redistribution and relaxation of water. The Section concludes with an example of chemical exchange in hydrogen-bonded systems. An extensive discussion on other hydrogen-bonded liquids is given in the recent overview [7].

7.4.1 Coherent response of isotopically diluted water

Protic solvents, such as water and alcohols, form extended hydrogen-bonded networks connecting the molecules that are, however, continuously changing in configuration and hydrogen bond strengths. As a result, the correlation between hydrogen bond distance (strength) and IR transition frequency of the X−H stretching oscillator [33–35, 163, 164] becomes somewhat blurred [165–167], and additional orientational parameters, such as the hydrogen bond angle, play a role [165, 166]. Nevertheless, when a particular molecule has its X−H stretching frequency at a particular value, it corresponds to a particular hydrogen bond structure. Dynamical properties of the X−H stretching oscillator, such as dephasing, spectral diffusion, anisotropy decay, and population relaxation, are thus intimately correlated to fluctuations in the hydrogen bond network.

Water has attracted the most attention in the family of protic solvents, because of its utmost important role in nature. The structure and dynamics of water as a liquid remains an intense subject of debate as indicated by recent numerous studies ranging from experiment [168–172] to theory [81, 173–176]. Until now most studies on the vibrational dynamics of hydrogen bonds in water have focused on the dephasing and spectral diffusion of isotopically diluted water, i.e. on the O−H stretching transition of HOD in D_2O, and on the O−D stretching band of HOD in H_2O. The first photon echo on HOD in D_2O was reported by Stenger et al. (Fig. 7.8) [10], where the fast dephasing time of 90 fs was ascribed to the combined effect of large diagonal anharmonicity of the O−H stretching oscillator and the fast solvent fluctuations of D_2O [177, 178]. For the HOD/D_2O system a full determination of the frequency fluctuation correlation function $C(t)$ has been achieved with three pulse photon echo peak shift (3PEPS) measurements using homodyne detection. In the early work by

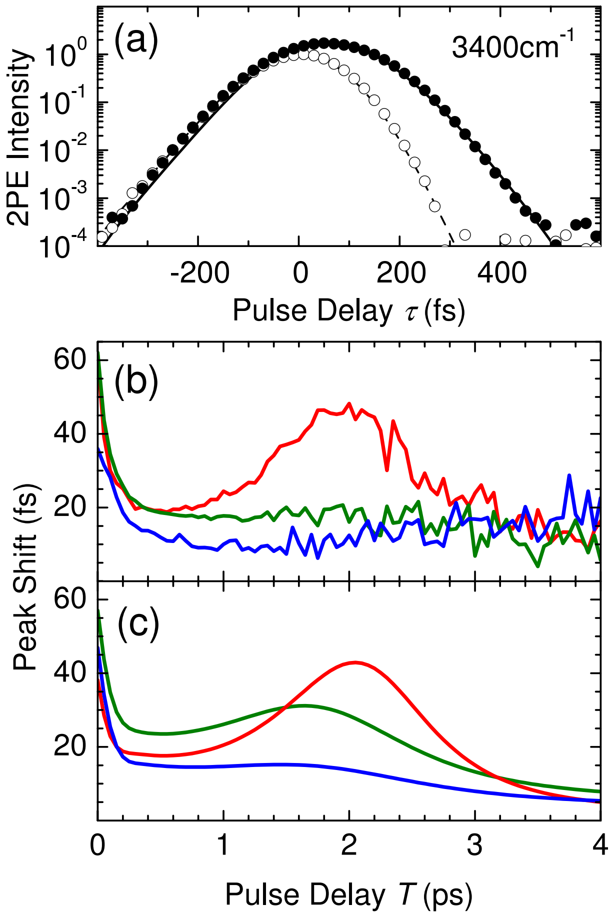

Fig. 7.8. (a) Homodyne detected 2PE signal of HOD in D_2O (*solid dots*), as recorded by tuning the excitation pulses near the maximum of the O−H stretching band. The *open circles* indicate the time resolution as measured in a CaF_2 sample. The *solid line* is a fit of the echo data assuming homogeneous broadening ($T_2 = 90\,\text{fs}$) and frequency fluctuations on (sub)picosecond time scales; (b) 3PEPS signals of HOD in D_2O recorded by excitation at 3300 (*red line*), 3400 (*green line*) and $3500\,\text{cm}^{-1}$ (*blue line*); (c) Calculated 3PEPS signals, where the frequency correlation function $C(t)$ was described using an instantaneous δ-component (leading to an effective $T_2 = 90\,\text{fs}$), and two components with 700 fs and 15 ps decay constants.

Stenger et al. the bandwidth of the laser pulses was smaller than the O−H stretching line width of HOD in D_2O (pulse duration ∼ 150 fs) [12]. A time dependence of the 3PEPS-signal was reported with a delayed rise on a time scale of 1-2 ps for excitation on the low-frequency side of the O−H stretching band that clearly does not mimic the temporal behavior of $C(t)$ (see Fig. 7.8).

Using the five level system of Fig. 7.6, this effect has been explained to be the result of a cancellation effect, decreasing its magnitude as function of the population lifetime T_1, of signal contributions described by Liouville space pathways that follow the ground state (diagram *I* of Fig. 7.4) and those that follow the excited state (diagrams *II* and *III* of Fig. 7.4) during the population time period T. In contrast, when much larger pulse bandwidths are used (pulse duration $\sim 50\,\text{fs}$), covering approximately the full fundamental $v(\nu_{OH}) = 0 \rightarrow 1$ O−H stretching band as well as most of the $v(\nu_{OH}) = 1 \rightarrow 2$ excited state absorption, a delayed rise has not been detected in 3PEPS measurements [111, 112, 179]. It appears that the cancellation effect will be less pronounced when the laser bandwidth covers the resonances of the fundamental $v(\nu_{OH}) = 0 \rightarrow 1$ and excited state $v(\nu_{OH}) = 1 \rightarrow 2$ transitions. The same approach of Stenger et al. has recently been used to interpret the results of a photon echo spectroscopic study of the dephasing and spectral diffusion dynamics of the N−H stretching mode of DCONHD in deuterated formamide $DCOND_2$ [97].

From the 3PEPS experiment by Stenger et al. a temporal behavior $C(t)$ has been derived that has been approximated with three time components ($\delta(t)$ (i.e. an infinitely small time constant), 700 fs and 5-15 ps). In the same work it has been noted that an equally satisfying simulation result had been obtained by using two time components ($\delta(t)$ and 2 ps) [12]. Recent echo measurements on the O−H stretching transition of HOD/D_2O with improved time resolution have led to the determination of the multicomponent temporal behavior of $C(t)$, with the shortest characteristic time constant ranging from 50-130 fs, whereas the long tail approximates an exponential decay behavior with a 1-1.5 ps time constant [109, 111, 112, 179]. Similar behavior has been found for the O−D stretching band for HOD in H_2O [113–115]. Since the O−D stretching lifetime T_1 of HOD in H_2O is $\sim 1.8\,\text{ps}$ as opposed to $\sim 0.7\,\text{ps}$ for the O−H stretching excited state for HOD in D_2O, the echo decay can be probed for a larger time range before the effects of the energy redistribution and thermalization set in.

Only in the case of HOD/D_2O 3PEPS measurements have been reported to show a recurrence with a period of 180 fs, suggesting that the O−H stretching mode of HOD is anharmonically coupled to the low-frequency hydrogen bond stretching mode that is underdamped with a frequency of $160\,\text{cm}^{-1}$ [111, 112, 179]. A low-frequency recurrence has not been reported for the case of HOD/H_2O even though a similar time resolution was effective [113–115], which may hint at a smaller magnitude of anharmonic coupling between the O−D stretching vibration and the hydrogen bond stretching mode with the surrounding solvent.

More insight can be obtained by comparison of experiment and theory. For the latter mixed quantum/classical studies have been pursued. Until now only numerical studies of vibrational dynamics in isotopically diluted water have been reported. Here the intramolecular modes of the solute HOD (O−H and O−D stretching and the H−O−D bending modes) have been treated quantum mechanically, whereas the remaining degrees of freedom, in particular the hydrogen bond modes, have been treated classically. Whereas it seems plausible to describe the low-frequency translational hydrogen bond stretching modes between solute and solvent classically, this is not warranted for the librational (hindered rotational) modes, that typically have frequencies between 500-800 cm^{-1}, with a tail extending up to 1600 cm^{-1}. Several numerical approaches have been reported with which one can describe the vibrational dynamics. In one class of simulations the same molecular dynamics (MD) force field has been applied to describe solvent, solute and the solute-solvent interaction. This has been used to describe the water monomer and static water clusters [180–183]. In another class of calculations a classical MD field describes the solvent and solute-solvent interaction, whereas the solute vibrations are subject to a different field adapted to fit experimental findings [165–167, 184, 185]. In this approach polarizable force fields can be implemented [115, 186]. In a third class of modeling an MD force field is applied on the solvent only. The solute-solvent interaction and the solute have been estimated by a map accounting for the electrostatic field generated by the solvent field [111, 112, 187, 188]. The importance of electrostatic fields on the vibrational line shapes and nonlinear response has been recognized [111, 112, 189, 190]. Quantum corrections need to be considered in the calculation of vibrational line shapes and the nonlinear response [191]. Comparison between experiment and numerical simulations have led to the conclusion that the temporal behavior of $C(t)$, in particular the extended tail on picosecond time scales, is better described with polarizable water models [115, 186, 188].

Comparison between experiment and theory provides insight into the underlying mechanisms that dictate the temporal behavior of $C(t)$. It should be emphasized that dissection of $C(t)$ into a number of exponentially decaying functions does not necessarily imply an equal amount of underlying microscopic processes. The long time tail of $C(t)$ has been associated with more drastic rearrangements of hydrogen bonds, such as hydrogen bond breaking and formation [113, 115, 166] and rotational diffusion [166, 192] of the solute HOD molecule, but also more collective hydrogen bond network rearrangements [112, 188]. The recurrences at early times have been ascribed to underdamped motion of the translational stretching mode [111, 112, 165, 166]. Faster dynamics on a time scale of ~50 fs also appears in the calculated correlation functions. However, as librational modes have not been explicitly implemented in the numerical routines, one cannot directly assign these early time dynamics in the calculated $C(t)$ to be due to librational motions. Thus, to validate the proposed explanation for the fastest dynamics observed in 3PEPS experiments on HOD/D_2O [112, 179], and in 2D photon echo experiments on neat H_2O [26] (see below), it is important to include librational modes explicitly in the numerical studies.

As a final note it should be mentioned that work has been reported on two-dimensional infrared photon echo spectroscopy of the hydrogen bond dynamics of methanol-OD oligomers [118, 119, 155] and of N,N-dimethylacetamide and pyrrole in benzene solution [120].

7.4.2 Coherent response of neat liquid water

The vibrational dephasing and spectral diffusion of neat water has only recently been addressed in a heterodyne detected photon echo experiment [26]. The high optical density of the O−H stretching mode in neat H_2O and parasitic window signals in conventional samples have so far hindered attempts to access the fastest relaxation processes of liquid water. In the photon echo study of neat liquid water it has been shown that thin (800 nm) Si_3N_4 windows negligibly contribute to the nonlinear response. As a result the fastest dynamics of water (500 nm thickness) at room temperature has now been determined with 70 fs time resolution. From these experiments it has been possible to temporally resolve for the first time the anisotropy decay (occurring with a 75 fs time constant), providing insight into the coupling strengths between neighboring water molecules (Fig. 7.9). Earlier reported work has only indicated an upper limit for the anisotropy decay in neat water [193]. The spectrally resolved grating scattering and the 2D correlation spectra (Fig. 7.10) show that spectral diffusion fully occurs within 50 fs. This is much shorter than the time scale on which the hydrogen bond stretching mode can respond to excitation of the hydrogen O−H stretching oscillator (∼200 fs period of a low-frequency of 170 cm^{-1}), whether underdamped or overdamped. Only librational modes, strongly coupled to the O−H stretching oscillator, and highly susceptible to

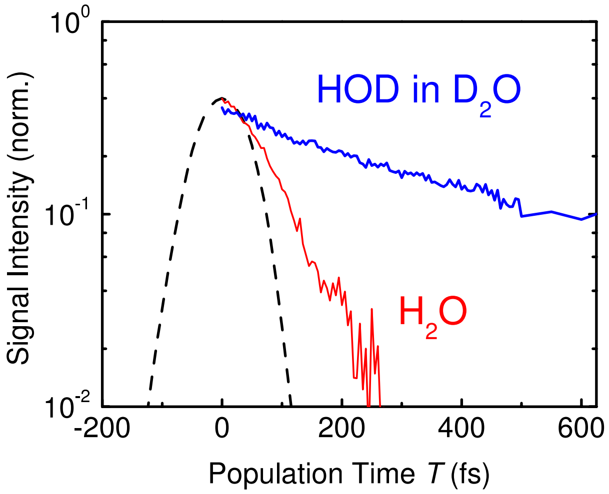

Fig. 7.9. Anisotropy decay of the transient grating scattering signal of the O−H stretching transition of neat H_2O (*red line*) and of 13 M HOD in D_2O (*blue line*). The temporal resolution is indicated by the *black dashed curve*.

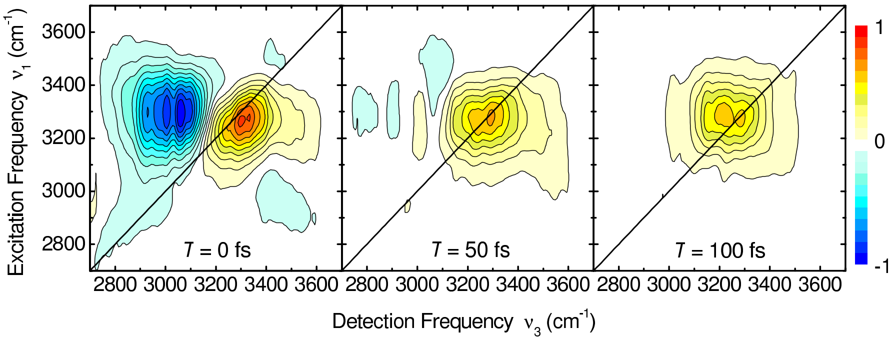

Fig. 7.10. Absorptive components of the three-pulse photon echo signal of pure H_2O for population times $T = 0, 50$ and $100\,\mathrm{fs}$. The inhomogeneity, as indicated by the skewness of the positive peak along the diagonal in the $T = 0\,\mathrm{fs}$ spectrum, has almost completely disappeared in the $T = 50\,\mathrm{fs}$ plot, clearly indicative of the rapid dephasing and ultrafast memory loss of the O−H stretching polarization in H_2O.

the fluctuating hydrogen bond network, can be assigned as the reason for this ultrafast spectral diffusion. These recent experimental results on neat water emphasize the necessity of theoretical studies on the determination of the couplings of librational modes with the O−H stretching oscillator [194], as well as intermolecular resonant vibrational energy transfer [195, 196], fluctuations of the hydrogen bond network of neat water [176, 197], and reorientational dynamics [198].

7.4.3 Vibrational energy redistribution and relaxation of O−H/O−D stretching and bending vibrations in water

When a molecular vibration is excited, couplings with the other molecular normal modes cause IVR, and intermolecular vibrational excitation exchange (vibrational energy relaxation, VER) [199–201]. IVR may lead to recurrences in vibrational excitation for isolated small molecules in the gas phase. The sizeable number of degrees of freedom in large molecules provide an efficient intramolecular heat bath. For VER to surrounding molecules, e.g., solvent shells, the vibrational energy transfer occurs in one direction and a true dissipation takes place. The anharmonicities of molecular vibrations involved in the hydrogen bond are significant. As a result, these vibrational modes (e.g., in-plane and out-of-plane X−H bending, librational and hydrogen bond stretching modes) are the first candidates to accept the vibrational energy corresponding to one quantum of X−H/X−D stretching vibration. This vibrational redistribution process occurs on ultrafast time scales: the X−H/X−D stretching oscillator in a hydrogen bond has a vibrational population time T_1 of $\sim 1\,\mathrm{ps}$ or less [7], typically much faster than VER to the solvent, and certainly faster than the time scale of a full thermalization of the vibrational excess energy, i.e., when a Boltzmann distribution is reached over all vibrational modes of solute and solvent with an elevated temperature. Despite the fact that only in the case when a full equilibration is reached, and a vibrational temperature can be defined, the situations of elevated population numbers of a fraction of intramolecular vibrational modes – while the X−H/X−D stretching vibration has returned to the $v(\nu_{OH}) = 0$ state – have been described as hot ground states (cf. Sect. 7.3.1 and Fig. 7.6).

The magnitude of anharmonic couplings of the X−H/X−D stretching oscillator with other modes dramatically increase with increasing hydrogen bond strength. The increased frequency down-shift of the X−H/X−D stretching band with increasing hydrogen bond strength may lead to a more efficient Fermi coupling with the X−H/X−D first overtone band, and often this has been assumed to be the relaxation pathway for the X−H/X−D stretching excitation, although direct evidence that IVR occurs along this pathway has until now been only scarcely reported (see Sect. 7.5.2) [25].

Water has three intramolecular degrees of freedom [62,104]. For HOD these are the O−H and O−D stretching and the H−O−D bending modes, each with distinct transition frequencies. In H_2O, on the other hand, the antisymmetric and symmetric O−H stretching modes have similar transition frequencies, whereas the O−H bending fundamental frequency is about half of the stretching frequencies. In the case of HOD in H_2O or D_2O a significant frequency mismatch of $500\,\mathrm{cm}^{-1}$ exists between the $v(\nu_{OH}) = 1$ and $v(\delta_{HOD}) = 2$ levels [184, 201, 202]. Here the O−H stretching vibration may dissipate the excitation energy through the bending pathway, but the involvement of the hydrogen bond modes (librations, hydrogen bond stretching modes with the H_2O or D_2O solvent bath) should play an active acceptor role in the primary step in energy redistribution as well. In contrast, for neat liquid H_2O the energy mismatch between the $v(\nu_{OH}) = 1$ and $v(\delta_{HOD}) = 2$ levels is minor, and within the spectral width of the O−H stretching vibration a clear overlap exists. Energy redistribution through the bending pathway is - thus - much more facilitated by the vibrational mode structure of the hydrogen-bonded H_2O molecule, although here also the excess energy has eventually to be channeled into the hydrogen bond network vibrational modes.

The bending vibration of any isotopomer of water (HOD, H_2O, D_2O) is the intramolecular degree of freedom with the lowest fundamental frequency. As a result, population relaxation of the bending mode can only proceed by dissipation into the intermolecular modes of the hydrogen bond network, making the bending vibration an ideal means for studies of energy transport through the hydrogen bond network triggered by initial local vibrational excitation.

Measurements of the O−H stretching population relaxation for isolated non-hydrogen-bonded H_2O molecules dissolved in $CDCl_3$ have resulted in a T_1 time of 36 ps for the asymmetric O−H stretching vibration [203, 204]. Isolated HOD molecules dissolved in acetonitrile have an O−H stretching lifetime value of $T_1 = 12\,\mathrm{ps}$, whereas an increased HOD fraction leads to a gradual decrease of this value approaching that of HOD in D_2O ($T_1 = 0.7\,\mathrm{ps}$) [205].

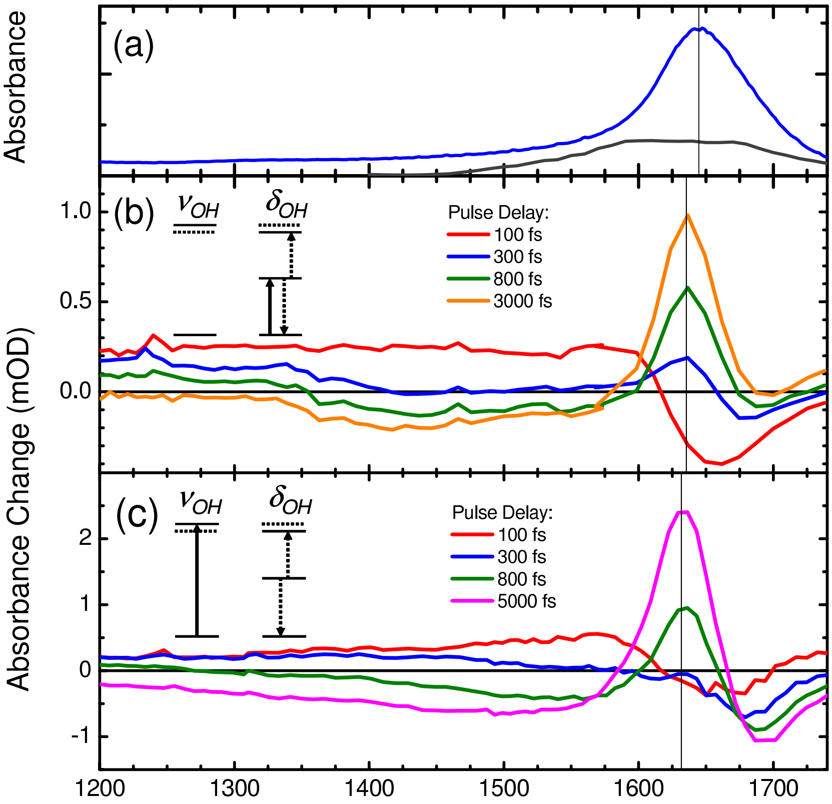

Fig. 7.11. (a) Linear vibrational absorption spectrum of pure H_2O, showing the O−H bending band and a broad librational absorption (*blue line*) as well as the spectral bandwidth of the IR pump pulse (*gray curve*); (b) Transient infrared spectra of H_2O measured with pump pulses centered at 1650 cm^{-1}, showing the $v(\delta_{OH}) = 0 \rightarrow 1$ bleaching and an extremely broad $v(\delta_{OH}) = 1 \rightarrow 2$ excited state absorption. After population relaxation of the bending vibration one finds a frequency red-shifted $v(\delta_{OH}) = 0' \rightarrow 1'$ absorption of the hot bending ground state, as well as a red-shifted librational band; (c) Transient infrared spectra of H_2O in the bending and librational frequency region measured with pump pulses centered at 3150 cm^{-1}, pumping the O−H stretching band.

This decrease with increasing water fraction is accompanied by a frequency down-shift of the O−H stretching band. Here it has been argued that the frequency red-shift of the O−H band upon hydrogen bonding results into a more efficient Fermi coupling with the bending overtone, with a shorter O−H stretching T_1 population lifetime as a result. This argument has also been used to explain the decrease of the O−H stretching lifetime for liquid H_2O, measured to be 200 fs for neat water [26,100,206]. The bending overtone for the H_2O is located around 3250 cm^{-1}, whereas for HOD the mismatch of around $500\,\mathrm{cm}^{-1}$ between bending overtone and O−H stretching fundamental occurs. An increased red-shift of the O−H stretching band with more overlap with the O−H bending overtone is, however, not the only prerequisite for a faster O−H stretching population decay. Solvent fluctuations are necessary for enabling all members of the ensemble to sample with its O−H stretching oscillator the right resonance frequency space facilitating efficient energy redistribution [207], for instance, through Fermi coupling with the bending overtone.

Another example providing evidence that solvent fluctuations are playing a key role in the relaxation of the O−H stretching vibration are water molecules bound in solvation shells of ions. These exhibit longer O−H stretching population lifetimes (for an overview see Sect. 6.2 of [7]); for HOD up to 9 times longer than in bulk water [208], which cannot be explained by the frequency shifts of the O−H stretching bands only. Here it is known that water near ions has a lower mobility, as indicated by the decreased anisotropy decay of the O−H stretching oscillator of water in ion shells [209] and by recent molecular dynamics calculations [210]. A lifetime increase of O−H stretching vibrations of up to 0.8 ps has also been observed for H_2O molecules confined into micelle surroundings [211, 212]. Here the large number of ionic heads and counter ions lead to a lower water mobility (as exemplified by the inhomogeneity and anisotropy decay of the hydrogen stretching vibrations persisting well into the picosecond domain [116, 213]).

To test the validity of the O−H/O−D stretching to bending relaxation pathway mechanism, one has to consider population kinetics using the experimentally determined O−H/O−D bending lifetime as input. Single H_2O molecules dissolved in $CDCl_3$ have an O−H bending lifetime of 28.5 ps [214]. When water is hydrogen bonded to nearby solvent molecules, hydrogen bond stretching and librational modes enhance the bending relaxation rates significantly. When one quantum of O−H/O−D stretching modes is redistributed over such vibrational modes as O−H/O−D bending, librational and hydrogen bond stretching modes, making these highly excited, anharmonic couplings of these modes with the O−H/O−D stretching oscillator lead to transient frequency shifts [215]. The O−H/O−D stretching band appears frequency up-shifted when a molecule is in a "hot" ground state (see Sect. 7.3.1), clearly different from the $v(\nu_{OH}) = 1 \rightarrow 2$ excited state absorption that appears frequency down-shifted due to the diagonal anharmonicity. The O−H/O−D bending vibration exhibits the more typical transient frequency down-shifting for "hot" ground states (see Fig. 7.11) that are more difficult to distinguish from the vibrationally excited $v(\delta_{OH}) = 1$ states that also have red-shifted $v(\delta_{OH}) = 1 \rightarrow 2$ excited state absorption contributions [28, 31, 216, 217].

Only recently the population lifetime of the bending vibration of HOD in D_2O [217], of H_2O in D_2O [216], as well as of H_2O in neat water [28] have been measured with IR-pump/IR-probe spectroscopy. For HOD in D_2O a value of 390 fs was found [217], very close to recent theoretical estimations [218, 219]. For the determination of the bending vibration of H_2O it is important to measure with a time resolution as short as 100 fs. To eliminate unwanted cross phase modulation by cell window material that prevents analysis of the response at early pulse delays [216], a recent study on neat H_2O using thin Si_3N_4 windows with negligible nonresonant response, has led to a value of 170 fs for the population lifetime of the water bending vibration [28]. In this work also the important signal contributions of the nonlinear response of librational excitations in the frequency range between 1200 and 1700 cm^{-1} have been indicated (Fig. 7.11). A H_2O bending lifetime of 170 fs seems to be in contradiction with the previously reported value of 1.4 ps, found with IR-pump/anti-Stokes Raman probe measurements [220]. Measurements on the intramolecular (stretching, bending) modes of neat H_2O, however, are always intertwined with frequency shifts caused by anharmonic couplings to the intermolecular hydrogen bond network librational and hydrogen bond stretching modes, since the vibrational energy accepting molecules are of the same species as the initially excited H_2O molecule carrying one quantum of the O−H stretching or bending vibration. This may be the reason for the apparent discrepancy between the recent IR-pump/IR-probe and the IR-pump/anti-Stokes Raman probe measurements, where a larger effect on the measured signals is expected in the latter case due to a substantial fraction of excited molecules [221–223]. For H_2O a fully completed cooling cannot be observed until heat transport out of the laser beam interaction zone has finished that occurs well into the microsecond time regime. Only in the case of water confined in micelles vibrational excitation transfer to the micelle molecular units, and eventually to the organic phase lead to a full cooling of water back to room temperature with micelle size-dependent picosecond time scales [224–226].

In light of the 170 fs population relaxation time of the bending vibration of H_2O, and the 200 fs lifetime of the O−H stretching vibration in H_2O, one can estimate that the transient population of the bending $v(\delta_{HOH}) = 1$ state will not reach more than a maximum value of 0.35 compared to the hypothetical case where the bending vibration has an infinite lifetime, provided all excited molecules relax through the bending vibrational pathway. As a result, one has to be careful in concluding that a red-shifting of the bending vibration upon excitation of the O−H stretching is a direct indication of the transient population of the bending mode [205,212,223,227–229], as excitation of librational and hydrogen bond stretching modes [28], and even the O−H stretching vibration [31], also will play a role in the observed features. Figure 7.11c shows how upon O−H stretching excitation of H_2O, the O−H bending shows an instantaneous response, pointing to a Fermi resonance between the $v(\nu_{OH}) = 1$ and $v(\delta_{OH}) = 2$ states. As a result the $v(\delta_{OH}) = 2 \rightarrow 3$ and $v(\delta_{OH}) = 1 \rightarrow 2$ transitions of the bending oscillator are strongly broadened, extending over more than 200 cm^{-1}. A delayed increase in stimulated emission of the $v(\delta_{OH}) = 1 \rightarrow 0$ transition observed at 1650 cm^{-1}, before contributions of a “hot” bending ground state begin to dominate, is in perfect agreement with a sequential population transfer from the $v(\nu_{OH}) = 1/v(\delta_{OH}) = 2$ manifold to the $v(\delta_{OH}) = 1$ state (with partial vibrational energy release into librational degrees of freedom with a 200 fs time constant), followed by bending relaxation to the $v(\delta_{OH}) = 0$ ground state, again with energy dissipation to librational modes.

7.4.4 Chemical exchange

The basic idea of exchange spectroscopy, both in NMR and in the IR spectral range, is the following: A particular group in the molecule is tagged, (i.e. a nuclear spin in the NMR case and a local normal mode in the IR case) by excitation. As long as that excitation lives, and does not decay due to T_1 relaxation, the molecular group will carry it around. When the molecular group changes its spectroscopic properties due to chemical exchange, i.e. changes its chemical environment due to some diffusive process and as a result of that changes its absorption frequency, it will just take its tag (i.e. its excitation) with it.

The basic assumption of exchange spectroscopy is that the excitation of the molecular group does *not* influence the way how the molecules move in time; the excitation is just used as a label to follow how molecules move in time. They move not because of the excitation, but due to room temperature diffusive motion. This assumption certainly is valid in the case of NMR, where the excitation energy is far below $k_B T$ and hence, very unlikely to influence the course of a reaction just because of an energy argument. However, in the case of an IR excitation, this assumption might sometimes be questionable. Energy, in principle, would be sufficient to change the outcome of a diffusive process, but what helps is the fact that vibrational transitions, which are harmonic oscillators to a very good approximation, tend to decouple from each other. However, in the case of strongly coupled states, such as in hydrogen-bonded systems, this assumption might break down [230].

2D spectroscopy is ideally suited to study ultrafast chemical exchange processes. This was first demonstrated by Woutersen and Hamm, studying the exchange between hydrogen bonded and non-hydrogen bonded N-methylacetamide (NMA) dissolved in methanol [231]. More recently and almost in parallel, chemical exchange was also studied by Hochstrasser and co-workers for hydrogen-bond exchange between CH_3OH linked to the cyanosite of CH_3CN [121], as well as by Fayer and co-workers [157,158] for exchange between hydrogen-bonded phenol-benzene complexes as well as for rotational isomerization in ethane derivatives [232]. When phenol-*d* and benzene are mixed together in CCl_4, both exist in an equilibrium between a complexed and a dissociated form (Fig. 7.12a), forming a weak hydrogen bond between the OD group of phenol and the benzene ring. Upon hydrogen bonding, the O−D stretch mode changes its frequency from about $2670\,\mathrm{cm}^{-1}$ to $2530\,\mathrm{cm}^{-1}$. Hence, in the linear absorption spectrum, two peaks appear which represent the equilibrium ratio between both configurations (which can be tuned by adjusting the benzene concentration). However, the linear spectrum gives no

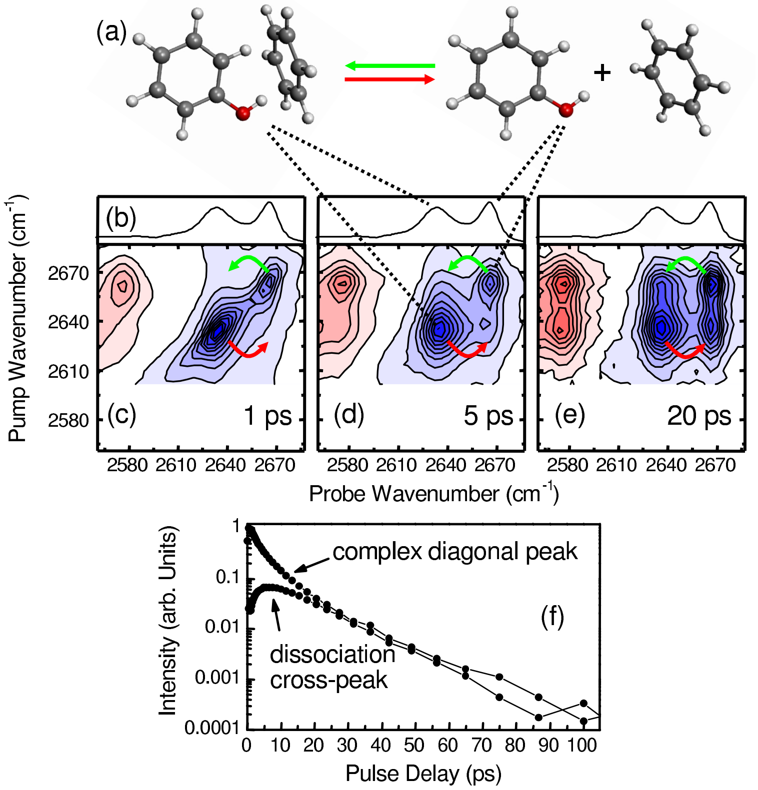

Fig. 7.12. (a) Chemical exchange between uncomplexed phenol and phenol hydrogen-bonded to benzene; (b) linear IR spectrum; (c-e) 2D-IR measurements using the double resonance approach measured at three different pulse delays show the onset of exchange between the two conformations; (f) the magnitude of the diagonal and off-diagonal peaks as function of pulse delay show that full equilibration occurs within 20 ps.

clue about the exchange rate between both configurations, except that it is slower than some threshold value, in which case both bands would start to merge due to motional narrowing effects.

The 2D spectrum, in contrast, provides exactly this information. The essential parameter varied in an exchange experiment is the so-called waiting or mixing time τ_m, i.e. the time between labeling and probing the O$-$D vibrator. Initially, after 1 ps, essentially no exchange had occurred. As a result, the 2D spectrum is still diagonal, saying that each labeled molecule, complexed or dissociated, is still in the configuration in which it was when exciting it. As times go on, however, labeled O$-$D vibrators change from complexed to dissociated form and vice versa, carrying their tag with them. As a result, cross peaks appear in the 2D spectrum which report on molecules which were in one configuration when pumping it, but jumped to the other configuration during the waiting time before probing it.

The intensities of diagonal and cross peak directly report on the time scale of the exchange process (Fig. 7.12e). Initially, the cross peak intensity is zero, but as both configurations equilibrate, the intensities of diagonal and cross peak approach each other. In fact, the ratio between both intensities would directly reflect the equilibration time. Figure 7.12f also demonstrates a limitation of exchange spectroscopy: The exchange process can be observed only as long as the vibrational excitation, that is the tag, lives. As T_1 relaxation times are relatively short for vibrational transitions in the solution phase (typically 1-20 ps), the time window accessible to 2D-IR spectroscopy is relatively short. In that sense, 2D-IR and 2D-NMR exchange spectroscopy are complimentary, as they address completely different time regimes. Improving the signal-to-noise ratio of the 2D apparatus may increase the accessible time window. For example, in Fig. 7.12 the exchange process has been followed up to 100 ps although the T_1 relaxation time is ≈ 12 ps, but T_1 relaxation will eventually stop the possibility to observe the process. For hydrogen-bonded systems the vibrational cooling rates will delimit the observation time window, as these systems relax into spectrally shifted hot ground states (Fig. 7.6). If one were to remove the vibrationally excited molecules by, for example, a photochemical process in the vibrationally excited state so that they could not fall back into the initial state, one could follow chemical exchange for unlimited time for the hole burned into the ensemble.

It is worth noting that Fig. 7.12 and the data shown in [157] have been measured with the two complimentary techniques of 2D-IR spectroscopy discussed in Sect. 7.3.3, one in the frequency domain (Fig. 7.12) using the double resonance scheme, and one in the time domain [157] using the heterodyne detected photon echo scheme. Besides this, the conditions were exactly the same. The comparison shows that in principle the information content of both techniques is indeed exactly the same.

7.5 Hydrogen bonds with ordered molecular topologies

Inter- as well as intramolecular hydrogen bonds with well-defined geometries appear in a number of different classes of compounds including numerous ordinary organic molecules, carbohydrates, carboxylic acids, amino acids, nucleosides and nucleotides as well as biomolecular macromolecules such as proteins or nucleic acid structures [48]. Hydrogen bonding crucially determines the molecular structure and thus, the functionality in these systems. In this Section two examples of medium-strong hydrogen bonds with well-defined geometries are presented. Several ultrafast nonlinear spectroscopic techniques are employed to discern the different hydrogen bond vibrational coupling mechanisms.

7.5.1 Coherent nuclear motions and relaxation processes in intramolecular hydrogen bonds

The anharmonic coupling of the X−H stretching oscillator to low-frequency hydrogen bond modes results in a vibrational multilevel system and progressions of vibrational transitions within the X−H stretching absorption band. Broadband excitation of such a system by a femtosecond pulse generates a nonstationary superposition of vibrational levels of the low-frequency mode, i.e. a vibrational wave packet that propagates in the potential defined by the high frequency X−H stretching vibrations (see Fig. 7.2). Oscillatory wave packet motions have been observed for different molecular systems forming a medium-strong intramolecular hydrogen bond of well-defined geometry. As a prototype example, results are presented here of a detailed pump-probe study of *o*-phthalic acid monomethylester (PMME-H) and its deuterated analog (PMME-D) (Fig. 7.13).

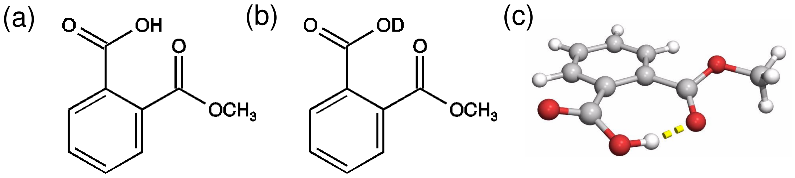

Fig. 7.13. *o*-Phthalic acid monomethylester (PMME); (a) PMME-H; (b) PMME-D; (c) lowest energy conformer.

The structure and the vibrational spectra of PMME were analyzed by quantum chemical calculations which are discussed in [13]. The lowest energy conformer of PMME consists in a quasi-planar structure in which the hydrogen bond is part of a seven-membered ring. This 7-ring does not entirely fit into the plane of the benzene ring so that the substituents are slightly tilted out-of-plane (Fig. 7.13c). The heavy atom hydrogen bond O· · · O distance of 256 pm and the H· · · O distance of 160 pm indicate an intramolecular hydrogen bond of intermediate strength and a well-defined geometry.

The steady-state O−H and O−D stretching bands of PMME-H and PMME-D are shown in Fig. 7.14a. In the femtosecond pump-probe experiments with PMME-H, the infrared pulses were tuned throughout the O−H stretching band, as indicated by the pulse spectra in Fig. 7.14b, and the spectrally integrated probe pulses transmitted through the sample were detected. The time evolution of the nonlinear change of absorbance at the different spectral positions is plotted in Fig. 7.15. Apart from small solvent and sample cell window contributions around delay zero, the signal originates from changes of the O−H stretching absorption of PMME-H. For probe frequencies between 2500 and 3200 cm^{-1}, a pronounced decrease of infrared absorption is observed that is strongest around the maximum of the steady-state infrared band. The

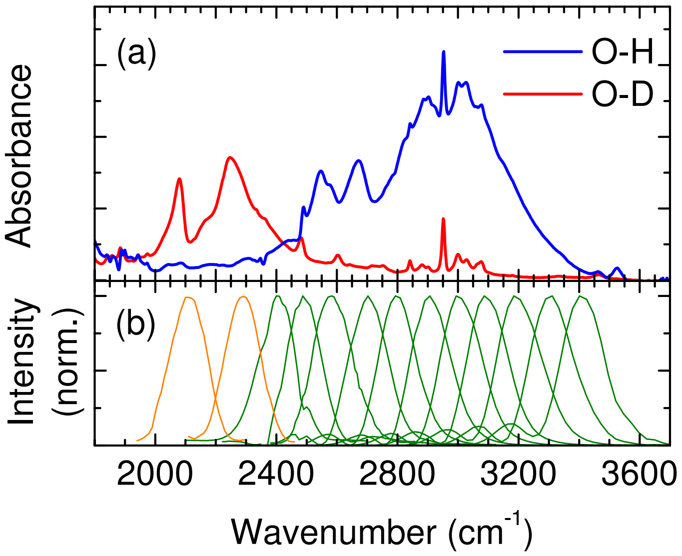

Fig. 7.14. (a) Steady-state O−H stretching band of PMME-H (*blue line*) and O−D stretching band of PMME-D (*red line*). The sharp line at 2950 cm^{-1} is due to C−H stretching absorption; (b) Spectra of the femtosecond pulses used in the pump-probe experiments with spectrally integrated detection (*green lines*) and with spectrally resolved detection (*orange lines*).

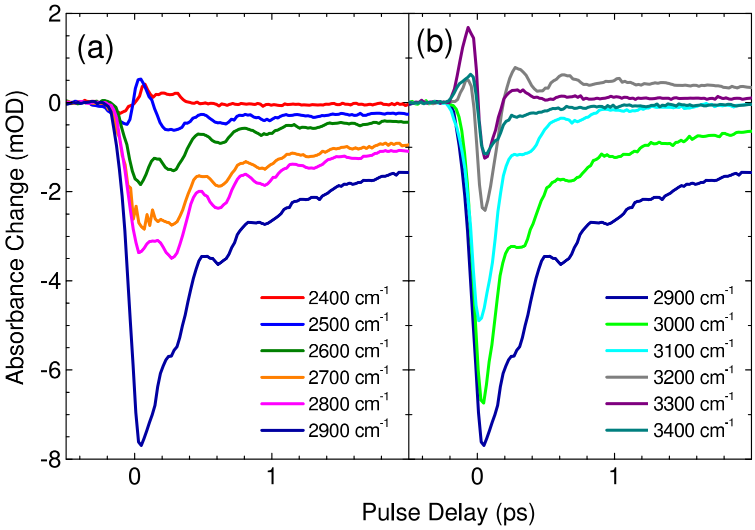

Fig. 7.15. PMME-H: Pump-probe transients measured using spectrally integrated detection. The absorbance change is plotted as function of delay between pump and probe pulses at the frequencies indicated.

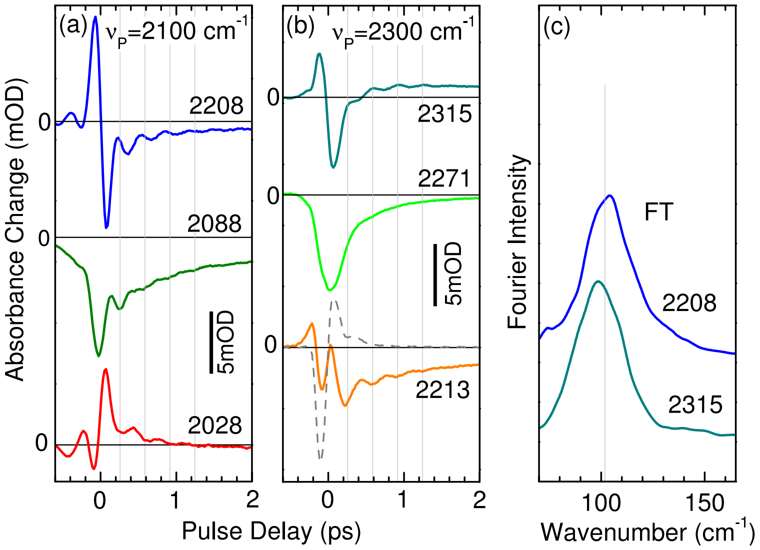

Fig. 7.16. PMME-D: (a,b) Time-resolved absorbance changes measured using spectrally resolved detection (ν_p: center frequency of the pump pulses, probe frequencies are given in cm^{-1}). The *dashed line* in (b) represents the response of the solvent; (c) Fourier transforms (FT) of the oscillatory signals.

absorption changes show a fast decay within the first 1 ps, followed by a slower relaxation on a time scale of 30 ps (not shown). At 3300 and 3400 cm^{-1}, an absorption increase is found which rises within the first 200-300 fs and shows a slow decay within 30 ps. All transients are superimposed by strong oscillatory signals with a frequency of 100 cm^{-1} and a damping time of approximately 500 fs.

The transient O−D stretching absorption of PMME-D reveals a similar behavior. In Fig. 7.16, results are presented for pump pulses centered at 2100 cm^{-1} (a) and 2300 cm^{-1} (b) and spectrally dispersed probe pulses. Depending on the probe frequency, one observes either bleaching or enhanced absorption. At 2028 cm^{-1} (Fig. 7.16a), the enhanced absorption decays with a time constant of about 400 fs. The bleaching transients (except for a probe frequency of 2271 cm^{-1}) show a fast decay with 400 fs, followed by a slower decay on a 20 to 30 ps time scale (not shown). Again, pronounced oscillations with a frequency of 100 cm^{-1}(Fig. 7.16c), i.e. identical to that in PMME-H, are superimposed on the incoherent pump-probe signals.

For an analysis of the pump-probe data, the level scheme in Fig. 7.6 has been applied (A refined level scheme including the potential curves for the low-frequency hydrogen bond motion will be presented in the following Subsection). In addition to the vibrational transition from the $v(\nu_{OH}) = 0$ to the $v(\nu_{OH}) = 1$ state, the red-shifted $v(\nu_{OH}) = 1$ to $v(\nu_{OH}) = 2$ transition and the blue-shifted $v(\nu_{OH}) = 0'$ to $v(\nu_{OH}) = 1'$ transition of molecules with a vibrationally hot ground state are taken into account. The pump pulse promotes part of the molecules from the $v(\nu_{OH}) = 0$ to the $v(\nu_{OH}) = 1$ state, resulting in a bleaching of the $v(\nu_{OH}) = 0 \rightarrow 1$ transition due to the depletion of the $v(\nu_{OH}) = 0$ state and stimulated emission from the $v(\nu_{OH}) = 1$ state. Such two contributions dominate the bleaching signals observed at delay times $< 1\,\mathrm{ps}$ in Figs. 7.14 and 7.15. The transient population of the $v(\nu_{OH}) = 1$ state gives also rise to a red-shifted $v(\nu_{OH}) = 1 \rightarrow 2$ absorption which is evident from the PMME-D transient at $2028\,\mathrm{cm}^{-1}$ (Fig. 7.16a) and – much less pronounced – from the PMME-H data taken at $2400\,\mathrm{cm}^{-1}$ (Fig. 7.15). The decay of excited state absorption reflects the depopulation of the $v(\nu_{OH}) = 1$ level with time constants of $\sim$400 fs for PMME-D and $< 250\,\mathrm{fs}$ for PMME-H. Population relaxation is due to a coupling of the $v(\nu_{OH}) = 1$ state to other vibrational modes at lower frequency, transferring the energy of the O−H (O−D) excitation into the vibrational manifold (the details of which will be discussed in the following Subsection). As a result, molecules with a hot vibrational system are created in which the O−H (O−D) stretching mode is in the $v(\nu_{XH}) = 0'$ ground state. In the hot molecules, the H-bond is weakened and, thus, the O−H (O−D) stretching absorption is blue-shifted compared to the initial absorption. This mechanism gives rise to (i) the enhanced absorption of PMME-H at 3300 and $3400\,\mathrm{cm}^{-1}$ and of PMME-D at $2315\,\mathrm{cm}^{-1}$, and (ii) to the bleaching signals extending to delay times longer than 1 ps. Dissipation of the vibrational excess energy into the surrounding solvent – a process occurring on a multitude of time scales extending up to several tens of picoseconds – leads to the slow nonexponential decay of the absorption changes. It should be noted that the fast rise of the blue-shifted absorption of PMME-H at $3400\,\mathrm{cm}^{-1}$ gives independent support for a decay of the $v(\nu_{OH}) = 1$ state with a sub-250 fs time constant.

The oscillatory signals present in the pump-probe transients are discussed next. In both PMME-H and PMME-D, the oscillations display a frequency of $100\,\mathrm{cm}^{-1}$. The oscillations are due to wave packet motions along a low-frequency mode which couples anharmonically to the fast stretching modes. Wave packet generation is visualized with the help of the potential energy scheme in Fig. 7.2a which is based on an adiabatic separation of the time scales of the fast stretching and the slow low-frequency motion. In the experiments, the spectral field envelope of the pump pulse covers several levels of the low-frequency mode, allowing for the excitation of a coherent superposition of low-frequency states, i.e. of wave packets. Wave packets in the $v(\nu_{OH}) = 1$ state of the stretching oscillator are created via vibrational absorption whereas wave packet motion in the $v(\nu_{OH}) = 0$ state is induced by a Raman-like process within the bandwidth of the pump pulse. This Raman process is resonantly enhanced by the vibrational transition.

The enhanced absorption of PMME-D at $2028\,\mathrm{cm}^{-1}$ (Fig. 7.16a) is due to the $v(\nu_{OH}) = 1 \rightarrow 2$ transition and – thus – the oscillations on this transient reflect wave packet motion in the $v(\nu_{OH}) = 1$ state. The damping time of the oscillations of 500 fs is close to the $v(\nu_{OH}) = 1$ lifetime, suggesting that vibrational population relaxation represents a major damping mechanism. In PMME-H, the $v(\nu_{OH}) = 1$ lifetime of the O−H stretching mode has a substantially smaller value of 200 to 250 fs, i.e. close to the oscillation period of the 100 cm^{-1} mode. As a result, oscillations in the $v(\nu_{OH}) = 1$ state are not observed.

Wave packet motions in both the $v(\nu_{OH}) = 0$ and $v(\nu_{OH}) = 1$ states are relevant for the analysis of the oscillations found on top of the bleaching signals. As shown schematically in Fig. 7.2a, the $v(\nu_{OH}) = 0 \rightarrow 1$ transition frequency of the O−D/O−H stretching mode depends on the elongation along the low-frequency mode. Wave packet motion along this coordinate results in a periodic modulation of the O−D/O−H transition frequency. In PMME-D (Fig. 7.16), this mechanism leads to the oscillatory blue-shift of the O−D stretching band which is evident from the oscillatory enhancement of absorption at 2315 cm^{-1}. Consistent with this picture, there are no oscillations around the maximum of the O−D band at 2271 cm^{-1} and oscillations of opposite phase at 2213 cm^{-1}. PMME-H (Fig. 7.15) shows the same behavior. Here, however, only wave packet motion in the $v(\nu_{OH}) = 0$ state is relevant [13]. As frequency shifts of the O−D/O−H stretching bands are a measure of the length of the hydrogen bond, the oscillatory blue-shift is equivalent to a modulation of the O$\cdots$O distance in PMME, determining the strength of the hydrogen bond.

A normal mode analysis of PMME provides insight into the microscopic nature of the low-frequency mode displaying a frequency of 100 cm^{-1}. As discussed in detail in [8, 13], the periodic modulation of the O$\cdots$O distance is attributed to an out-of plane torsional motion by which the two ring substituents in PMME move relative to each other, thus changing the O$\cdots$O distance. This picture has been confirmed by anharmonic potential energy surface calculations and quantum dynamics simulations [14–17]. The frequency of this mode remains unchanged upon H/D exchange and − thus − identical oscillation frequencies occur in the PMME-H and PMME-D data. This intramolecular mode displays a comparably long damping time on the order of 0.5 ps, resulting in an underdamped character of this mode. Note, that the population relaxation time of the low-frequency mode in the $v(\nu_{OH}) = 0$ ground state is about 1.7 ps as obtained from classical molecular dynamics simulations of the force-force correlation function [18]. This hints at a more complex damping mechanism including, e.g., intramolecular anharmonic couplings. This is in contrast to many theoretical studies of H-bond dynamics in which overdamped low-frequency motions have been assumed [39, 44, 233]. It should be noted that there are modes at higher frequencies also modulating the length of the hydrogen bond [14]. The spectral bandwidth of the generated pump pulses and the time resolution of the experiment, however, were not sufficient to excite wave packets along such modes and to follow their time evolution.

7.5.2 Intramolecular vibrational redistribution of the O−H stretching excitation

In the case of PMME-H the fate of the O−H stretching excitation after T_1 relaxation has also been investigated. Two-color pump-probe spectroscopy on the O−H stretching, C=O stretching and O−H in-plane bending vibrations of PMME-H, have demonstrated that excitation energy of the O−H stretching oscillator is redistributed on a subpicosecond time scale along the O−H bending vibration (Fig. 7.17) [25].

Here the dynamics of the O−H bending vibration is measured, by following the decay of the O−H bending bleach at 1415 cm^{-1}, and the excited state absorption at 1390 cm^{-1}, as observed for three different pumping frequencies: excitation of the O−H stretching vibration at 2900 cm^{-1} (Fig. 7.17a,b), excitation of the C=O stretching vibration at 1740 cm^{-1} (Fig. 7.17e,f), and excitation of the bend vibration itself at 1400 cm^{-1} (Fig. 7.17c,d). In all cases a red-shifted feature appears within temporal resolution, albeit with significant differences in shape. Red-shifted vibrational resonances are expected both for excitation of the O−H bending mode (when $v(\delta_{OH}) = 1$), and for cases when other - in particular low-frequency - modes are excited. Assignment of the spectral contributions due to these clearly distinct situations is not trivial in itself, but it is the dynamics of these different states that enable a clear interpretation. Whereas excitation of the O−H stretching and O−H bending leads to similar behavior of the transient absorbance in the bend region, with both 800 fs and 7 ps temporal components, excitation of the C=O stretching vibration only results in the 7 ps component in the response of the O−H bending vibration. From these results it can be concluded that with an O−H stretching lifetime of 220 fs and an O−H bending lifetime of 800 fs it is experimentally feasible to detect a transient population build-up of the bending vibration after O−H stretching excitation.

In order to get a better idea of the multidimensional aspects of IVR in PMME quantum dynamical model calculations of the energy flow have been performed. A full-dimensional description of the intramolecular dynamics driven by an IR laser field has been given in [14] by combining a reaction surface Hamiltonian with a time-dependent self-consistent field propagation of nuclear wave packets. In agreement with experiment (cf. Figs. 7.15 and 7.16) this parameter-free simulation revealed the periodic modulation of the transient absorption signal due to the anharmonic coupling between the excited O−H stretching vibration and a low-frequency hydrogen bond mode. Despite its high-dimensional nature the model did not show any signatures of intramolecular energy randomization during the first 3 ps. Subsequently, in [16, 17] reduced 9- to 19-dimensional reaction surface models have been investigated on the basis of a multiconfiguration time-dependent Hartree approach [234]. Here, it could be demonstrated that the additional flexibility of the multiconfiguration wave function can capture the onset of IVR with an estimated time constant of about 20 ps [17]. However, this is still in strong

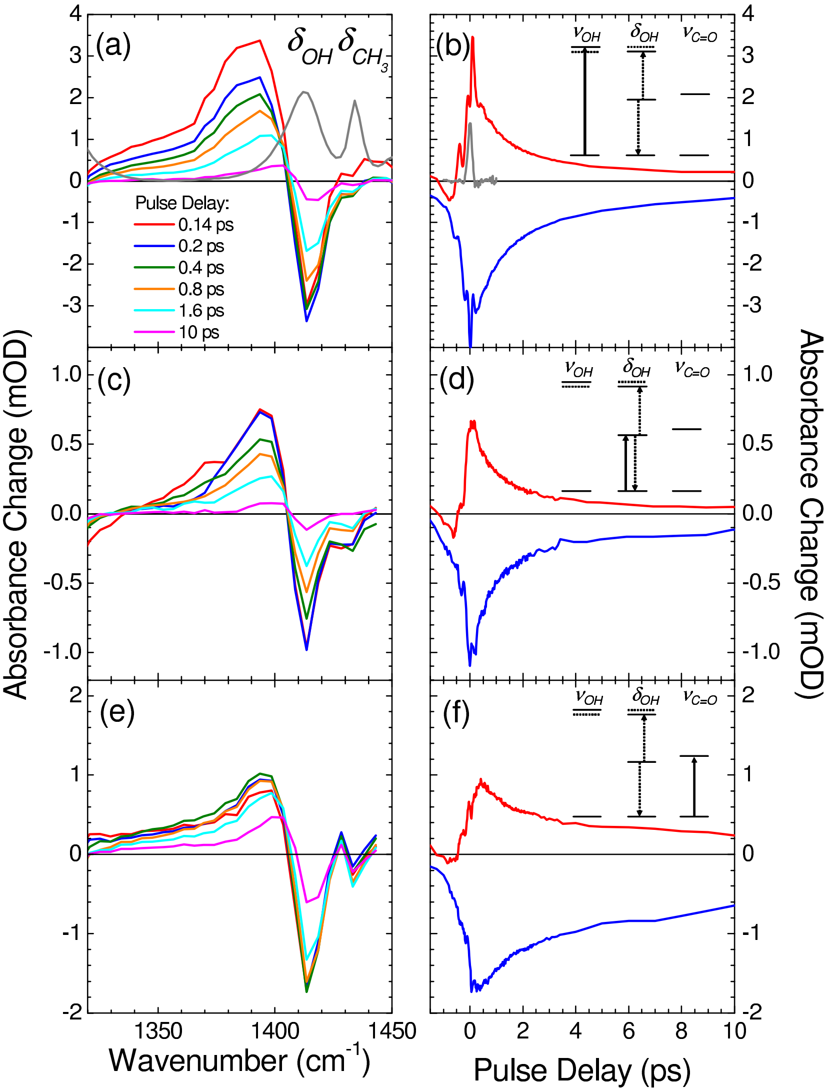

Fig. 7.17. PMME-H: Two color pump-probe results. The *gray curve* in (a) represents the steady-state IR absorption spectrum showing the O−H bending (at 1415 cm^{-1}) and the C−H bending of the CH$_3$-group (1435 cm^{-1}). The *gray curve* in (b) indicates the temporal resolution in the experiments. Here the bending vibration is probed for three excitation conditions: excitation of the O−H stretching vibration at 2900 cm^{-1} (a,b), the bending vibration at 1400 cm^{-1} (c,d) and the C=O stretching vibration at 1700 cm^{-1} (e,f). The frequency-resolved transient spectra are shown in panels (a,c,e) whereas the transient absorbance changes of the $v(\delta_{OH}) = 0 \to 1$ ground state bleach at 1415 cm^{-1} (negative signals) and the $v(\delta_{OH}) = 1 \to 2$ excited state absorption at 1390 cm^{-1} (positive signals) are shown in panels (b,d,f).

contrast to the observed time scale of about 200 and 400 fs for the O−H and O−D stretching vibrational relaxation, respectively, what led to the conclusion that the solvent interaction contributes considerably to these rapid relaxation processes.

The mechanistic details have been simulated by a dissipative system-bath model [235] specified to the case where the bath consists of intramolecular as well as solvent degrees of freedom. Because of its simpler absorption spectrum in the O−D stretching region, PMME-D was the first target for a system-bath description. In [15] a 3-dimensional model system was proposed which included the O−D stretching (ν_{OD}) and bending (δ_{OD}) coordinates as well as a low-frequency hydrogen bond mode (ν_{HB}). Due to its single minimum character the anharmonic potential energy surface could be spanned by the respective normal mode coordinates. Instead of the Taylor expansion in (7.5), the potential was calculated on a grid using DFT/B3LYP. The double peak structure of the IR spectrum in Fig. 7.14a could be explained as being due to a Fermi resonance between the $v(\nu_{OD}) = 0 \rightarrow 1$ fundamental and the $v(\delta_{OD}) = 0 \rightarrow 2$ overtone transition. The combination transitions with the low-frequency mode, e.g. $v(\nu_{OD}) + nv(\nu_{HB})$, are masked by the broadening due to the system-bath coupling. In the model of [15] the latter comprised linear and nonlinear terms responsible for energy and phase relaxation. A key feature of the model which proved to be vital for the explanation of the rapid $v(\nu_{OD}) = 1$ decay has been a solvent-assisted intramolecular relaxation pathway. Using classical molecular dynamics simulation of force-force correlation functions the relaxation time for the low-frequency hydrogen bond mode was determined to be about 1.7 ps in CCl_4 at room temperature [18]. In [18] it was also shown that the dissipative model supports coherence transfer with respect to the hydrogen bond mode between the ν_{OD} fundamental excitation and its ground state. This contributes to hydrogen bond wave packet dynamics in the ν_{OD} ground state which is additionally triggered by the initial IR-laser excitation (as has been discussed in Sect. 7.5.1).

The two-color IR pump-probe experiments of Fig. 7.17 described above provided a more detailed picture of the rapid IVR process in PMME-H [25]. Building on [18] a five-dimensional dissipative model has been derived whose relevant coordinates are shown in Fig. 7.18 in terms of their normal mode displacement vectors. Besides the O−H stretching (ν_{OH}) and bending (δ_{OH}) modes calculation of the anharmonic force constants suggests to include two modes of approximately out-of-plane O−H-bending character (γ_{OH1} and γ_{OH2}) into the model. These four fast coordinates are dressed by the slow coordinate of the hydrogen bond motion (ν_{HB}). It is instructive to inspect the diabatic potential energy curves for the motion of the hydrogen bond coordinate in the different states of the fast coordinates (see Fig. 7.18). Starting from the ground state there are certain "bands" of transitions such as the γ_{OH1} and γ_{OH2} fundamentals, the δ_{OH} fundamental as well as the γ_{OH1} and γ_{OH2} combination and first overtones, their second overtones as well as combinations with the δ_{OH} fundamental, and finally the ν_{OH} fundamental which

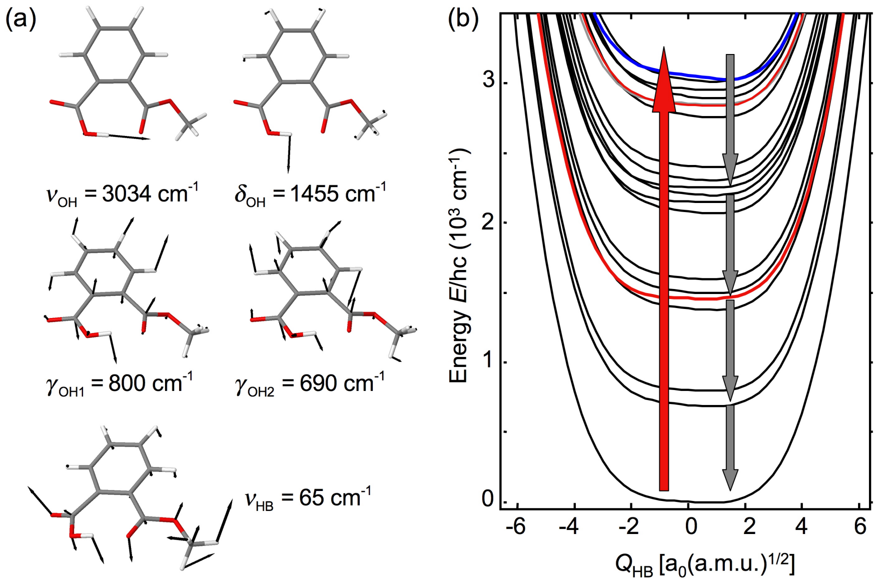

Fig. 7.18. (a) Normal mode displacement vectors of the 5 modes of the dissipative PMME-H model; (b) Uncoupled diabatic potential energy curves governing the motion of the low-frequency hydrogen bond mode for the different quantum states of the fast modes. These states as well as their coupling have been obtained by expressing the 5-dimensional Hamiltonian in the basis of the fast-coordinate states defined at the equilibrium geometry of the hydrogen bond mode (red - δ_{OH}, blue - ν_{OH}). The red arrow indicates the O−H stretching excitation by the IR laser field, whereas the gray arrows represent the energy cascading process.

is immersed into the manifold of states coming from the various combination transitions of the bending modes as well as the first δ_{OH} overtone. Notice that each potential curve in Fig. 7.18 contains the vibrational ladder of the low-frequency hydrogen bond mode and that there are diabatic state coupling between the different curves as well.

The quantum dynamics of this 5D dissipative model has been modeled using the Quantum Master equation approach [235]. From the density of states in the ν_{OH} region one would expect a rapid energy redistribution among several zero-order states upon excitation in this spectral range. However, simulations show that this is not sufficient to account for the 200 fs energy relaxation time scale. Modeling this relaxation requires to include other intramolecular as well a solvent degrees of freedom. Since the hydrogen bond mode has the lowest intramolecular frequency it can only relax into the solvent; the respective spectral density obtained from classical molecular dynamics has been discussed above [18]. As far as the modes γ_{OH1} and γ_{OH2} are concerned,

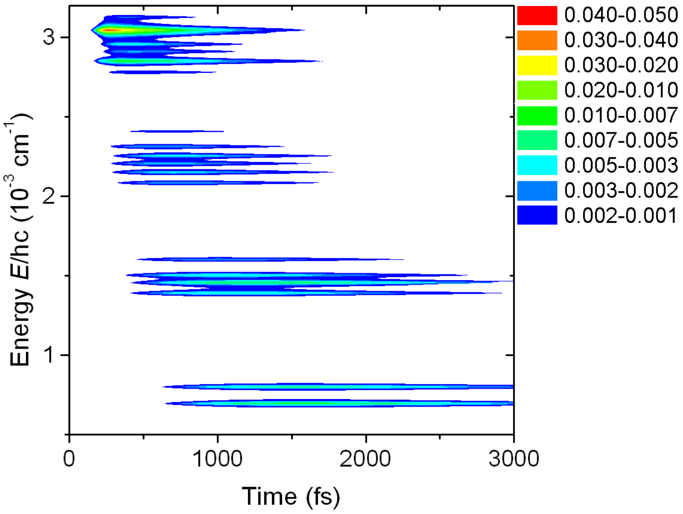

Fig. 7.19. Population dynamics of the diabatic states of PMME-H as indicated in Fig. 7.18 summed over all respective states of the hydrogen bond mode for the 5-dimensional dissipative model of PMME-H. Populations are shown at the energy of the corresponding diabatic states (ground state not shown).

there are different possibilities, such as the decay via modes of comparable frequency or via excitation of two quanta in a lower-frequency mode. According to the calculated anharmonic force constants the former model is to be favored. However, due to a slight energy mismatch, assistance of the transition by low-frequency solvent modes is required similar to what had been proposed for PMME-D in [15]. Notice that the strength of the solvent-assisted coupling to the intramolecular bath is the only free parameter of the model.

The resulting dynamics upon O−H stretching excitation with a 100 fs IR pulse is shown in Fig. 7.19 in terms of the diabatic state populations of the fast modes. The cascading of the energy down the vibrational ladder formed by the manifolds of different bending mode states is clearly discernible (see arrows in Fig. 7.18). The time scale of the ν_{OH} and δ_{OH} decay is about 200 fs and 800 fs, respectively, in good agreement with the experiment of Fig. 7.17, thus supporting the proposed cascading mechanism via the δ_{OH} bending vibration for the ultrafast ν_{OH} relaxation in intramolecular hydrogen bonds of this medium-strong type.

7.5.3 Coherent and relaxation dynamics of hydrogen-bonded dimers

Cyclic dimers of carboxylate acids represent important model systems forming two coupled intermolecular hydrogen bonds (Fig. 7.20). The linear vibrational

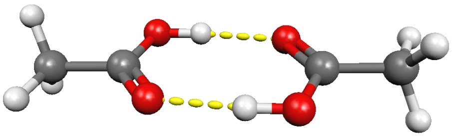

Fig. 7.20. Acetic acid dimer $(CX_3{-}COOX)_2$, X = H, D.

spectra of carboxylate acid dimers have been studied in detail, both in the gas and liquid solution phase, and a substantial theoretical effort has been undertaken to understand the line shape of their O−H and/or O−D stretching bands. In contrast, only few experiments have been reported on the nonlinear vibrational response. The coupling of the two carbonyl oscillators in acetic acid dimers has been investigated by femtosecond pump-probe and photon echo measurements [236], and vibrational relaxation following O−H stretching excitation has been addressed in picosecond pump-probe studies [237].

In the following, recent extensive pump-probe studies of cyclic acetic acid dimers in the femtosecond time domain are presented [20,21,24], followed by a discussion of results from photon echo measurements [22,27], and a presentation of quantum chemical calculations of the anharmonic couplings and the resulting linear spectra and nonlinear signals [24,27,29,30]. From the interplay of experiment and theory a quantitative estimation of the couplings as well as the linear and nonlinear infrared response is achieved. In order to disentangle the different coupling mechanisms (as described in Sect. 7.2.2) of the O−H/O−D stretching oscillator in acetic acid dimer, dimer structures containing two O−H$\cdots$O (OH/OH dimer) or two O−D$\cdots$O (OD/OD dimer) hydrogen bonds as well as dimers with one O−H$\cdots$O and one O−D$\cdots$O hydrogen bond (mixed dimers) have been explored. The combination of different nonlinear spectroscopic techniques enable the extraction of information on particular coupling mechanisms.

The steady state and the transient O−H stretching absorption spectra of OH/OH dimers are displayed in Fig. 7.21a,b. The transient spectra show a strong bleaching in the central part of the steady-state band and enhanced absorption on the red and blue wing, in accordance with the level scheme of Fig. 7.6. The bleach, consisting of a series of comparably narrow spectral dips, originates from the depopulation of the $v(\nu_{OH}) = 0$ state and stimulated emission from the $v(\nu_{OH}) = 1$ state. The enhanced absorption at small frequencies is due to the $v(\nu_{OH}) = 1 \rightarrow 2$ transition and decays by depopulation of the $v(\nu_{OH}) = 1$ state with a lifetime of $T_1 = 200\,\mathrm{fs}$. The latter is evident from time-resolved measurements at a probe frequency of $2250\,\mathrm{cm}^{-1}$ (not shown). The enhanced absorption on the blue side is caused by the vibrationally hot ground state formed by relaxation of the $v(\nu_{OH}) = 1$ state, followed by vibrational cooling on a 10 to 15 ps time scale. Transient spectra measured for the OD/OD and the mixed dimers – both on the O−H and O−D stretching bands – display a very similar behavior.

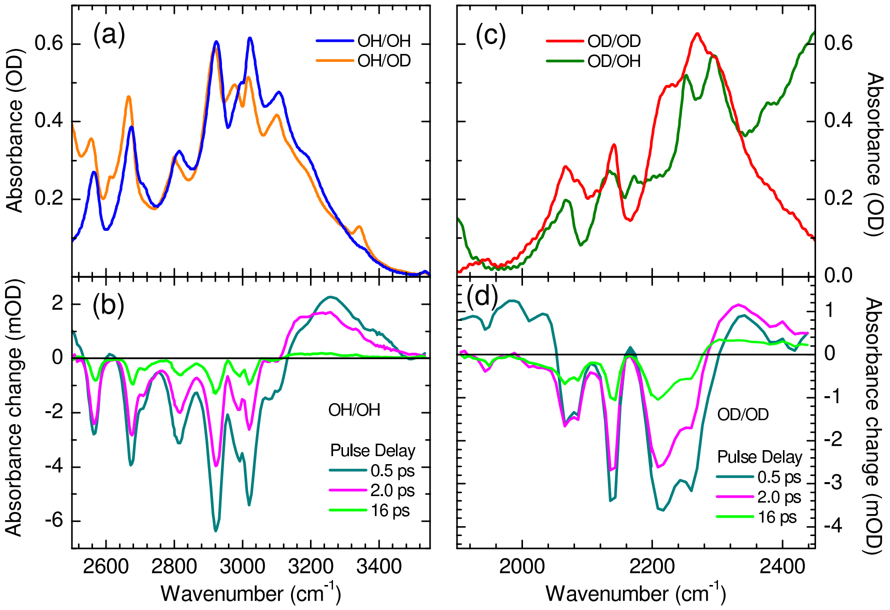

Fig. 7.21. (a) O$-$H stretching band of acetic acid dimer $(CD_3{-}COOH)_2$ (*blue line*: OH/OH-dimer) and of $(CD_3{-}COOH)$-$(CD_3{-}COOD)$ (*orange line*: OH/OD-mixed dimer); (b) Transient spectra of the OH/OH dimer measured at selected pulse delay between pump and probe; (c) O$-$D stretching band of acetic acid dimer $(CH_3{-}COOD)_2$ (*red line*: OD/OD-dimer) and of $(CH_3{-}COOD)$-$(CH_3{-}COOH)$ (*green line*: OD/OH-mixed dimer); (d) Transient spectra of the OD/OD dimer measured at selected pulse delay between pump and probe.

The time evolution of the nonlinear O$-$H stretching absorption (Fig. 7.22) shows pronounced oscillatory signals for all types of dimers studied. In contrast to the intramolecular hydrogen bond of PMME, and of other similar systems [8,9,13] the time-dependent amplitude of the oscillations displays features of a beatnote, demonstrating the presence of more than one oscillation frequency. In Fig. 7.23 the Fourier transforms of the oscillatory signals are plotted as obtained for the uniform isotopomers of acetic acid dimer. There are three prominent frequency components, a strong doublet with maxima at 145 and 170 cm^{-1} and a much weaker component around 50 cm^{-1}.

In principle the observed oscillatory components could originate from Davydov, Fermi or from coupling to low-frequency modes. The two local stretching oscillators in the OH/OH and OD/OD dimers are subject to Davydov coupling resulting in a splitting of the $v(\nu_{OH}) = 1$ states, on top of the anharmonic coupling to low-frequency modes. In the linear absorption spectrum of the ensemble of dimers, this results in two separate low-frequency progressions originating from the $v(Q_u) = 0$ and $v(Q_u) = 1$ levels in the $v(\nu_{OH}) = 0$ state of the O$-$H stretching vibrations (Fig. 7.24). In thermal

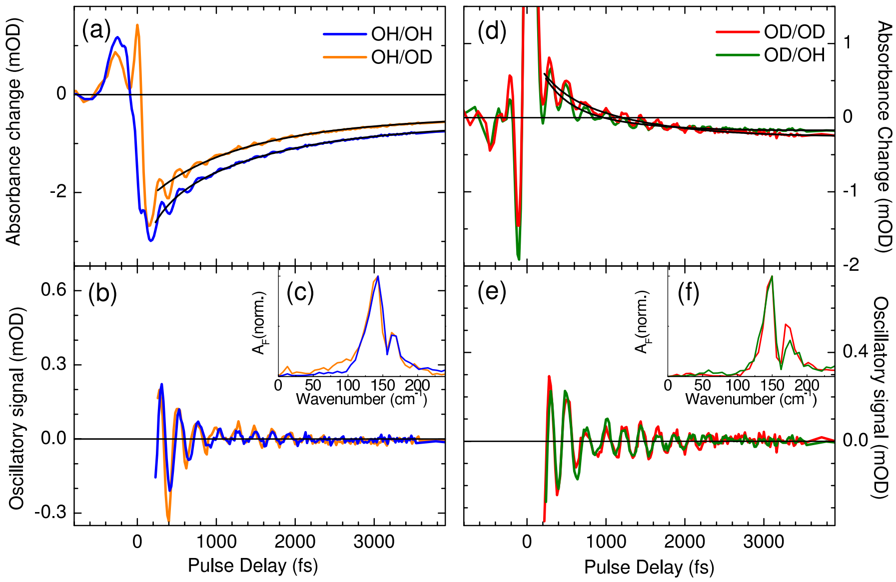

Fig. 7.22. (a) Transient absorbance changes in the bleach region of the O−H stretching band of acetic acid dimer $(CD_3{-}COOH)_2$ (*blue line*: OH/OH-dimer) and of $(CD_3{-}COOH)$-(CD_3COOD) (*orange line*: OH/OD-mixed dimer) as recorded with pump pulses centered at $2950\,cm^{-1}$ and a probe detection at $2880\,cm^{-1}$; (b) Oscillatory contribution of the pump-probe signals of the OH/OH and OH/OD dimers of panel (a); (c) Fourier transform of the oscillatory signals of (b) of the OH/OH and OH/OD dimers showing two low-frequency components; (d) Transient absorbance changes in the bleach region of the O−D stretching band of acetic acid dimer $(CH_3{-}COOD)_2$ (*red line*: OD/OD-dimer) and of $(CH_3{-}COOD)$-$(CH_3{-}COOH)$ (*green line*: OD/OH-mixed dimer) as recorded with pump pulses centered at $2100\,cm^{-1}$ and a probe detection at $2020\,cm^{-1}$; (e) Oscillatory contribution of the pump-probe signals of the OD/OD and OD/OH dimers of panel (d); (f) Fourier transform of the oscillatory signals of (e) of the OD/OD and OD/OH dimers showing two the same low-frequency components.

equilibrium, a particular dimer populates only one of the $v(Q_u)$ levels at a certain instant in time and – thus – only one of the progressions can be excited. Consequently, a quantum coherent nonstationary superposition of the split $v^{\pm}(\nu_{OH}) = 1$ states of the stretching mode cannot be excited in an individual dimer and quantum beats due to Davydov coupling are absent in the pump-probe signal.

This behavior is evident from a comparison of transients recorded with OH/OD and OH/OD dimers, the latter displaying negligible Davydov coupling because of the large frequency mismatch between the O−H and O−D stretching oscillators. The time-resolved change of O−D stretching absorption

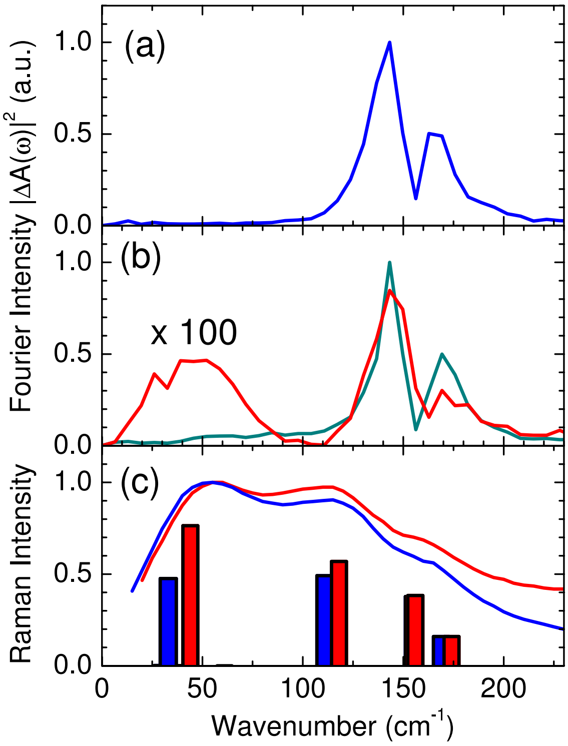

Fig. 7.23. Comparison of the Fourier intensities of the oscillatory components in the frequency-resolved pump-probe data of the acetic acid dimer isotopomers. (a) $(CD_3{-}COOH)_2$, measured at 3040 cm^{-1}; (b) $(CH_3{-}COOD)_2$, measured at 2300 cm^{-1} (*green line*) and 2250 cm^{-1} (*red line*); (c) experimental (*lines*) and calculated (*bars*) Raman spectra of $(CD_3{-}COOH)_2$ (*blue line/bars*) and of $(CH_3{-}COOD)_2$ (*red line/bars*).

of the two types of dimers shows a very similar time evolution, and the Fourier spectra agree within experimental accuracy.

Group theoretical analysis (Fig. 7.24c) and calculations of IR-active progressions originating from a ground state with the Q_u low-frequency mode being excited suggest small IR cross sections for this series [29].

A contribution of quantum beats between states split by Fermi resonances can be ruled out as well. There are different Fermi resonances within the O−H and O−D stretching bands. Depending on the spectral positions of pump and probe, this should lead to a variation of the oscillation frequencies, in particular when comparing O−H and O−D stretching excitations. Such a behavior is absent in the experiment, which shows identical oscillation frequencies for O−H and O−D stretching excitation that remain unchanged for pumping throughout the respective absorption band.

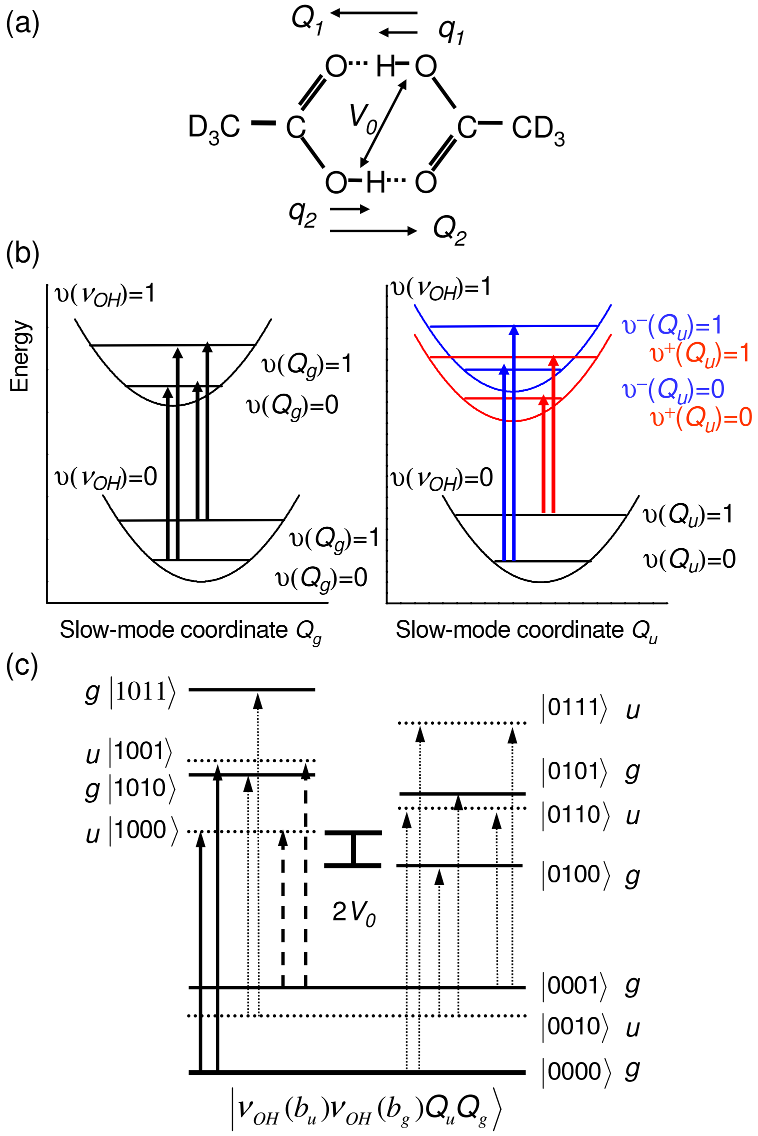

Fig. 7.24. (a) Schematic showing acetic acid dimer with local high-frequency (q_1, q_2) O–H stretching and low-frequency (Q_1, Q_2) O$\cdots$O hydrogen bond modes; (b) Potential energy surfaces of the low-frequency modes anharmonically coupled to the O–H stretching vibrations, shown using symmetrized Q_g and Q_u low-frequency modes. Davydov coupling (V_0) leads to a splitting of the energy levels of the asymmetric Q_u mode, for which a priori selection rules apply. (c) A refined analysis of the IR cross sections for the different transitions within the O–H stretching manifold (*solid lines*: strong ground state absorption; *dashed lines*: hot transitions; *dotted lines*: weak transitions; for details see [29]).

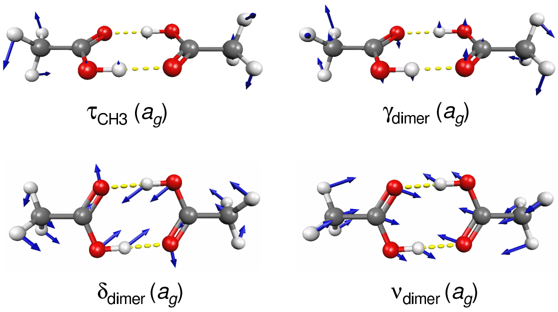
τ_{CH3} (a_g) γ_{dimer} (a_g)

δ_{dimer} (a_g) ν_{dimer} (a_g)

Fig. 7.25. Raman-active low-frequency vibrational modes of acetic acid dimer.

Instead, the oscillatory absorption changes are due to coherent wave packet motions along several low-frequency modes which anharmonically couple to the stretching modes. Wave packets in the $v(\nu_{OH/OD}) = 0$ states that are generated through an impulsive resonantly enhanced Raman process, govern the oscillatory response, whereas wave packets in the $v(\nu_{OH/OD}) = 1$ states are strongly damped by the fast depopulation process. Low-frequency modes of acetic acid have been studied in a number of Raman experiments. The spectrum in Fig. 7.23c was taken from [238] and displays three maxima around 50, 120 and 160 cm^{-1}. The number of subbands in such strongly broadened spectra and their assignment have remained controversial [239]. The character of the different low-frequency modes and their anharmonic coupling to the O−H stretching mode have now been analyzed in recent normal mode calculations based on density functional theory [24]. In Fig. 7.23c the calculated Raman transitions are shown for the OH/OH and OD/OD dimers.

There are four Raman-active vibrations (Fig. 7.25): the methyl torsion at 44 cm^{-1} (τ_{CH3}), the out-of-plane wagging mode at 118 cm^{-1} (γ_{dimer}), the in-plane bending mode around 155 cm^{-1} (δ_{dimer}) and the dimer stretching mode at 174 cm^{-1} (ν_{dimer}). In this set of vibrations, the in-plane bending and the dimer stretching modes couple strongly to the O−H/O-D stretching mode via a third-order term in the vibrational potential that dominates compared to higher order terms. The coupling of the methyl torsion is much weaker, and that of the out-of-plane wagging mode even negligible. Such theoretical results are in good agreement with the experimental findings: the strong doublet in the Fourier spectra (Fig. 7.23a,b) is assigned to the in-plane bending and the dimer stretching mode, the weak band around 50 cm^{-1} to the methyl torsion. The out-of-plane wagging is not observed at all. It should be noted that the spectra derived from the oscillatory pump-probe signals, i.e. from time domain data, allow for a much better separation of the low-frequency mode coupling than the steady-state spontaneous Raman spectra.

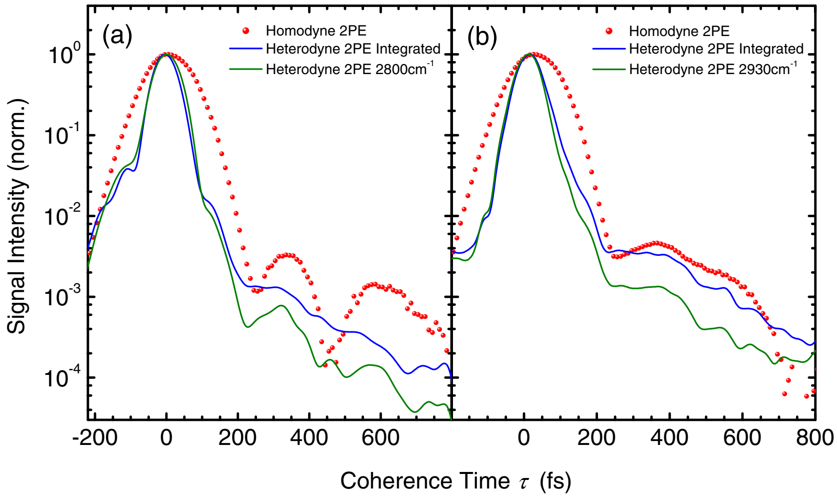

Fig. 7.26. Homodyne and heterodyne detected 2PE signals of acetic acid dimer $(CH_3{-}COOH)_2$ (a) and mixed dimers $(CD_3{-}COOH)$-$(CD_3{-}COOD)$ (b). The *red dotted trace* has been recorded using homodyne detection, whereas the *solid curves* have been derived from the heterodyne detected 2D-IR spectrum, for a particular detection frequency ν_3 and for spectral integration over ν_3.

In the case of photon echo spectroscopy on the acetic acid dimer, the number of coherences contributing to the nonlinear signals is large as a consequence of the multilevel structure of the O−H/O−D stretching band. Here in principle all coupling mechanisms described in Sect. 7.2.2 should affect the outcome of the echo experiments. Homodyne detected 2PE measurements (Fig. 7.26) have indicated the importance of the quantum beat contributions of the low-frequency mode couplings [22, 27], as indicated by the recurrences with an oscillation period given by the low-frequency in-plane stretching and in-plane deformation hydrogen bond modes. In addition Davydov coupling appears to be of minor importance. The low-frequency wave packet motions also lead to beating contributions in the integrated 3PEPS signals [22]. The homodyne detected photon echo measurements, in conjunction with a refined analysis of the fine structure of the bleach signals in the pump-probe measurements (Fig. 7.21) have led to the conclusion that the individual transitions in the O−H stretching manifold have a homogeneous broadening corresponding to a dephasing time $T_2 = 200\,\text{fs}$.

Two-color pump-probe experiments have indicated the importance of anharmonic couplings between the IR-active O−H stretching and O−H bending and C−O stretching modes [23]. The effects of these couplings between the O−H stretching and the fingerprint vibrations are even more pronounced in heterodyne-detected 2D infrared photon echo signals (Fig. 7.27). For the 2D spectrum with a population waiting time $T = 0\,\text{fs}$, transitions between

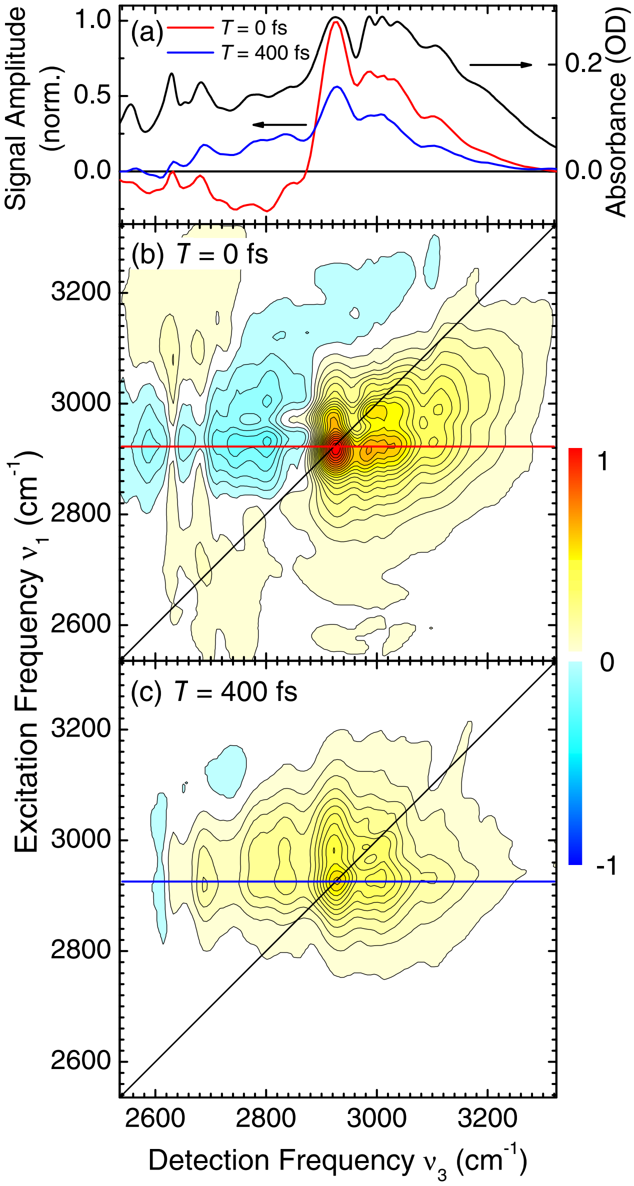

Fig. 7.27. (a) Linear spectrum of the O−H stretching band of cyclic dimers of acetic acid in CCl_4 (*black line*); Cross sections through the 2D-IR spectra for population times $T = 0\,\text{fs}$ (*red line*) and $T = 400\,\text{fs}$ (*blue line*); (b,c) 2D-IR spectra of acetic acid dimer for population times $T = 0$ and $400\,\text{fs}$. The amplitude of the photon echo signal is plotted as a function of the excitation frequency ν_1 and the detection frequency ν_3.

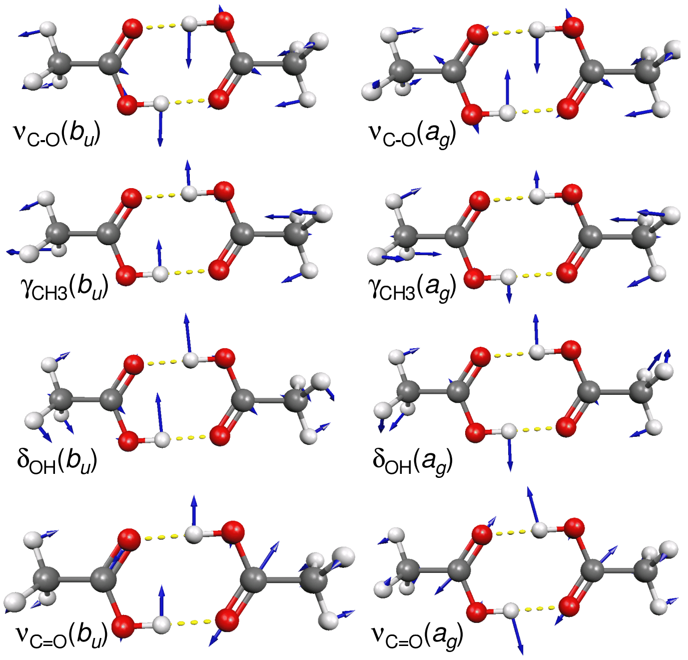

Fig. 7.28. Vibrational modes of acetic acid dimer $(CH_3{-}COOH)_2$, strongly coupled to the IR-active O−H stretching mode. IR- (b_u) and Raman-active (a_g) fingerprint modes.

$v(\nu_{OH}) = 0 \rightarrow 1$ and $v(\nu_{OH}) = 1 \rightarrow 2$ contribute with diagonal and off-diagonal peaks. Since the excited state of the O−H stretching vibration (lifetime $T_1 = 200\,\text{fs}$ [24]) decays into a hot ground state (Fig. 7.6) with complete loss of phase memory [22], the 2D spectrum for a population waiting time $T = 400\,\text{fs}$ is determined by the nonlinear signal contributions of the fundamental $v(\nu_{OH}) = 0 \rightarrow 1$ transition only, as described by the Liouville space pathway I of Fig. 7.4. In particular overtone and combination levels of the IR- and Raman-active O−H bending and C−O stretching modes contribute, but in addition the roles of the C=O stretching and C−H bending vibrations cannot be discarded (see Fig. 7.28) [27,30]. More details on this are described in the following section.

7.5.4 Anharmonic coupling in acetic acid dimers: Simulation of linear and two-dimensional infrared spectra

Several attempts have been made to analyze the lineshape of the O−H and/or O−D stretching band of acetic acid dimers in the gas and liquid phase as well as in matrices [37, 38, 240–246]. Besides the vibrational coupling mechanisms discussed in Sect. 7.2.2 inhomogeneous broadening resulting from different dimer structures, monomers or oligomers [247, 248] may contribute to the spectral width.

In this Section results are summarized on theoretical calculations based on DFT to investigate three mechanisms for vibrational coupling within the two intermolecular hydrogen bonds: (i) anharmonic coupling of the high-frequency O−H stretching mode to low-frequency modes, (ii) Fermi resonance coupling the of O−H stretching $v(\nu_{OH}) = 1$ state to fingerprint mode combination tones, and (iii) a combination of both [29]. Linear IR absorption spectra of the O−H stretching mode are simulated and compared to high-resolution IR spectra measured by supersonic jet Fourier transform spectroscopy [246, 249]. These cold gas phase spectra uncover much of the vibrational fine structure and can thus serve as a reference for zero temperature gas phase calculations (Fig. 7.29a). With subsequent extension to simulations of two-dimensional IR spectra [47, 250] the investigation of multidimensional signatures of the different coupling mechanisms has become possible [27, 30].

All quantum chemical calculations were carried out using DFT applying the B3LYP/6-311+G(d,p) method as implemented in Gaussian03 [251]. This study is restricted to the most commonly appearing C_{2h}-symmetric cyclic dimer structure (Fig. 7.20) the optimized structure of which is found to be in good agreement with earlier calculations [246, 249, 252].

Anharmonic multidimensional potential energy surfaces were calculated in the basis of dimensionless normal modes by expanding the potential energy V up to sixth-order in a selected set of modes. First-order and harmonic second-order off-diagonal force constants vanish at the equilibrium geometry. For higher-order force constants up to three-body interactions were included. Dipole moment derivatives were expanded to first-order only, thereby neglecting electrical anharmonicities, which are usually much smaller than mechanical ones [253, 254]. Cubic and higher-order force constants were calculated numerically by finite differences from analytical second-order force constants [52]. For benzoic acid dimers the validity of second-order perturbation theory with respect to vibrational modes in the fingerprint region has been critically examined [61]. It was found that standard perturbation theory accounts for anharmonic shifts of the vibrational modes in almost all cases. A notable exception, however, is the out-of-plane O−H bending mode, the accurate treatment of which requires multidimensional nonperturbative calculations at high quantum-chemical level.

The cyclic dimer exhibits C_{2h} symmetry and is thus subject to the IR-Raman exclusion rule. Upon dimerization all monomeric vibrations, which would be pairwise degenerate without coupling, experience excitonic or Davydov coupling and split into a set of *ungerade* (u) IR active and a set of *gerade* (g) Raman-active dimer modes [38, 243]. It should be noted that the one-dimensional potential energy surfaces for u modes are symmetric, whereas g modes have asymmetric potentials. For symmetric potential energy surfaces odd-order force constants vanish. Thus, the first anharmonic correction to IR active fundamental vibrations is in quartic order. The number of nonzero force constants is further reduced by symmetry. Only force constants, for which the product of irreducible representations of the respective coordinates involved in the force constant is totally symmetric, can be different from zero [62].

Vibrational eigenstates were calculated from an effective vibrational exciton Hamiltonian with up to 4 excitation quanta [29, 253, 255]. Calculated harmonic vibrational frequencies ω_i are usually too high with respect to experimental values. The deviation is mainly caused by missing anharmonic corrections as well as insufficient treatment of electron correlation of the quantum chemical method. Here, anharmonic corrections were included, but the imperfect treatment of electron correlation by the DFT B3LYP/6-311+G(d,p) method had to be accounted for. Therefore, harmonic force constants were scaled such that the frequencies of the fundamental vibrational modes resulting from the anharmonic vibrational Hamiltonian match experimental gas phase values [246, 249], which leads to scaling factors of about 0.98. The harmonic force constant for the $\nu_{OH}(b_u)$ mode was set to $2915\,\mathrm{cm}^{-1}$. This corresponds to a scaling factor of 0.90, which shows that the B3LYP method underestimates the strength of hydrogen bonding in acetic acid dimers. The assignments of the major subbands of the O$-$H stretching mode vibrational spectrum are relatively insensitive to a variation of scaling factors in a reasonably range, but for an accurate determination of the fine structure, scaling is important.

Femtosecond three-pulse photon echo studies have shown that the O$-$H stretching absorption spectrum is predominantly homogeneously broadened, whereas inhomogenous broadening can be neglected [22]. From the observed dephasing time $T_2 \approx 200\,\mathrm{fs}$ a homogeneous linewidth $\Gamma \approx 50\,\mathrm{cm}^{-1}$ is derived. In the following, calculated IR spectra with homogeneous linewidths (full width at half maximum) of $\Gamma = 1$ and $40\,\mathrm{cm}^{-1}$ will be presented. The latter value was found to fit the experimental spectrum measured in CCl_4 more appropriately than the value derived from the photon echo study.

Early treatments suggested anharmonic coupling to a single low-frequency mode, an intermolecular hydrogen bond stretching mode, together with Davydov coupling to be exclusively responsible for the vibrational line shape of the O$-$H stretching bands [37]. Dimerization gives rise to 6 new intermolecular vibrational modes. Because of the C_{2h} inversion symmetry of the acetic acid dimer, 3 of them are IR- (u) and 3 are Raman-active (g) (Fig. 7.25). They are characterized by distance as well as in- and out-of-plane angle modulations between the two hydrogen bonded monomers. These hydrogen bond modes are thus associated with relatively weak hydrogen bond forces and large reduced masses. Therefore, they all appear at low frequencies, that is below $200\,\mathrm{cm}^{-1}$ for acetic acid dimers [25, 238, 239, 256].

Upon coupling of the IR active ν_{OH} mode with Raman-active low-frequency modes, an IR active Franck-Condon series with one or several quanta of low-frequency modes arises [36]. Combining coherent femtosecond IR-pump$-$IR-probe spectroscopy and quantum chemical calculations 2 modes

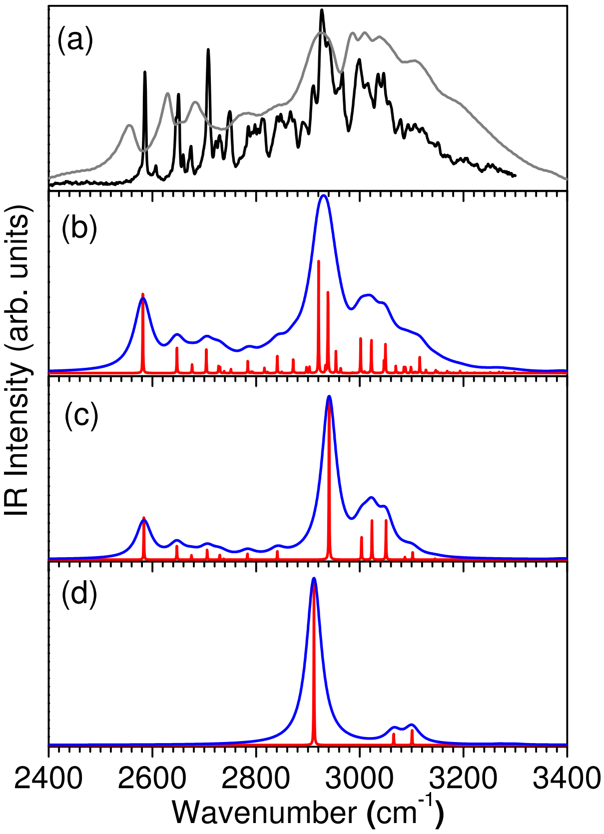

Fig. 7.29. $(CH_3{-}COOH)_2$: (a) Experimental IR absorption spectra: Cold gas phase spectrum (*black*) taken from [246] with permission and spectrum in CCl_4 (*gray*) measured at 298 K; (b-d) Calculated spectra (1 K) using homogeneous line widths of $\Gamma = 1$ (*red*) and 40 cm^{-1} (*blue*) including the following modes: $\nu_{OH}(b_u)$ + (b) fingerprint modes and $\delta_{dimer}(a_g)$ + $\nu_{dimer}(a_g)$; (c) fingerprint modes only; (d) $\delta_{dimer}(a_g)$ and $\nu_{dimer}(a_g)$ only.

were identified, which couple strongly to ν_{OH} [25]. These are the hydrogen bond bending ($\delta_{dimer}(a_g)$) and stretching ($\nu_{dimer}(a_g)$) modes absorbing at 145 and 170 cm^{-1}, respectively, which both modulate the hydrogen bond distance strongly (Fig. 7.25). Cubic coupling constants, which contribute most to anharmonic coupling, are about 150 and -145 cm^{-1} for $\delta_{dimer}(a_g)$ and $\nu_{dimer}(a_g)$, respectively. The IR spectrum based on 3 modes, $\nu_{OH}(b_u)$, $\delta_{dimer}(a_g)$ and $\nu_{dimer}(a_g)$, is shown in Fig. 7.29d. On a linear intensity scale a progression with only a single quantum of each low-frequency mode becomes visible. It can be concluded that a spectrum solely based on anharmonic coupling of $\nu_{OH}(b_u)$ to low-frequency modes can not account for the substructure and total width of the experimentally observed spectra shown in Fig. 7.29a.

Instead of coupling to low-frequency modes, multiple Fermi resonance coupling with combination tones of fingerprint vibrations has been considered to account for the width and substructure of the O$-$H stretching absorption spectrum [38, 242–245]. The relevance of Fermi resonances contributing to the substructure of the IR spectrum is supported by recent model calculations [246, 257]. With the exception of methyl group rocking and scissoring modes all IR active (b_u) fingerprint modes are included as well as their Raman-active (a_g) counterparts as only ungerade combination tones can directly interact with the $\nu_{OH}(b_u)$ high-frequency mode. These are the C$-$O (ν_{C-O}) and C=O ($\nu_{C=O}$) stretching modes, the O$-$H in-plane bending (δ_{OH}) and the methyl (γ_{CH3}) wagging modes (Fig. 7.28). It should be noted that none of the normal modes is local. Instead, in addition to a dominating contribution, O$-$H in-plane bending and methyl deformation motions mix into the normal coordinates. The O$-$H out-of-plane bending mode (γ_{OH}) was initially taken into account, but later on rejected from the Hamiltonian, because combination tones of this mode were shown not to contribute to the spectrum to any appreciable extent [29]. A linear IR spectrum for this model is shown in Fig. 7.29c. This spectrum accounts for major parts of the substructure of the experimental gas as well as solution phase spectra [22,29,246]. The vibrational fine structure, however, which is evident from the gas phase spectrum, is still lacking.

As neither anharmonic coupling to low-frequency modes nor Fermi resonance coupling to fingerprint combination bands sufficiently account for the observed lineshape of the O$-$H stretching band absorption, both mechanisms were merged into an 11-mode model. The resulting linear spectrum (Fig. 7.29b) shows a rich fine structure in good agreement with the experimental high-resolution gas phase and solution phase spectra (Fig. 7.29a) [22, 29, 246]. The more intense peaks in the linear spectrum are mostly dominated by Fermi resonances similar to the pure Fermi resonance spectrum without coupling to low-frequency modes (Fig. 7.29c). The low-frequency mode progressions build up on all Fermi resonance peaks forming the vibrational fine structure. Some low-frequency modes even gain intensities comparable to Fermi resonance bands [29]. The experimental spectrum measured in CCl_4 (Fig. 7.29a) shows broadening compared to the gas phase spectrum, whereby the overall width of the solution phase spectrum is reasonably well described by the calculated spectrum using a homogeneous linewidth of $\Gamma = 40\,\mathrm{cm}^{-1}$. Individual peaks observed in the gas phase spectrum merge into broader subbands. These solution phase subbands partly coincide with spectral features in the gas phase spectrum, but, as a consequence of shifted fundamental fingerprint vibrations, some of combination bands are also shifted. This is particularly obvious in the low-energy side of the spectrum below $2700\,\mathrm{cm}^{-1}$, where the solution phase bands are red-shifted with respect to their counterparts in the gas phase spectrum. All of the bands gain intensity from resonance coupling with $\nu_{OH}(b_u)$. However, as the $\nu_{OH}(b_u)$ intensity is spread over so many bands, its own contribution to individual states is relatively small. It is largest for the peak at 2920 cm^{-1}, which accordingly is the most intense peak in the spectrum with a contribution of about 15% for $\nu_{OH}(b_u)$. This corroborates the relevance of Fermi resonances in the O−H stretching IR absorption spectrum that was pointed out before [38,246,257]. However, a prominent role of a single Fermi resonance, namely the O−H stretching/bending coupling [257], which contributes to the medium intense band around 2840 cm^{-1} cannot be confirmed. The strongest anharmonic couplings are calculated for the combination bands on the red side of spectrum. This explains their relatively high peak intensities despite less fortunate resonance conditions.

The important role of low-frequency hydrogen bond bending and stretching modes in characterizing the O−H stretching IR absorption band as well as in providing efficient energy relaxation channels should be emphasized. This argument is supported by the recent experimental observation of coherent low-frequency motions after femtosecond excitation of the O−H stretching mode [25]. The strength of anharmonic coupling to low-frequency modes is on the same order of magnitude as Fermi resonance couplings. Low-frequency mode progressions in the IR spectra start at 2728 cm^{-1} and then insert over the remaining blue part of the spectrum. Some of the peaks gain intensities comparable to the weaker Fermi resonances.

To investigate the multidimensional signatures of the different coupling mechanisms, 2D-IR spectra were simulated based on the vibrational Hamiltonians described above. Thus, the estimated anharmonic coupling constants between the IR-active ν_{OH} mode and the fingerprint and low-frequency modes depicted in Figs. 7.25 and 7.28 have been used as input in the calculation of the nonlinear signals. Two-dimensional photon echo signals in the phase matching direction $k_{echo} = -k_1 + k_2 + k_3$ were calculated with parallel linear polarization applying the sum-over-states formalism [47,250]. The signal displayed in the frequency domain is given by:

$$S(\omega_3, T, \omega_1) = \int_{-\infty}^{\infty} dt_3 \int_{-\infty}^{\infty} dt_1 \, R_a(t_3, T, t_1) \exp(-i\omega_3 t_3 - i\omega_1 t_1) \; . \tag{7.16}$$

In the rotating wave approximation, the response function is given by a sum of Liouville space pathways (diagrams I, II, and III in Fig. 7.4), that is $R_a(t_3, T = 0, t_1) = R_I(t_3, T = 0, t_1) + R_{II}(t_3, T = 0, t_1) - R^*_{III}(t_3, T = 0, t_1)$. Liouville space pathways are calculated as a sum over all vibrational eigenstates [47,258]. They are proportional to a population factor of the initially occupied vibrational state, a polarization factor, a product of 4 transition dipole moments related to 4 infrared transitions, and a lineshape function, chosen here to be in the homogeneous limit. R_I and R_{II} describe transitions involving the ground and the first excited vibrational states giving rise to diagonal and cross peaks, while R_{III} describes transitions from one- to two-quantum states thereby adding excited state absorption to the spectra. For the calculation of 2D spectra, the three incident laser pulses were tuned to 2900 cm^{-1} assuming a rectangular electric field spectrum of ±400 cm^{-1} width

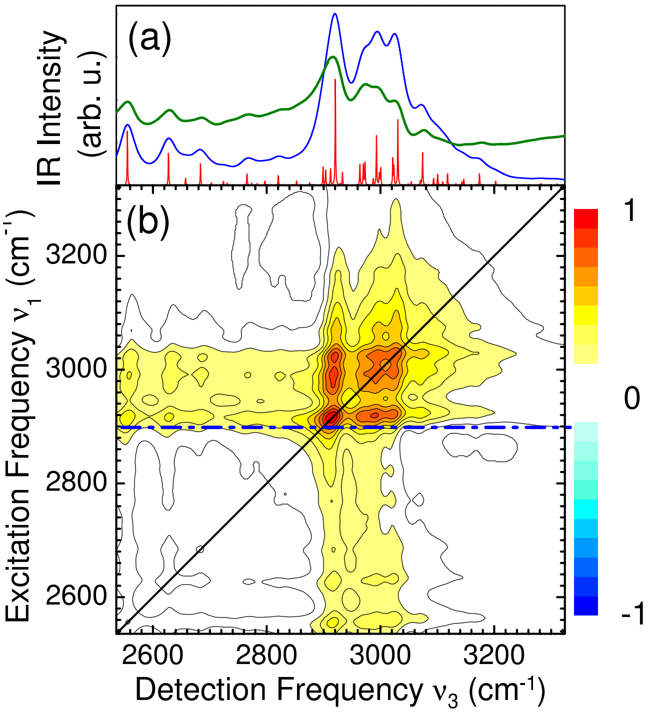

Fig. 7.30. (a) Calculated one-dimensional linear spectra with homogeneous linewidth of $\Delta\nu(fwhm) = 1$ (*red*) and $36\,\mathrm{cm}^{-1}$ (*blue*); cross section for an excitation frequency of $\nu_1 = 2921\,\mathrm{cm}^{-1}$ for ground state absorption (*green*); (b) Two-dimensional spectrum for a population time with zero- to one-quantum pathways only, with $\Delta\nu(fwhm) = 36\,\mathrm{cm}^{-1}$ (temperature 0 K), mimicking the population time $T = 400$ fs.

for selecting resonant transitions. A homogeneous linewidth of $\Delta\nu = 36\,\mathrm{cm}^{-1}$ was used.

A spectrum including ground state absorption only ($R_a = R_I$, $R_{II} = R_{III} = 0$, Fig. 7.30b) resembles conditions, where the excited state has decayed already into the hot ground state without conservation of phase memory [12]. This spectrum, which can be compared to the experimental 2D spectrum measured at $T = 400$ fs (Fig. 7.27c), contains only diagonal and cross peaks. The most striking diagonal and cross peaks are observed for the most intense bands in the linear spectrum, that is at $2921\,\mathrm{cm}^{-1}$ which is mainly due to the $\nu_{C-O}(b_u)/\nu_{C=O}(a_g)$ combination band with a cubic coupling constant with $\nu_{OH}(b_u)$ of $\Phi = -86\,\mathrm{cm}^{-1}$, at $2993\,\mathrm{cm}^{-1}$ ($\nu_{C-O}(a_g)/\nu_{C=O}(b_u)$, Φ $=48\,\mathrm{cm}^{-1}$) and at $3022/3031\,\mathrm{cm}^{-1}$ ($\gamma_{CH3}(b_u)/\nu_{C=O}(a_g)$, Φ $=62\,\mathrm{cm}^{-1}$; $\nu_{C-O}(a_g)/\delta_{OH}(b_u)/\delta_{dimer}(a_g)/\nu_{dimer}(a_g)$) [29]. In addition, prominent cross peaks exist for bands in the low-energy part of the spectrum, that is for the peak at $2555\,\mathrm{cm}^{-1}$ ($\nu_{C-O}(a_g)/\nu_{C-O}(b_u)$, Φ $=150\,\mathrm{cm}^{-1}$), at $2627\,\mathrm{cm}^{-1}$

($\nu_{C-O}(a_g)/\gamma_{CH3}(b_u), \Phi = -118\,\mathrm{cm}^{-1}$) and at $2684\,\mathrm{cm}^{-1}$ ($\nu_{C-O}(a_g)/\delta_{OH}(b_u)$, $\Phi = -126\,\mathrm{cm}^{-1}$). This coupling pattern within the O−H stretching band is also evident from a comparison of the cross section at $\nu_1 = 2921\,\mathrm{cm}^{-1}$ to the linear spectrum (Fig. 7.29a), where the off-diagonal bands, the peak intensities of which revealing the coupling strengths, match the resonance frequencies. From the good agreement with experimental results (Fig. 7.27) it can be concluded that Fermi resonances also dominate the $T = 400\,\mathrm{fs}$ experimental 2D spectrum. Low-frequency progressions make a minor contribution to the 2D spectra because of their substantially smaller transition dipoles. In going from anharmonic coupling of $\nu_{OH}(b_u)$ to low-frequency modes (3-mode model) to Fermi resonance coupling with fingerprint mode combination tones (9-mode model) to a combined mechanism (11-mode model) the number of individual 2D peaks grows considerably and the complexity of the vibrational signatures increases substantially. Introduction of homogeneous broadening causes many individual peaks to overlap to a single spectral feature. A comparison of the calculated linear spectra with high-resolution gas and solution phase spectra shows that only the combined mechanism accounts for the experimentally observed vibrational fine structure of the O−H stretching band demonstrating that both anharmonic coupling to low-frequency modes and Fermi resonance coupling are important vibrational coupling mechanisms for hydrogen bonds in acetic acid dimers. The corresponding 2D IR spectra, however, are dominated by vibrational signatures originating from cross peaks due to Fermi resonance coupling.

7.6 Outlook

The results presented in this chapter demonstrate how ultrafast nonlinear infrared spectroscopy allows for a separation of different microscopic couplings present in hydrogen-bonded systems. The X−H stretching oscillator is a sensitive probe for hydrogen bonding and the elucidation of its dynamics provides insight into the anharmonic couplings to other vibrational modes, such as X−H bending and hydrogen bond stretching modes, as well as to the (fluctuating) surroundings. Femtosecond infrared nonlinear spectroscopy and ab initio quantum chemical molecular dynamics have revealed for neat protic liquids, in particular water, the time scales for local fluctuations and associated loss of structural memory in the hydrogen-bonded networks. Energy redistribution and energy transport into the hydrogen bond stretching and librational modes deserve more attention of both experiment and theory as these modes are directly connected to the hydrogen bond networks. Future activities may involve the study of these hydrogen-bonded liquids in different situations, e.g. water in direct contact with biomolecular systems such as proteins and DNA.

In the case of the investigated medium-strong hydrogen-bonded molecular systems with well-defined geometries, the anharmonic couplings of high-frequency X−H stretching modes with low-frequency vibrations have been found to underly oscillatory wave packet motions contributing to the pump-probe signals. Coherent multidimensional spectroscopy, which was applied in the investigation of acetic acid dimers, has revealed the key role of Fermi and Davydov resonance couplings in the observed nonlinear signals.

The results obtained for PMME and cyclic acetic acid dimers demonstrate that coherent intermolecular motions persist for several picoseconds. This should allow for the development of control schemes using tailored vibrational wave packets prepared by excitation with phase-shaped infrared pulses. Moreover, as fingerprint vibrations such as the X−H bending mode couple strongly to X−H stretching motions, multicolor spectroscopy has to be explored further. For instance, both X−H stretching and X−H bending modes could be manipulated simultaneously to achieve control. With this the potential of optimal steering of hydrogen bond motions, and associated with that the control of hydrogen or proton transfer in double well potential systems should be explored.

Until now, the majority of studies have focused on the vibrational dynamics of hydrogen donating hydroxyl groups. Equally important are however amino groups, the hydrogen bonds of which can be found in nucleic acid base pairs in DNA and RNA, and in the formation of secondary structures in proteins, such as α-helices and β-sheets. Future application of ultrafast vibrational spectroscopy will provide a wealth of new information on hydrogen bonds in these biomolecular systems.

Cordial acknowledgment is being due to Jens Stenger, Dorte Madsen, Karsten Heyne, Nils Huse, R. J. Dwayne Miller, Barry. D. Bruner, Michael A. Cowan, Jason R. Dwyer, Satoshi Ashihara, Agathe Espagne, Holger Naundorf, Milena Petković, and Gennady K. Paramonov for their important contributions to the work describe here.

References

1. G.C. Pimentel, A.L. McClellan, *The hydrogen bond.* A Series of Chemistry Books (W.H. Freeman and Company, San Francisco and London, 1960)
2. P. Schuster, G. Zundel, C. Sandorfy (eds.), *The hydrogen bond: Recent developments in theory and experiments*, vol. I-III (North Holland, Amsterdam, 1976)
3. D. Hadži (ed.), *Theoretical treatments of hydrogen bonding* (John Wiley & Sons, Chichester, 1997)
4. S. Scheiner, *Hydrogen bonding: A theoretical perspective* (Oxford University Press, New York, 1997)
5. D. Hadži, S. Bratos, in *The hydrogen bond: Recent developments in theory and experiments*, vol. II. Structure and spectroscopy, ed. by P. Schuster, G. Zundel, C. Sandorfy (North Holland, Amsterdam, The Netherlands, 1976), p. 565
6. M.D. Fayer (ed.), *Ultrafast infrared and Raman spectroscopy.* Practical Spectroscopy Series Vol. 26 (Marcel Dekker, Inc., New York, 2001)

7. E.T.J. Nibbering, T. Elsaesser, Chem. Rev. **104**, 1887 (2004)
8. J. Stenger, D. Madsen, J. Dreyer, E.T.J. Nibbering, P. Hamm, T. Elsaesser, J. Phys. Chem. A **105**, 2929 (2001)
9. D. Madsen, J. Stenger, J. Dreyer, E.T.J. Nibbering, P. Hamm, T. Elsaesser, Chem. Phys. Lett. **341**, 56 (2001)
10. J. Stenger, D. Madsen, P. Hamm, E.T.J. Nibbering, T. Elsaesser, Phys. Rev. Lett. **87**, 027401 (2001)
11. J. Stenger, D. Madsen, J. Dreyer, P. Hamm, E.T.J. Nibbering, T. Elsaesser, Chem. Phys. Lett. **354**, 256 (2002)
12. J. Stenger, D. Madsen, P. Hamm, E.T.J. Nibbering, T. Elsaesser, J. Phys. Chem. A **106**, 2341 (2002)
13. D. Madsen, J. Stenger, J. Dreyer, P. Hamm, E.T.J. Nibbering, T. Elsaesser, Bull. Chem. Soc. Jpn. **75**, 909 (2002)
14. G.K. Paramonov, H. Naundorf, O. Kühn, Eur. J. Phys. D **14**, 205 (2001)
15. O. Kühn, J. Phys. Chem. A **106**, 7671 (2002)
16. H. Naundorf, G.A. Worth, H.D. Meyer, O. Kühn, J. Phys. Chem. A **106**, 719 (2002)
17. H. Naundorf, O. Kühn, in *Femtochemistry and Femtobiology*, ed. by A. Douhal, J. Santamaria (World Scientific, Singapore, 2002), p. 438
18. O. Kühn, H. Naundorf, Phys. Chem. Chem. Phys. **5**, 79 (2003)
19. M. Petković, O. Kühn, Chem. Phys. **304**, 91 (2004)
20. K. Heyne, N. Huse, E.T.J. Nibbering, T. Elsaesser, Chem. Phys. Lett. **369**, 591 (2003)
21. K. Heyne, N. Huse, E.T.J. Nibbering, T. Elsaesser, J. Phys.: Condens. Matter **15**, S129 (2003)
22. N. Huse, K. Heyne, J. Dreyer, E.T.J. Nibbering, T. Elsaesser, Phys. Rev. Lett. **91**, 197401 (2003)
23. K. Heyne, N. Huse, E.T.J. Nibbering, T. Elsaesser, Chem. Phys. Lett. **382**, 19 (2003)
24. K. Heyne, N. Huse, J. Dreyer, E.T.J. Nibbering, T. Elsaesser, S. Mukamel, J. Chem. Phys. **121**, 902 (2004)
25. K. Heyne, E.T.J. Nibbering, T. Elsaesser, M. Petković, O. Kühn, J. Phys. Chem. A **108**, 6083 (2004)
26. M.L. Cowan, B.D. Bruner, N. Huse, J.R. Dwyer, B. Chugh, E.T.J. Nibbering, T. Elsaesser, R.J.D. Miller, Nature **434**, 199 (2005)
27. N. Huse, B.D. Bruner, M.L. Cowan, J. Dreyer, E.T.J. Nibbering, R.J.D. Miller, T. Elsaesser, Phys. Rev. Lett. **95**, 147402 (2005)
28. N. Huse, S. Ashihara, E.T.J. Nibbering, T. Elsaesser, Chem. Phys. Lett. **404**, 389 (2005)
29. J. Dreyer, J. Chem. Phys. **122**, 184306 (2005)
30. J. Dreyer, Int. J. Quant. Chem. **104**, 782 (2005)
31. S. Ashihara, N. Huse, A. Espagne, E.T.J. Nibbering, T. Elsaesser, Chem. Phys. Lett. **424**, 66 (2006)
32. K. Giese, M. Petković, H. Naundorf, O. Kühn, Phys. Rep. **430**, 211 (2006)
33. A. Novak, Structure and Bonding (Berlin) **18**, 177 (1974)
34. W. Mikenda, J. Mol. Struct. **147**, 1 (1986)
35. W. Mikenda, S. Steinböck, J. Mol. Struct. **384**, 159 (1996)
36. B.I. Stepanov, Nature **157**, 808 (1946)
37. Y. Marechal, A. Witkowski, J. Chem. Phys. **48**, 3697 (1968)

38. Y. Maréchal, J. Chem. Phys. **87**, 6344 (1987)
39. O. Henri-Rousseau, P. Blaise, D. Chamma, Adv. Chem. Phys. **121**, 241 (2002)
40. P. Hamm, R.M. Hochstrasser, in *Ultrafast infrared and Raman spectroscopy*, ed. by M.D. Fayer (Marcel Dekker, Inc., New York, 2001), p. 273
41. R. Janoschek, E.G. Weidemann, G. Zundel, B. Johnson, J. Chem. Soc. Faraday Trans. II **69**, 505 (1973)
42. N. Rösch, M.A. Ratner, J. Chem. Phys. **61**, 3344 (1974)
43. S. Bratos, J. Chem. Phys. **63**, 3499 (1975)
44. G.N. Robertson, J. Yarwood, Chem. Phys. **32**, 267 (1978)
45. B. Boulil, O. Henri-Rousseau, P. Blaise, Chem. Phys. **126**, 263 (1988)
46. R. Kubo, Adv. Chem. Phys. **15**, 101 (1969)
47. S. Mukamel, *Principles of nonlinear optical spectroscopy*, *Oxford Series in Optical and Imaging Sciences*, vol. 6 (Oxford University Press, Oxford, 1995)
48. G.A. Jeffrey, *Introduction to hydrogen bonding* (Oxford University Press, New York, 1997)
49. A.G. Császár, in *The encyclopedia of Computational Chemistry*, ed. by P. Schleyer, N. Allinger, T. Clark, J. Gasteiger, P.A. Kollman, H.A. Schaefer III, P.R. Schreiner (John Wiley and Sons, Chichester, 1998), p. 13
50. J. Gauss, in *Modern methods and algorithms in Quantum Chemistry, NIC*, vol. 3, ed. by J. Grotendorst (John von Neumann Institute for Computing, Jülich, 2000), p. 541
51. G.C. Schatz, in *Reaction and molecular dynamics, Lecture notes in Chemistry*, vol. 14, ed. by A. Lagana, A. Riganelli (Springer, Berlin, 2000), p. 15
52. W. Schneider, W. Thiel, Chem. Phys. Lett. **157**, 367 (1989)
53. S. Dressler, W. Thiel, Chem. Phys. Lett. **273**, 71 (1997)
54. A.D. Boese, W. Klopper, J.M.L. Martin, Mol. Phys. **103**, 863 (2005)
55. J.M. Bowman, S. Carter, N.C. Handy, in *Theory and applications of Computational Chemistry: The first forty years*, ed. by C. Dykstra, G. Frenking, K.S. Kim (Elsevier Science Publishing Company, 2005), p. 251
56. R.B. Gerber, G.M. Chaban, B. Brauer, Y. Miller, in *Theory and applications of Computational Chemistry: The first forty years*, ed. by C. Dykstra, G. Frenking, K.S. Kim (Elsevier Science Publishing Company, 2005), p. 165
57. W.A. Lester, Jr., B.L. Hammond, Annu. Rev. Phys. Chem. **41**, 283 (1990)
58. J.B. Anderson, Rev. Comp. Chem. **13**, 132 (1999)
59. Z. Bačić, J.C. Light, Annu. Rev. Phys. Chem. **40**, 469 (1989)
60. M.V. Vener, O. Kühn, J.M. Bowman, Chem. Phys. Lett. **349**, 562 (2001)
61. J. Antony, G. von Helden, G. Meijer, B. Schmidt, J. Chem. Phys. **123**, 014305 (2005)
62. G. Herzberg, *Molecular spectra and molecular structure. II. Infrared and Raman spectra of polyatomic molecules* (Van Nostrand, Princeton, 1945)
63. J.R. Fair, O. Votava, D.J. Nesbitt, J. Chem. Phys. **108**, 72 (1998)
64. M. Khalil, A. Tokmakoff, Chem. Phys. **266**, 213 (2001)
65. M. Khalil, N. Demirdöven, A. Tokmakoff, J. Phys. Chem. A **107**, 5258 (2003)
66. M.P. Allen, D.J. Tildesley, *Computer simulation of liquids* (Oxford University Press, New York, 1987)
67. W. Wang, O. Donini, C.M. Reyes, P.A. Kollman, Annu. Rev. Biophys. Biomol. Struct. **30**, 211 (2001)
68. A.D. Mackerell, Jr., J. Comput. Chem. **25**, 1584 (2004)

69. J.J.P. Stewart, in *The encyclopedia of Computational Chemistry*, ed. by P. Schleyer, N. Allinger, T. Clark, J. Gasteiger, P.A. Kollman, H.A. Schaefer III, P.R. Schreiner (John Wiley and Sons, Chichester, 1998), p. 1263
70. J.E. Del Bene, M.J.T. Jordan, Int. Rev. Phys. Chem. **18**, 119 (1999)
71. S.F. Boys, F. Bernardi, Mol. Phys. **19**, 553 (1970)
72. F.B. van Duijneveldt, J.G.C.M. van Duijneveldt-van de Rijdt, J.H. van Lenthe, Chem. Rev. **94**, 1873 (1994)
73. P. Hobza, Annu. Rep. Prog. Chem. Sect. C **100**, 3 (2004)
74. W. Koch, M.C. Holthausen, *A chemist's guide to density functional theory*, 2nd edn. (Wiley-VCH, Weinheim, 2001)
75. J. Ireta, J. Neugebauer, M. Scheffler, J. Phys. Chem. A **108**, 5692 (2004)
76. J. Černý, P. Hobza, Phys. Chem. Chem. Phys. **7**, 1624 (2005)
77. E.R. Johnson, A.D. Becke, J. Chem. Phys. **124**, 174104 (2006)
78. Y. Zhao, O. Tishchenko, D.G. Truhlar, J. Phys. Chem. B **109**, 19046 (2005)
79. P. Jurečka, P. Nachtigall, P. Hobza, Phys. Chem. Chem. Phys. **3**, 4578 (2001)
80. B.M. Ladanyi, M.S. Skaf, Annu. Rev. Phys. Chem. **44**, 335 (1993)
81. I. Ohmine, S. Saito, Acc. Chem. Res. **32**, 741 (1999)
82. G. Sutmann, in *Quantum simulations of complex many-body systems: From theory to algorithms*, *NIC series*, vol. 10, ed. by J. Grotendorst, D. Marx, A. Muramatsu (John von Neumann Institute for Computing, Jülich, 2002), p. 211
83. D. Marx, J. Hutter, in *Modern methods and algorithms of Quantum Chemistry*, *NIC series*, vol. 1, ed. by J. Grotendorst (John von Neumann Institute for Computing, Jülich, 2000), p. 1
84. R. Iftimie, P. Minary, M.E. Tuckerman, Proc. Natl. Acad. Sci. USA **102**, 6654 (2005)
85. D. Marx, in *Computational nanoscience: Do It yourself!*, *NIC series*, vol. 31, ed. by J. Grotendorst, S. Blügel, D. Marx (John von Neumann Institute for Computing, Jülich, 2006), p. 195
86. D. Marx, ChemPhysChem **7**, 1848 (2006)
87. K. Laasonen, M. Sprik, M. Parrinello, R. Car, J. Chem. Phys. **99**, 9080 (1993)
88. P.L. Silvestrelli, M. Parrinello, J. Chem. Phys. **111**, 3572 (1999)
89. P.L. Geissler, C. Dellago, D. Chandler, J. Hutter, M. Parrinello, Science **291**, 2121 (2001)
90. E. Tsuchida, Y. Kanada, M. Tsukada, Chem. Phys. Lett. **311**, 236 (1999)
91. M.E. Tuckerman, D. Marx, M.L. Klein, M. Parinello, Science **275**, 817 (1997)
92. D. Marx, M.E. Tuckerman, J. Hutter, M. Parinello, Nature **397**, 901 (1999)
93. G.A. Voth, Acc. Chem. Res. **39**, 143 (2006)
94. M. Eichinger, P. Tavan, J. Hutter, M. Parrinello, J. Chem. Phys. **110**, 10452 (1999)
95. J. Gao, D.G. Truhlar, Annu. Rev. Phys. Chem. **53**, 467 (2002)
96. R.A. Friesner, V. Guallar, Annu. Rev. Phys. Chem. **56**, 389 (2005)
97. J. Park, J.H. Ha, R.M. Hochstrasser, J. Chem. Phys. **121**, 7281 (2004)
98. W.T. Pollard, R.A. Mathies, Annu. Rev. Phys. Chem. **43**, 497 (1992)
99. H.K. Nienhuys, S. Woutersen, R.A. van Santen, H.J. Bakker, J. Chem. Phys. **111**, 1494 (1999)
100. A.J. Lock, H.J. Bakker, J. Chem. Phys. **117**, 1708 (2002)
101. M.A.F.H. van den Broek, M.F. Kropman, H.J. Bakker, Chem. Phys. Lett. **357**, 8 (2002)

102. P. Hamm, S.M. Ohline, W. Zinth, J. Chem. Phys. **106**, 519 (1997)
103. E.T.J. Nibbering, H. Fidder, E. Pines, Annu. Rev. Phys. Chem. **56**, 337 (2005)
104. J.C. Deàk, S.T. Rhea, L.K. Iwaki, D.D. Dlott, J. Phys. Chem. A **104**, 4866 (2000)
105. D. Dlott, Chem. Phys. **266**, 149 (2001)
106. V. Kozich, J. Dreyer, S. Ashihara, W. Werncke, T. Elsaesser, J. Chem. Phys. **125**, 074504 (2006)
107. G.R. Fleming, M. Cho, Annu. Rev. Phys. Chem. **47**, 109 (1996)
108. W.P. de Boeij, M.S. Pshenichnikov, D.A. Wiersma, Annu. Rev. Phys. Chem. **49**, 99 (1998)
109. S. Yeremenko, M.S. Pshenichnikov, D.A. Wiersma, Chem. Phys. Lett. **369**, 107 (2003)
110. S. Yeremenko, M.S. Pshenichnikov, D.A. Wiersma, Phys. Rev. A **73**, 021804 (2006)
111. C.J. Fecko, J.D. Eaves, J.J. Loparo, A. Tokmakoff, P.L. Geissler, Science **301**, 1698 (2003)
112. C.J. Fecko, J.J. Loparo, S.T. Roberts, A. Tokmakoff, J. Chem. Phys. **122**, 054506 (2005)
113. J.B. Asbury, T. Steinel, C. Stromberg, S.A. Corcelli, C.P. Lawrence, J.L. Skinner, M.D. Fayer, J. Phys. Chem. A **108**, 1107 (2004)
114. T. Steinel, J.B. Asbury, S.A. Corcelli, C.P. Lawrence, J.L. Skinner, M.D. Fayer, Chem. Phys. Lett. **386**, 295 (2004)
115. J.B. Asbury, T. Steinel, K. Kwak, S.A. Corcelli, C.P. Lawrence, J.L. Skinner, M.D. Fayer, J. Chem. Phys. **121**, 12431 (2004)
116. H.S. Tan, I.R. Piletic, R.E. Riter, N.E. Levinger, M.D. Fayer, Phys. Rev. Lett. **94**, 057405 (2005)
117. J.B. Asbury, T. Steinel, C. Stromberg, K.J. Gaffney, I.R. Piletic, A. Goun, M.D. Fayer, Chem. Phys. Lett. **374**, 362 (2003)
118. J.B. Asbury, T. Steinel, C. Stromberg, K.J. Gaffney, I.R. Piletic, A. Goun, M.D. Fayer, Phys. Rev. Lett. **91**, 237402 (2003)
119. J.B. Asbury, T. Steinel, M.D. Fayer, J. Phys. Chem. B **108**, 6544 (2004)
120. I.V. Rubtsov, K. Kumar, R.M. Hochstrasser, Chem. Phys. Lett. **402**, 439 (2005)
121. Y.S. Kim, R. Hochstrasser, Proc. Natl. Acad. Sci. USA **102**, 11185 (2005)
122. M.C. Asplund, M.T. Zanni, R.M. Hochstrasser, Proc. Natl. Acad. Sci. USA **97**, 8219 (2000)
123. M.L. Cowan, J.P. Ogilvie, R.J.D. Miller, Chem. Phys. Lett. **386**, 184 (2004)
124. H. Eichler, H. Stahl, J. Appl. Phys. **44**, 3429 (1973)
125. H.J. Eichler, Optica Acta **24**, 631 (1977)
126. M.D. Fayer, Annu. Rev. Phys. Chem. **33**, 63 (1982)
127. N.A. Kurnit, S.R. Hartmann, I.D. Abella, Phys. Rev. Lett. **13**, 567 (1964)
128. T.J. Aartsma, D.A. Wiersma, Phys. Rev. Lett. **36**, 1360 (1976)
129. D. Zimdars, A. Tokmakoff, S. Chen, S.R. Greenfield, M.D. Fayer, T.I. Smith, H.A. Schwettman, Phys. Rev. Lett. **70**, 2718 (1993)
130. K. Duppen, D.A. Wiersma, J. Opt. Soc. Am. B **3**, 614 (1986)
131. T. Joo, Y. Jia, J.Y. Yu, M.J. Lang, G.R. Fleming, J. Chem. Phys. **104**, 6089 (1996)
132. W.P. de Boeij, M.S. Pshenichnikov, D.A. Wiersma, Chem. Phys. Lett. **253**, 53 (1996)

133. K. Duppen, D.P. Weitekamp, D.A. Wiersma, Chem. Phys. Lett. **108**, 551 (1984)
134. R.M. Hochstrasser, N.H. Ge, S. Gnanakaran, M.T. Zanni, Bull. Chem. Soc. Jpn. **75**, 1103 (2002)
135. I.V. Rubtsov, J. Wang, R.M. Hochstrasser, J. Chem. Phys. **118**, 7733 (2003)
136. P. Hamm, M. Lim, W.F. DeGrado, R.M. Hochstrasser, Proc. Natl. Acad. Sci. USA **96**, 2036 (1999)
137. M. Khalil, N. Demirdöven, A. Tokmakoff, Phys. Rev. Lett. **90**, 047401 (2003)
138. J. Bredenbeck, J. Helbing, R. Behrendt, C. Renner, L. Moroder, J. Wachtveitl, P. Hamm, J. Phys. Chem. B **107**, 8654 (2003)
139. J. Bredenbeck, J. Helbing, P. Hamm, J. Am. Chem. Soc. **126**, 990 (2004)
140. R.R. Ernst, G. Bodenhausen, A. Wokaun, *Principles of nuclear magnetic resonance in one and two dimensions* (Clarendon, Oxford, 1987)
141. W.P. Aue, E. Bartholdi, R.R. Ernst, J. Chem. Phys. **64**, 2229 (1976)
142. P. Hamm, M. Lim, R.M. Hochstrasser, J. Phys. Chem. B **102**, 6123 (1998)
143. S. Woutersen, P. Hamm, J. Phys. Chem. B **104**, 11316 (2000)
144. S. Woutersen, Y. Mu, G. Stock, P. Hamm, Proc. Natl. Acad. Sci. USA **98**, 11254 (2001)
145. S. Woutersen, R. Pfister, P. Hamm, Y. Mu, D.S. Kosov, G. Stock, J. Chem. Phys. **117**, 6833 (2002)
146. S. Woutersen, P. Hamm, J. Phys.: Condens. Matter **14**, R1035 (2002)
147. K. Kwac, M. Cho, J. Chem. Phys. **119**, 2256 (2003)
148. O. Golonzka, M. Khalil, N. Demirdöven, A. Tokmakoff, Phys. Rev. Lett. **86**, 2154 (2001)
149. M.T. Zanni, N.H. Ge, Y.S. Kim, R.M. Hochstrasser, Proc. Natl. Acad. Sci. USA **98**, 11265 (2001)
150. M.T. Zanni, S. Gnanakaran, J. Stenger, R.M. Hochstrasser, J. Phys. Chem. B **105**, 6520 (2001)
151. M. Zanni, R.M. Hochstrasser, Curr. Opin. Struct. Biol. **11**, 516 (2001)
152. A.T. Krummel, P. Mukherjee, M.T. Zanni, J. Phys. Chem. B. **107**, 9165 (2003)
153. M. Khalil, N. Demirdöven, A. Tokmakoff, J. Chem. Phys. **121**, 362 (2004)
154. I.R. Piletic, K.J. Gaffney, M.D. Fayer, J. Chem. Phys. **119**, 423 (2003)
155. J.B. Asbury, T. Steinel, C. Stromberg, K.J. Gaffney, I.R. Piletic, M.D. Fayer, J. Chem. Phys. **119**, 12981 (2003)
156. I.R. Piletic, H.S. Tan, M.D. Fayer, J. Phys. Chem. B **109**, 21273 (2005)
157. J. Zheng, K. Kwak, J. Asbury, X. Chen, I.R. Piletic, M.D. Fayer, Science **309**, 1338 (2005)
158. J. Zheng, K. Kwak, X. Chen, J.B. Asbury, M.D. Fayer, J. Am. Chem. Soc. **128**, 2977 (2006)
159. P. Hamm, R.A. Kaindl, J. Stenger, Opt. Lett. **25**, 1798 (2000)
160. R.A. Kaindl, M. Wurm, K. Reimann, P. Hamm, A.M. Weiner, M. Woerner, J. Opt. Soc. Am. B **17**, 2086 (2000)
161. V. Volkov, R. Schanz, P. Hamm, Opt. Lett. **30**, 2010 (2005)
162. P. Tian, D. Keusters, Y. Suzaki, W.S. Warren, Science **300**, 1553 (2003)
163. G.M. Gale, G. Gallot, F. Hache, N. Lascoux, S. Bratos, J.C. Leicknam, Phys. Rev. Lett. **82**, 1068 (1999)
164. S. Bratos, J.C. Leicknam, G. Gallot, H. Ratajczak, in *Ultrafast hydrogen bonding dynamics and proton transfer processes in the condensed phase*, *Understanding chemical reactivity*, vol. 23, ed. by T. Elsaesser, H.J. Bakker (Kluwer Academic Publishers, Dordrecht, 2002), p. 5

165. R. Rey, K.B. Møller, J.T. Hynes, J. Phys. Chem. A **106**, 11993 (2002)
166. K.B. Møller, R. Rey, J.T. Hynes, J. Phys. Chem. A **108**, 1275 (2004)
167. C.P. Lawrence, J.L. Skinner, J. Chem. Phys. **118**, 264 (2003)
168. R. Torre, P. Bartolini, R. Righini, Nature **428**, 296 (2004)
169. P. Wernet, D. Nordlund, U. Bergmann, M. Cavalleri, M. Odelius, H. Ogasawara, L.A. Naslund, T.K. Hirsch, L. Ojamae, P. Glatzel, L.G.M. Pettersson, A. Nilsson, Science **304**, 995 (2004)
170. J.D. Smith, C.D. Cappa, K.R. Wilson, B.M. Messer, R.C. Cohen, R.J. Saykally, Science **306**, 851 (2004)
171. A. Nilsson, P. Wernet, D. Nordlund, U. Bergmann, M. Cavalleri, M. Odelius, H. Ogasawara, L.A. Naslund, T.K. Hirsch, L. Ojamae, P. Glatzel, L.G.M. Pettersson, Science **308**, 793 (2005)
172. J.D. Smith, C.D. Cappa, B.M. Messer, R.C. Cohen, R.J. Saykally, Science **308**, 793 (2005)
173. A. Luzar, D. Chandler, Nature **379**, 55 (1996)
174. A. Luzar, D. Chandler, Phys. Rev. Lett. **76**, 928 (1996)
175. G. Reddy, C.P. Lawrence, J.L. Skinner, A. Yethiraj, J. Chem. Phys. **119**, 13012 (2003)
176. D. Xenides, B.R. Randolf, B.M. Rode, J. Chem. Phys. **122**, 174506 (2005)
177. D.W. Oxtoby, D. Levesque, J.J. Weis, J. Chem. Phys. **68**, 5528 (1978)
178. D.W. Oxtoby, Adv. Chem. Phys. **40**, 1 (1979)
179. J.J. Loparo, C.J. Fecko, J.D. Eaves, S.T. Roberts, A. Tokmakoff, Phys. Rev. B **70**, 180201 (2004)
180. C.J. Burnham, S.S. Xantheas, J. Chem. Phys. **116**, 5115 (2002)
181. C.J. Burnham, S.S. Xantheas, M.A. Miller, B.E. Applegate, R.E. Miller, J. Chem. Phys. **117**, 1109 (2002)
182. G.S. Fanourgakis, E. Apra, W.A. de Jong, S.S. Xantheas, J. Chem. Phys. **122**, 134304 (2005)
183. A. Lagutschenkov, G.S. Fanourgakis, G. Niedner-Schatteburg, S.S. Xantheas, J. Chem. Phys. **122**, 194310 (2005)
184. C.P. Lawrence, J.L. Skinner, J. Chem. Phys. **117**, 5827 (2002)
185. C.P. Lawrence, J.L. Skinner, J. Chem. Phys. **117**, 8847 (2002)
186. S.A. Corcelli, C.P. Lawrence, J.B. Asbury, T. Steinel, M.D. Fayer, J.L. Skinner, J. Chem. Phys. **121**, 8897 (2004)
187. S.A. Corcelli, C.P. Lawrence, J.L. Skinner, J. Chem. Phys. **120**, 8107 (2004)
188. T. Hayashi, T. la Cour Jansen, W. Zhuang, S. Mukamel, J. Phys. Chem. A **109**, 64 (2005)
189. S.A. Corcelli, J.L. Skinner, J. Phys. Chem. A **109**, 6154 (2005)
190. J.R. Schmidt, S.A. Corcelli, J.L. Skinner, J. Chem. Phys. **123**, 044513 (2005)
191. C.P. Lawrence, J.L. Skinner, Proc. Natl. Acad. Sci. USA **102**, 6720 (2005)
192. S. Bratos, J.C. Leicknam, S. Pommeret, G. Gallot, J. Mol. Struct. **708**, 197 (2004)
193. S. Woutersen, H.J. Bakker, Nature **402**, 507 (1999)
194. W. Amir, G. Gallot, F. Hache, J. Chem. Phys. **121**, 7908 (2004)
195. J.A. Poulsen, G. Nyman, S. Nordholm, J. Phys. Chem. A **107**, 8420 (2003)
196. D. Laage, H. Demirdjian, J.T. Hynes, Chem. Phys. Lett. **405**, 453 (2005)
197. R. DeVane, B. Space, A. Perry, C. Neipert, C. Ridley, T. Keyes, J. Chem. Phys. **121**, 3688 (2004)
198. D. Laage, J.T. Hynes, Science **311**, 832 (2006)

199. T. Elsaesser, W. Kaiser, Annu. Rev. Phys. Chem. **42**, 83 (1991)
200. J.C. Owrutsky, D. Raftery, R.M. Hochstrasser, Annu. Rev. Phys. Chem. **45**, 519 (1994)
201. R. Rey, K.B. Møller, J.T. Hynes, Chem. Rev. **104**, 1915 (2004)
202. R. Rey, J.T. Hynes, J. Chem. Phys. **104**, 2356 (1996)
203. H. Graener, G. Seifert, A. Laubereau, Chem. Phys. **175**, 193 (1993)
204. H. Graener, G. Seifert, J. Chem. Phys. **98**, 36 (1993)
205. D. Cringus, S. Yeremenko, M.S. Pshenichnikov, D.A. Wiersma, J. Phys. Chem. B **108**, 10376 (2004)
206. A.J. Lock, S. Woutersen, H.J. Bakker, J. Phys. Chem. A **105**, 1238 (2001)
207. D.W. Oxtoby, Annu. Rev. Phys. Chem. **32**, 77 (1981)
208. M.F. Kropman, H.J. Bakker, J. Am. Chem. Soc. **126**, 9135 (2004)
209. A.W. Omta, M.F. Kropman, S. Woutersen, H.J. Bakker, J. Chem. Phys. **119**, 12457 (2003)
210. K.B. Møller, R. Rey, M. Masia, J.T. Hynes, J. Chem. Phys. **122**, 114508 (2005)
211. A.M. Dokter, S. Woutersen, H.J. Bakker, Phys. Rev. Lett. **94**, 178301 (2005)
212. D. Cringus, J. Lindner, M.T.W. Milder, M.S. Pshenichnikov, P. Vöhringer, D.A. Wiersma, Chem. Phys. Lett. **408**, 162 (2005)
213. H.S. Tan, I.R. Piletic, M.D. Fayer, J. Chem. Phys. **122**, 174501 (2005)
214. G. Seifert, T. Patzlaff, H. Graener, J. Chem. Phys. **120**, 8866 (2004)
215. Z.H. Wang, Y.S. Pang, D.D. Dlott, J. Chem. Phys. **120**, 8345 (2004)
216. O.F.A. Larsen, S. Woutersen, J. Chem. Phys. **121**, 12143 (2004)
217. P. Bodis, O.F.A. Larsen, S. Woutersen, J. Phys. Chem. A **109**, 5303 (2005)
218. C.P. Lawrence, J.L. Skinner, J. Chem. Phys. **119**, 1623 (2003)
219. C.P. Lawrence, J.L. Skinner, J. Chem. Phys. **119**, 3840 (2003)
220. A. Pakoulev, Z. Wang, Y. Pang, D.D. Dlott, Chem. Phys. Lett. **380**, 404 (2003)
221. H.J. Bakker, A.J. Lock, D. Madsen, Chem. Phys. Lett. **385**, 329 (2004)
222. A. Pakoulev, Z.H. Wang, Y.S. Pang, D.D. Dlott, Chem. Phys. Lett. **385**, 332 (2004)
223. H.J. Bakker, A.J. Lock, D. Madsen, Chem. Phys. Lett. **384**, 236 (2004)
224. T. Patzlaff, M. Janich, G. Seifert, H. Graener, Chem. Phys. **261**, 381 (2000)
225. G. Seifert, T. Patzlaff, H. Graener, Phys. Rev. Lett. **88**, 147402 (2002)
226. J.C. Deàk, Y. Pang, T.D. Sechler, Z. Wang, D.D. Dlott, Science **306**, 473 (2004)
227. Z.H. Wang, Y. Pang, D.D. Dlott, Chem. Phys. Lett. **397**, 40 (2004)
228. Z.H. Wang, A. Pakoulev, Y. Pang, D.D. Dlott, J. Phys. Chem. A **108**, 9054 (2004)
229. J. Lindner, P. Vöhringer, M.S. Pshenichnikov, D. Cringus, D.A. Wiersma, M. Mostovoy, Chem. Phys. Lett. **421**, 329 (2006)
230. T. Steinel, J.B. Asbury, J. Zheng, M.D. Fayer, J. Phys. Chem. A **108**, 10957 (2004)
231. S. Woutersen, Y. Mu, G. Stock, P. Hamm, Chem. Phys. **266**, 137 (2001)
232. J. Zheng, K. Kwak, J. Xie, M.D. Fayer, Science **313**, 1951 (2006)
233. P. Blaise, O. Henri-Rousseau, A. Grandjean, Chem. Phys. **244**, 405 (1999)
234. M.H. Beck, A. Jäckle, G.A. Worth, H.D. Meyer, Phys. Rep. **324**, 1 (2000)
235. V. May, O. Kühn, *Charge and energy transfer dynamics in molecular systems, 2nd revised and enlarged edition* (Wiley–VCH, Weinheim, 2004)
236. M. Lim, R.M. Hochstrasser, J. Chem. Phys. **115**, 7629 (2001)
237. G. Seifert, T. Patzlaff, H. Graener, Chem. Phys. Lett. **333**, 248 (2001)

238. O. Faurskov Nielsen, P.A. Lund, J. Chem. Phys. **78**, 652 (1983)
239. T. Nakabayashi, K. Kosugi, N. Nishi, J. Phys. Chem. A **103**, 8595 (1999)
240. M. Haurie, A. Novak, J. Chim. Phys. **62**, 146 (1965)
241. Y. Greenie, J.C. Cornut, J.C. Lassegues, J. Chem. Phys. **55**, 5844 (1971)
242. R.L. Redington, K.C. Lin, J. Chem. Phys. **54**, 4111 (1971)
243. D. Chamma, O. Henri-Rousseau, Chem. Phys. **248**, 53 (1999)
244. D. Chamma, O. Henri-Rousseau, Chem. Phys. **248**, 71 (1999)
245. D. Chamma, O. Henri-Rousseau, Chem. Phys. **248**, 91 (1999)
246. C. Emmeluth, M.A. Suhm, D. Luckhaus, J. Chem. Phys. **118**, 2242 (2003)
247. C. Emmeluth, M.A. Suhm, Phys. Chem. Chem. Phys. **5**, 3094 (2003)
248. J. Chocholoušová, J. Vacek, P. Hobza, J. Phys. Chem. A **107**, 3086 (2003)
249. T. Häber, U. Schmitt, C. Emmeluth, M.A. Suhm, Faraday Discuss. **118**, 331 (2001)
250. S. Mukamel, Annu. Rev. Phys. Chem. **51**, 691 (2000)
251. M.J. Frisch, et al. Gaussian 03, Revision C.02. Gaussian, Inc., Wallingford, CT, 2004
252. A. Burneau, F. Génin, F. Quilès, Phys. Chem. Chem. Phys. **2**, 5020 (2000)
253. A.M. Moran, J. Dreyer, S. Mukamel., J. Chem. Phys. **118**, 1347 (2003)
254. K. Park, M. Cho, S. Hahn, D. Kim, J. Chem. Phys. **111**, 4131 (1999)
255. T. Hayashi, S. Mukamel, J. Phys. Chem. A **107**, 9113 (2003)
256. H.R. Zelsmann, Z. Mielke, Y. Marechal, J. Mol. Struct. **237**, 273 (1990)
257. G.M. Florio, T.S. Zwier, E.M. Myshakin, K.D. Jordan, E.L. Sibert III, J. Chem. Phys. **118**, 1735 (2003)
258. J. Dreyer, A.M. Moran, S. Mukamel, J. Phys. Chem. B **107**, 5967 (2003)